

AN ANALYSIS OF APPROACH NAVIGATION ACCURACY AND
GUIDANCE REQUIREMENTS FOR THE GRAND TOUR
MISSION TO THE OUTER PLANETS

BY
DONALD WAYNE JONES

AMRL 1025

AUGUST 1971

N72-12836

Unclas
09623

(NASA-CR-124641) AN ANALYSIS OF APPROACH
NAVIGATION ACCURACY AND GUIDANCE
REQUIREMENTS FOR THE GRAND TOUR MISSION TO
THE OUTER PLANETS D.W. Jones (Texas Univ.)
Aug. 1971 158 p

CSCS 22C G3/30
(CATEGORY)

FACILITY
CK
(NASA CR OR TMX OR AD NUMBER)



APPLIED MECHANICS RESEARCH LABORATORY
THE UNIVERSITY OF TEXAS AT AUSTIN AUSTIN, TEXAS

Reproduced by
NATIONAL TECHNICAL
INFORMATION SERVICE
Springfield, Va. 22151

AN ANALYSIS OF APPROACH NAVIGATION ACCURACY AND GUIDANCE REQUIREMENTS
FOR THE GRAND TOUR MISSION TO THE OUTER PLANETS

Donald Wayne Jones
The University of Texas at Austin
Austin, Texas

AMRL 1025
August 1971

Applied Mechanics Research Laboratory
The University of Texas at Austin
Austin, Texas

This report was prepared under

Contract No. NGR 44-012-008

for the

National Aeronautics and Space Administration

by the

Applied Mechanics Research Laboratory
The University of Texas at Austin
Austin, Texas

under the direction of

Byron D. Tapley
Professor and Chairman

~~PRECEDING PAGE BLANK NOT FILMED~~

PREFACE

In the late 1960's the highly successful Mariner missions opened an exciting era of planetary exploration. Our knowledge of the near planets will soon be further enhanced by the Mariner and Viking missions scheduled for the early 1970's. In the later half of this decade our exploration of the solar system will be extended to the outer planets - Jupiter, Saturn, Uranus, Neptune and Pluto. The alignment of the outer planets in the period from 1976 to 1980 offers several favorable opportunities for successive flybys of various combinations of the planets. One of the most interesting, and ambitious, is an opportunity in 1977 for launching a spacecraft on a mission which includes successive flybys of Jupiter, Saturn, Uranus and Neptune - the Grand Tour.

Because of the extreme sensitivity of the Grand Tour mission to errors in the encounter trajectory at the intermediate planets, the success of the mission will depend to a large extent on the effectiveness of the navigation and guidance process during planetary approach. In this study, the theory of linear estimation was applied to the problem of defining the approach navigation accuracy and guidance requirements for the Grand Tour mission.

Special gratitude is expressed to Dr. B. D. Tapley for serving as supervising professor for this research. His encouragement, guidance and friendship during the author's course of study at The University of Texas are greatly appreciated. The author would also like to thank Dr. V. G. Szebehely, Dr. W. T. Fowler, Dr. P. E. Russell, and Dr. G. H. Born for

serving on the supervising committee. Also, a special thanks is extended to Mollie Schluter for her skillful typing of the manuscript.

The author wishes to acknowledge the cooperation and support given the author by the engineering management of Convair Aerospace Division of General Dynamics Corporation, Fort Worth, Texas, during the course of his graduate studies. The encouragement of V. A. Lee was especially appreciated. The author thanks Sharon Leifeste for her assistance in typing the drafts, and Grace Sullivan and Joe Delwaide for their work on the illustrations.

Finally, the author would like to express his deep appreciation to his wife, Janie, and his sons, Steven and Darrell, for their understanding, encouragement and patience during the course of his graduate studies.

Donald Wayne Jones

August 1971
Austin, Texas

ABSTRACT

The navigation and guidance process for the Jupiter, Saturn and Uranus planetary encounter phases of the 1977 Grand Tour Interior mission was simulated. The objectives of the investigation were to (1) define reference approach navigation accuracies, (2) evaluate the relative information content of the various observation types, (3) survey and define reference encounter guidance requirements, (4) determine sensitivities to assumed simulation model parameters, and (5) assess the adequacy of the linear estimation theory.

A linear sequential estimator is used to provide an estimate of the augmented state vector which consists of the six state variables of position and velocity plus the three components of a planet position bias. The distribution of random observation errors is assumed to be Gaussian with zero mean and known covariance matrix. Navigation accuracies are determined from an analysis of the error covariance matrix associated with the state estimate. Evaluation of the errors in the estimates for the state and target vectors are accomplished by direct comparison with the simulated data.

The guidance process is simulated using a non-spherical model of the execution errors. The uncertainty in the velocity correction is assumed to originate from: (1) uncertainty in the magnitude of ΔV due to a random error in the total impulse applied by the control rocket, and (2) uncertainty in the orientation of the correction vector due to random errors in the direction of the thrust vector. A simplified guidance algorithm is developed and

used to compute the velocity correction required at a specified time to null the deviation between the estimated target vector and the nominal target vector.

Computational algorithms which simulate the navigation and guidance process were derived from the theory and implemented into two research-oriented computer programs. Programs STEP V and STEP VI were written in FORTRAN IV for the CDC 6600 system at the University of Texas at Austin. Program STEP VI utilizes the interactive graphics capability of the CDC 252 display console to provide a powerful computational tool for the rapid analysis of interplanetary navigation and guidance problems.

TABLE OF CONTENTS

	Page
PREFACE	iii
ABSTRACT	v
LIST OF FIGURES	x
LIST OF TABLES	xii
 CHAPTER 1 - INTRODUCTION	 1
1.1 MISSION DESCRIPTION	2
1.2 PROBLEM DESCRIPTION	2
1.3 TECHNICAL APPROACH	5
 CHAPTER 2 - THEORETICAL DEVELOPMENT	 7
2.1 STATE EQUATIONS	7
EQUATION OF MOTION	7
THE STATE VECTOR	8
THE AUGMENTED STATE VECTOR	10
LINEARIZATION OF THE STATE EQUATIONS: THE STATE TRANSITION MATRIX	11
2.2 OBSERVATION-STATE RELATIONSHIPS	12
OBSERVATION EQUATIONS	13
MOTION OF THE TRACKING STATIONS	16
2.3 ERROR SIMULATION MODELS	18
SIMULATION OF THE OBSERVATIONS	19
SIMULATION OF THE INITIAL STATE ERRORS	20
SIMULATION OF THE GUIDANCE CORRECTION ERRORS	20
2.4 LINEAR ESTIMATION THEORY	23
MAXIMUM LIKELIHOOD ESTIMATION	23
STATISTICAL ASSUMPTIONS	24

	Page
THE LIKELIHOOD FUNCTION	25
MAXIMIZING THE LIKELIHOOD FUNCTION	26
BATCH PROCESSING	28
SEQUENTIAL STATE ESTIMATION	29
SEQUENTIAL ESTIMATION ALGORITHM	31
2.5 GUIDANCE THEORY	32
TARGETING VECTOR	32
UPDATING THE STATE ESTIMATE ERROR COVARIANCE MATRIX, P	34
UPDATING THE STATE ERROR COVARIANCE MATRIX, S	35
VELOCITY CORRECTION COVARIANCE MATRICES	37
STATISTICS OF THE MAGNITUDE OF THE VELOCITY CORRECTION	38
STATISTICS OF THE TARGETING ERROR	38
GUIDANCE ALGORITHM	39
CHAPTER 3 - COMPUTATIONAL DEVELOPMENT	41
3.1 DESCRIPTION OF THE PROGRAMS	41
3.2 DESCRIPTION OF INTERACTIVE PROGRAM OPERATION	45
CHAPTER 4 - APPROACH NAVIGATION ANALYSIS	47
4.1 ASSUMED ERROR SOURCES	47
4.2 REFERENCE NAVIGATION ACCURACY	48
STATE ESTIMATE UNCERTAINTY	50
STATE ESTIMATE UNCERTAINTY DURING JUPITER APPROACH	52
STATE ESTIMATE UNCERTAINTY DURING SATURN APPROACH	55
STATE ESTIMATE UNCERTAINTY DURING URANUS APPROACH	57
TARGET ESTIMATE ACCURACY	57
JUPITER TARGET ERROR ELLIPSES	59
SATURN TARGET ERROR ELLIPSES	62
URANUS TARGET ERROR ELLIPSES	65
OVERALL STATE UNCERTAINTY	68
TARGET ERRORS FOR SIMULATED ENCOUNTER	73

	Page
CHAPTER 5 - APPROACH GUIDANCE ANALYSIS	84
5.1 ASSUMED EXECUTION ERRORS	84
5.2 PRELIMINARY CONSIDERATIONS	85
5.3 APPROACH GUIDANCE REQUIREMENTS AND TARGET ACCURACIES	89
ONE CORRECTION SURVEY	89
TWO CORRECTION SURVEY	89
5.4 GUIDANCE SENSITIVITY ANALYSIS	100
5.5 MONTE CARLO SIMULATION	103
INITIAL STATE ERRORS	103
MONTE CARLO RESULTS	104
CHAPTER 6 - CONCLUSIONS AND RECOMMENDATIONS	109
PRINCIPAL CONCLUSIONS	109
RECOMMENDATIONS FOR FUTURE STUDY	112
APPENDICES	114
APPENDIX A - NOMINAL GRAND TOUR MISSION DATA	115
APPENDIX B - THE DYNAMICAL EQUATIONS IN RECTANGULAR CARTESIAN COORDINATES	118
APPENDIX C - THE OBSERVATION-STATE RELATIONSHIPS IN RECTANGULAR CARTESIAN COORDINATES	122
APPENDIX D - THE DERIVATION AND APPLICATION OF THE SHUR IDENTITY	127
APPENDIX E - THE DERIVATION AND APPLICATION OF THE ELLIPSOID OF PROBABILITY	129
APPENDIX F - DEFINITION OF THE B-VECTOR TARGETING SYSTEM	135
APPENDIX G - DERIVATION OF THE TARGET MAPPING MATRIX C	139
REFERENCES	144
BIBLIOGRAPHY	146

LIST OF FIGURES

Figure		Page
1	Heliocentric Profile of the 1977 Grand Tour Mission	3
2	Problem Geometry	9
3	Earth-based Observation Geometry	15
4	Onboard Observation Geometry	15
5	Tracking Station Geometry	17
6	Guidance Correction Geometry	21
7	Step V Computational Logic	43
8	Step VI Program Structure	44
9	State Estimate Uncertainty During Jupiter Approach	54
10	State Estimate Uncertainty During Saturn Approach	56
11	State Estimate Uncertainty During Uranus Approach	58
12	Navigation Target Error Ellipses for Jupiter Approach, (RR, OBA, RR + OBA)	60
13	Navigation Target Error Ellipses for Jupiter Approach, (E-30, E-15, E-5)	61
14	Navigation Target Error Ellipses at Saturn Approach, (RR, OBA, RR + OBA)	63
15	Navigation Target Error Ellipses at Saturn Approach, (E-20, E-10, E-2)	64
16	Navigation Target Error Ellipses at Uranus Approach, (RR, OBA, RR + OBA)	66
17	Navigation Target Error Ellipses at Uranus Approach, (E-20, E-10, E-1)	67

Figure		Page
18	Time Histories of State Uncertainty, (Jupiter, Saturn, Uranus) . . .	72
19	Time Histories of Target Errors at Jupiter Approach, (RR)	75
20	Time Histories of Target Errors at Jupiter Approach, (OBA)	76
21	Time Histories of Target Errors at Jupiter Approach, (RR + OBA) . . .	77
22	Time Histories of Target Errors at Saturn Approach, (RR)	78
23	Time Histories of Target Errors at Saturn Approach, (OBA)	79
24	Time Histories of Target Errors at Saturn Approach, (RR + OBA) . . .	80
25	Time Histories of Target Errors at Uranus Approach, (RR)	81
26	Time Histories of Target Errors at Uranus Approach, (OBA)	82
27	Time Histories of Target Errors at Uranus Approach, (RR + OBA) . . .	83
28	Geometric Representation of Navigation and Guidance Covariance Matrices	86
29	One Correction Guidance Survey at Jupiter Approach	90
30	One Correction Guidance Survey at Saturn Approach	91
31	One Correction Guidance Survey at Uranus Approach	92
32	Survey of Guidance Performance Index I_1 , Jupiter	94
33	Survey of Guidance Performance Index I_1 , Saturn	95
34	Survey of Guidance Performance Index I_1 , Uranus	96
35	Survey of Guidance Performance Index I_2 , Jupiter	97
36	Survey of Guidance Performance Index I_2 , Saturn	98
37	Survey of Guidance Performance Index I_2 , Uranus	99
38	Monte Carlo Simulation Results	106
39	Standard Probability Ellipse	134
40	Targeting Geometry	136

LIST OF TABLES

Table		Page
1	Nominal One-Sigma Values for Assumed Error Sources	49
2	Diagonal Elements of the Apriori State Estimate Covariance Matrix, P_0	51
3	Comparison of Navigation Accuracies at Jupiter Approach	69
4	Comparison of Navigation Accuracies at Saturn Approach	70
5	Comparison of Navigation Accuracies at Uranus Approach	71
6	Approach Guidance Sensitivities	102
7	Simulated Initial State Error Statistics	105
8	Monte Carlo Simulation Results	107
9	Heliocentric Trajectory Parameters	116
10	Planetocentric Flyby Parameters	117

CHAPTER 1

INTRODUCTION

During the last half of this decade the United States will embark on one of the most significant scientific investigations of all time--the exploration of the outer planets. Unmanned spacecraft will travel billions of miles to the outer edge of our solar system and send back data which will help scientists understand the origin and evolution of the universe. The key to the investigation will be the planet Jupiter, regarded by many as the primary object of interest in the solar system. Because of Jupiter's powerful trajectory shaping capability, missions to the outer planets will include a swingby of Jupiter as a means of reducing launch energy requirements and associated trip times.⁽¹⁾

The alignment of the outer planets in the period from 1976 to 1980 offers favorable opportunities for several multi-planet flyby missions,^(2,3) some of these are:

- 1976-80 Jupiter-Saturn,
- 1978-80 Jupiter-Pluto,
- 1978-80 Jupiter-Uranus-Neptune,
- 1977-78 Jupiter-Saturn-Pluto, and
- 1976-80 Jupiter-Saturn-Uranus-Neptune (Grand Tour).

Of particular interest is the four-planet flyby mission commonly referred to as the Grand Tour. The Grand Tour involves successive flybys of the planets Jupiter, Saturn, Uranus, and Neptune.

1.1 Mission Description

The 1977 Grand Tour Interior Mission departs Earth in September of 1977 and arrives at Neptune nine years later. A profile of the heliocentric trajectory for the nominal mission is shown in Figure 1. Jupiter encounter at an altitude of 194,500 km occurs 550 days after Earth departure. The swingby of Jupiter turns the velocity vector and increases the heliocentric energy so that the spacecraft encounters Saturn 576 days later. At Saturn the spacecraft passes inside the rings at an altitude of 9,180 km. The Saturn-Uranus leg takes 1230 days and brings the spacecraft within 13,100 km of Uranus. After an additional flight time of 998 days the spacecraft swings by Neptune and departs on a trajectory which escapes the solar system. The heliocentric trajectory lies very close to the ecliptic plane throughout the mission with a maximum heliocentric inclination of 2.45 degrees for the Jupiter-Saturn leg. Total heliocentric angle displacement for the mission is 326 degrees. A more detailed definition of the nominal mission is given in Appendix A.

1.2 Problem Description

From a navigation and guidance standpoint, the Grand Tour mission presents several unusual problems which have not been encountered in previous interplanetary missions. Some of these are listed below:

- (1) Severe guidance requirements. Extreme trajectory error sensitivities result in a requirement for guidance maneuvers during approach and during departure at each planet.^(4,5,6)
- (2) Long round-trip communication time. In addition to operational problems caused by the time delay (5.5 hours at Uranus), the accuracy of the earth-based doppler data is reduced.⁽⁷⁾

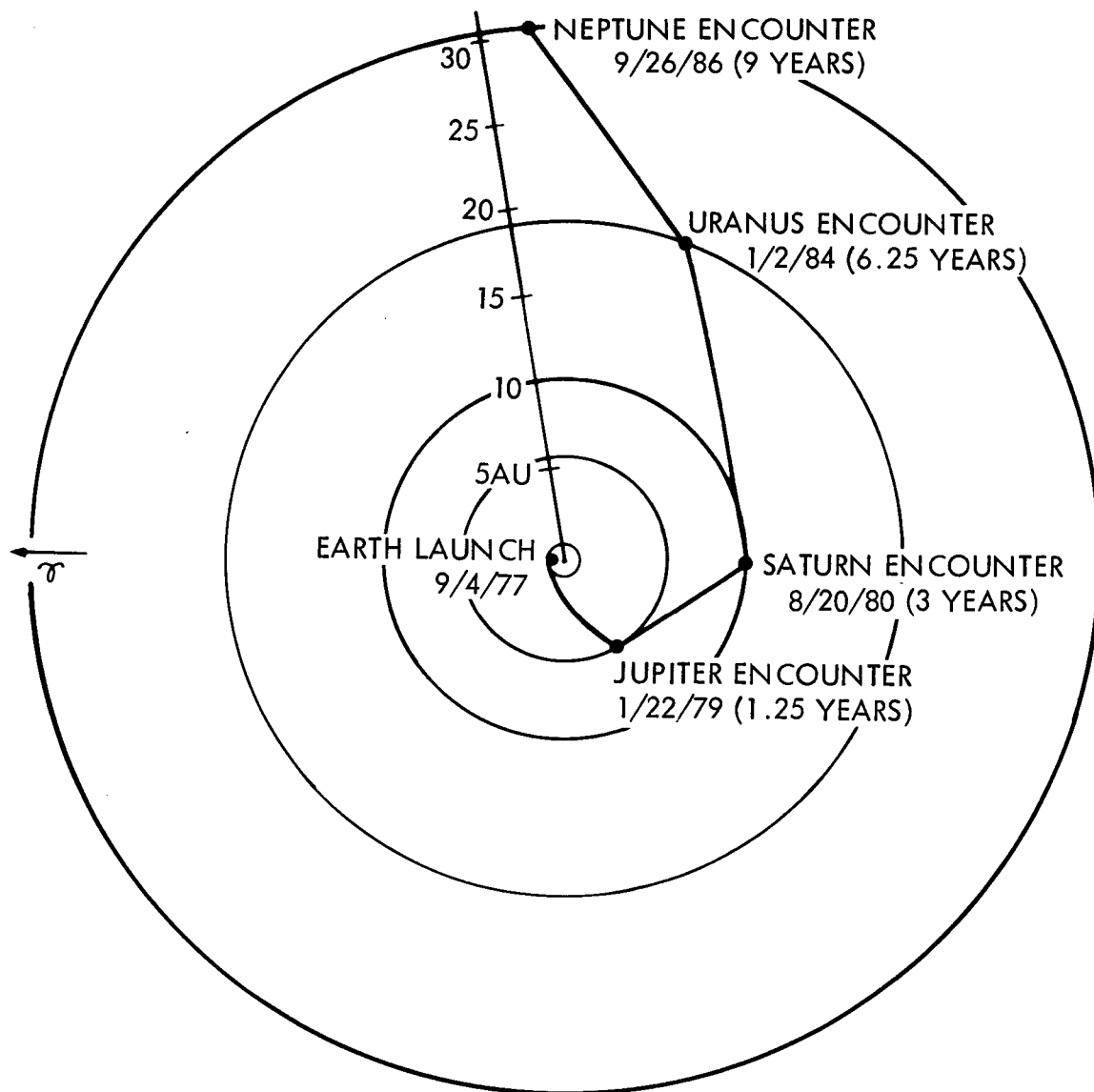


Figure 1 Helio-centric Profile of the 1977 Grand Tour Mission

- (3) Large uncertainties in the planetary ephemerides. Uncertainties on the order of 0.2 arc-sec are predicted for the late 1970's⁽⁸⁾. (At Uranus 0.2 arc-sec is equivalent to about 3,000 km.)
- (4) Encounter constraints. The trajectory must either pass outside Saturn's rings (exterior mission) or through the small region inside the rings (interior mission). Exterior missions have longer total mission durations, lower launch energy requirements, and less critical guidance requirements than the interior missions.
- (5) Long mission durations. The long trip times (typically about 9 years) and extreme trajectory sensitivity make precision numerical simulations both difficult and expensive. A high degree of reliability is required for onboard navigation and guidance systems.

Because of the extreme sensitivity of multi-planet flyby missions to errors in the encounter trajectory at the intermediate planets, the success of the Grand Tour will depend to a large extent on the effectiveness of navigation and guidance procedures during planetary approach. The spacecraft will arrive at the sphere of influence of each planet with large uncertainties in the state of the spacecraft relative to the planet. Approach navigation must reduce this uncertainty to an acceptable tolerance before an effective guidance correction can be performed. Guidance corrections based on poor navigation information will result in an incorrect execution and wasted guidance propellant. If the execution errors remain uncorrected throughout approach they will be amplified by the encounter and will require large post-encounter corrections.

Approach guidance correction requirements vary with execution time and increase sharply a few days prior to encounter. Navigation accuracy also increases during approach due to the improved planetocentric state information

provided by the observations. Since increased approach navigation accuracy is reflected in lower post-encounter corrections, the selection of the approach guidance execution time for minimum guidance propellant is an important optimization problem.

1.3 Technical Approach

In this study the navigation and guidance process for the Jupiter, Saturn and Uranus planetary encounter phases of the 1977 Grand Tour Interior mission has been simulated. The objectives of the investigation were to (1) define reference approach navigation accuracies, (2) evaluate the relative information content of the various observation types, (3) survey and define reference encounter guidance requirements, (4) determine sensitivities to assumed simulation model parameters, and (5) assess the adequacy of the linear estimation theory.

A linear sequential estimator is used to provide an estimate of the augmented state vector which consists of six state variables of position and velocity plus the three components of a planet position bias. The distribution of the random observation errors is assumed to be Gaussian with zero mean and known covariance matrix. Reference navigation accuracies are determined from analysis of the error covariance matrix associated with the state estimate. Evaluation of the accuracy of the estimated state and target vector are accomplished by direct comparison with simulated data.

The guidance process is simulated using a non-spherical model of the execution errors. The uncertainty in the velocity correction is assumed to originate from: (1) uncertainty in the magnitude of the correction vector due to a random error in the total impulse applied by the control rocket, and (2) uncertainty in the orientation of the correction vector due to random errors

in the direction of the thrust vector. A simplified guidance algorithm is developed and used to compute the velocity correction required to null the deviation between the estimated target vector and the nominal target vector.

In Chapter 2 the computational algorithms and error models used to simulate the navigation and guidance process are derived from the theory. Supporting derivations are found in Appendices B, C, and D. The computational algorithms were incorporated into two research-oriented computer programs. The programs, one an interactive graphics program, are described in Chapter 3.

Chapter 4 contains a comprehensive analysis of the navigation process during approach to Jupiter, Saturn, Uranus and Neptune. Reference navigation accuracies are defined for several combinations of Earth-based radar and on-board angle observations. Appendices E and F supplement Chapter 4.

An analysis of approach guidance is contained in Chapter 5. Guidance execution times are surveyed to determine the variation of guidance requirements and target accuracy during approach to Jupiter, Saturn, Uranus and Neptune. Sensitivities are defined for the effect of observation accuracy, guidance execution accuracy, and initial state errors on the guidance process. Finally, the results of a Monte Carlo simulation of the approach navigation and guidance process at Saturn encounter are presented. Appendices E, F and G supplement Chapter 5.

Chapter 6 summarizes the pertinent results and conclusions of the study and outlines recommended extensions to the work.

CHAPTER 2

THEORETICAL DEVELOPMENT

This chapter contains the theoretical development of the computational algorithms used to simulate planetary approach navigation and guidance. The chapter is divided into five sections as follows: 2.1 State Equations, 2.2 Observation-State Relationships, 2.3 Error Simulation Models, 2.4 Linear Estimation Theory, and 2.5 Guidance Theory.

2.1 State Equations

In the analysis presented here, the spacecraft motion relative to the target planet is approximated by a three-dimensional elliptic restricted three-body model. For this model the target planet is assumed to move about the sun in an unperturbed elliptic orbit while the third body (the spacecraft) moves under the influence of both primaries. The state (position and velocity) of the spacecraft relative to the target planet is obtained by numerical integration of the total acceleration resulting from the attraction of the sun and the planet.

Equation of Motion

The motion of a spacecraft which is perturbed by the sun as it approaches a target planet, is governed by the vector differential equation

$$\ddot{\mathbf{r}} = \bar{\mathbf{v}}(U_0 + U_1) \quad (2.1)$$

where \bar{r} is the position vector of the spacecraft relative to the planet, $U_0 = \frac{\mu}{r}$ is the two-body force function, μ is the gravitational parameter of the planet, r is the magnitude of \bar{r} , and U_1 is the third body disturbing function. The disturbing function, which expresses the perturbing effect of the sun on the spacecraft, is given by

$$U_1 = \mu_s \left(\frac{1}{R} - \frac{\bar{r} \cdot \bar{R}_t}{R R_t} \right) \quad (2.2)$$

where μ_s is the gravitational parameter of the sun, R_t is the magnitude of the heliocentric position vector of the target planet, \bar{R}_t , and R is the magnitude of the heliocentric position vector of the spacecraft, \bar{R} . Recognizing that $\nabla\left(\frac{1}{r}\right) = -\left(\frac{\bar{r}}{r^3}\right)$, the equations of motion can be written as

$$\ddot{\bar{r}} = \mu \frac{\bar{r}}{r^3} - \mu_s \left[\frac{\bar{R}}{R^3} - \frac{\bar{R}_t}{R_t^3} \right]. \quad (2.3)$$

The vector \bar{r} , \bar{R} and \bar{R}_t are defined in Fig. 2.

Eq. (2.3) can be reduced to a system of first order differential equations by the following transformation

$$\begin{aligned} \dot{\bar{r}} &= \bar{v} \\ \dot{\bar{v}} &= -\mu \frac{\bar{r}}{r^3} - \mu_s \left[\frac{\bar{R}}{R^3} - \frac{\bar{R}_t}{R_t^3} \right] \end{aligned} \quad (2.4)$$

The heliocentric position of the planet, i.e., R_t in Eq. (2.4), is obtained from a classical solution of the two-body problem.

The State Vector

The two first order, nonlinear, vector differential equations (Eqs. (2.4)) can be represented by

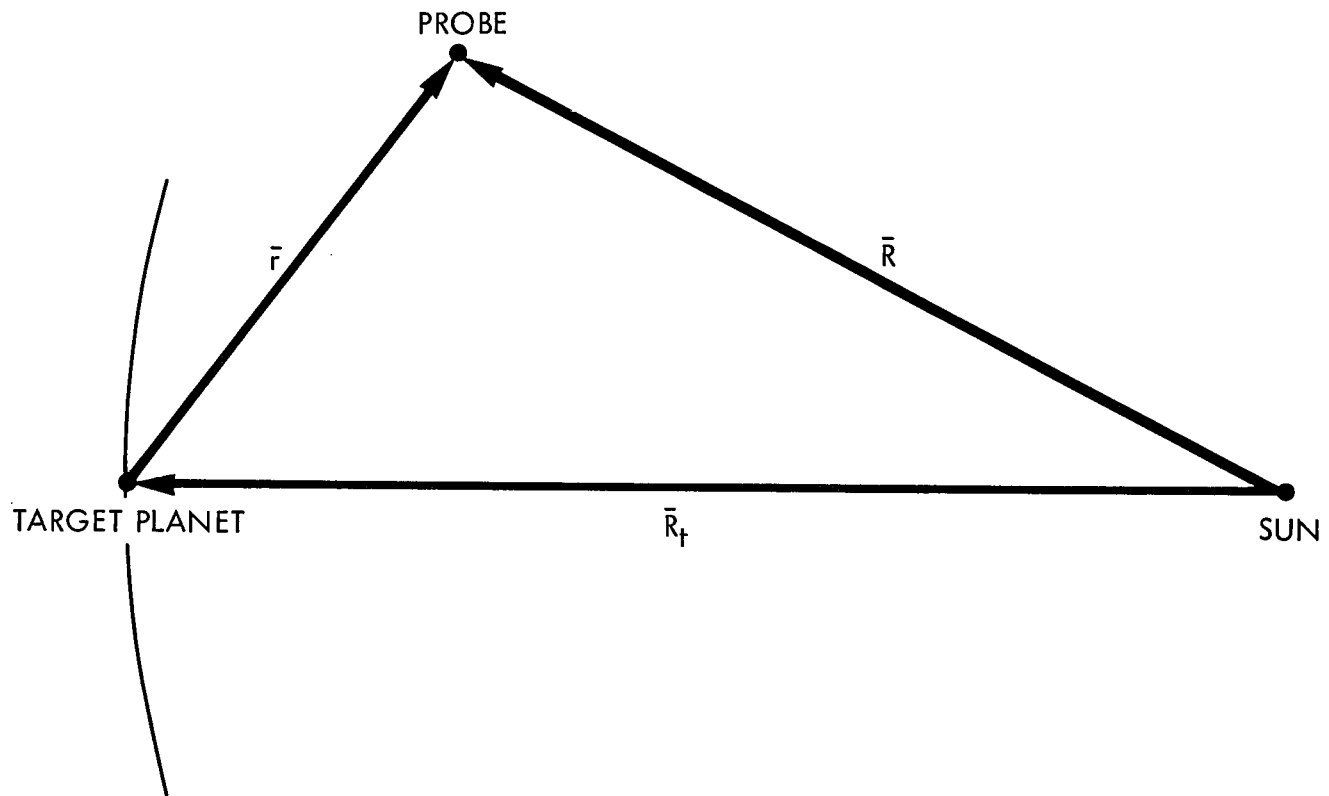


Figure 2 Problem Geometry

$$\dot{\tilde{X}} = F(\tilde{X}, t) \quad (2.5)$$

where the state vector \tilde{X} is defined as

$$\tilde{X} = \begin{bmatrix} \bar{r} \\ \bar{v} \end{bmatrix} \quad (2.6)$$

and the 6-vector F is the corresponding right hand side of Eqs. (2.4).

The Augmented State Vector

It is sometimes necessary or desirable to estimate certain parameters of the dynamical and/or error models whose values are not well established. For the problem treated here, the uncertainty in the position of the outer planets was considered large enough to justify its inclusion as a vector to be estimated. This was accomplished by augmenting the state vector with the planetary bias vector \bar{b} . The augmented state vector, a 9-vector, is defined as

$$X = \begin{bmatrix} \bar{r} \\ \bar{v} \\ \bar{b} \end{bmatrix} . \quad (2.7)$$

Since the position vector of the target planet changes very slowly during the relatively short encounter period, the error in the position vector was assumed to be a constant bias. The augmented state vector is therefore governed by the vector differential equation

$$\dot{X} = \begin{bmatrix} F(\tilde{X}, t) \\ \phi \end{bmatrix} . \quad (2.8)$$

Analytical expressions for the components of Eq. (2.8) are given in rectangular cartesian coordinates in Appendix B.

Linearization of the State Equations: The State Transition Matrix

As discussed in the previous section the n-dimensional state vector, X , can be defined as the solution to the first order, nonlinear, vector differential equation

$$\dot{X}(t) = F(X,t) ; \quad X(t_0) = X_0 . \quad (2.9)$$

Expanding Eq. (2.9) in a Taylor series about a nominal solution (designated with an asterisk) yields

$$\dot{X} = \dot{X}^* + [\partial F/\partial X]^* (X - X^*) + \dots \quad (2.10)$$

Neglecting terms of order higher than the first Eq. (2.9) can be written

$$\dot{x} = Ax ; \quad x(t_0) = x_0 \quad (2.11)$$

where $x = X - X^*$ and $A = [\partial F/\partial X]^*$.

By the theory of linear differential equations⁽⁹⁾ the solution of Eq. (2.11) can be expressed in the form

$$x(t) = \Phi(t,t_0)x_0 \quad (2.12)$$

where $\Phi(t,t_0)$ is an nxn transition matrix relating state deviations at time t_0 to state deviations at time t . Differentiating Eq. (2.12) yields

$$\dot{x}(t) = \dot{\Phi}(t,t_0)x_0 . \quad (2.13)$$

Subsequent substitutions result in the following development

$$\begin{aligned} \dot{\Phi}(t,t_0)x_0 &= A(t) x(t) \\ \dot{\Phi}(t,t_0)x_0 &= A(t) \Phi(t,t_0)x_0 \\ 0 &= [A(t) \Phi(t,t_0) - \dot{\Phi}(t,t_0)]x_0 . \end{aligned} \quad (2.14)$$

For a nontrivial solution x_0 will be non-zero. Therefore Eq. (2.4) can be satisfied only if the matrix differential equation governing the state transition matrix satisfies the relation

$$\dot{\Phi}(t, t_0) = A(t) \Phi(t, t_0); \quad \Phi(t_0, t_0) = I . \quad (2.15)$$

The state transition matrix has the following properties:

- 1) $\Phi(t, t) = I$, the $n \times n$ identity matrix
- 2) $\Phi(t_k, t_j) = \Phi(t_k, t_i) \Phi(t_i, t_j)$ for any t_i , t_j and t_k
- 3) $\Phi(t_i, t_j) = \Phi^{-1}(t_j, t_i)$ for any t_i and t_j .

For this study the transition matrix was obtained by numerical integration of the system of linear differential equations given by Eq. (2.15). Alternately, the nonlinear differential equation governing the state (Eq. 2.9) can be integrated n times from t_0 to t to generate the required matrix of numerical partial derivatives. The transition matrix is then formed by

$$\Phi(t, t_0) = \frac{\partial X(t)}{\partial X(t_0)} . \quad (2.16)$$

Analytical expressions for the elements of the 9×9 A matrix are given in Appendix B.

2.2 Observation-State Relationships

At any given time the observation vector Y is related to the state vector X by the nonlinear equation

$$Y(t) = G(X, t) + \varepsilon \quad (2.17)$$

where ϵ is the random error in the observation. Expanding Eq. (2.17) in a Taylor series about the nominal state and neglecting terms of order higher than the first yields

$$Y(t) = Y^*(t) + [\partial G/\partial X]^* (X(t) - X^*(t)) + \epsilon . \quad (2.18)$$

When this linearization is valid, the deviation in the observation can be expressed as

$$y(t) = \hat{H}(t) x(t) + \epsilon . \quad (2.19)$$

where $y = Y - Y^*$, $x = X - X^*$ and $\hat{H}(t) = [\partial G/\partial X]^*$.

Recalling from the previous section that

$$x(t_i) = \Phi(t_i, t_k) x(t_k) \quad (2.20)$$

the observation deviation at time t_i can be expressed in terms of the state deviation at time t_k by

$$y(t_i) = \hat{H}(t_i) \Phi(t_i, t_k) x(t_k) + \epsilon_i . \quad (2.21)$$

It is convenient to write Eq. (2.21) as

$$y_i = H_i x_k + \epsilon \quad (2.22)$$

and this convention will be used in the following sections. Note that when $i = k$, then $H_k = \hat{H}_k$. Analytical expressions for the elements of the \hat{H} matrix in rectangular cartesian coordinates are given in Appendix C.

Observation Equations

Four observation types were considered in this study:

1) Range (ρ)	}	Earth-based (Fig. 3)
2) Range-Rate ($\dot{\rho}$)		
3) Sun-Planet Angle (α)	}	onboard (Fig. 4)
4) Star-Planet Angle (β)		

When all four observations occur simultaneously, Y is a 4-vector defined as follows

$$Y^T = [\rho, \dot{\rho}, \alpha, \beta]. \quad (2.23)$$

The Range, the linear distance from the tracking station to the spacecraft, is defined by

$$\rho = (\bar{\rho} \cdot \bar{\rho})^{\frac{1}{2}} \quad (2.24)$$

where $\bar{\rho} = \bar{R} - \bar{R}_s$, \bar{R}_s is the heliocentric distance of a topocentric tracking station, and \bar{R} is the heliocentric distance to the spacecraft.

The Range-Rate, the time rate of change of range, is defined by

$$\dot{\rho} = (\dot{\bar{\rho}} \cdot \bar{\rho}) / \rho \quad (2.25)$$

where $\dot{\bar{\rho}} = \dot{\bar{R}} - \dot{\bar{R}}_s$.

The Sun-Planet Angle, the smaller angle between the spacecraft-planet line and the spacecraft-sun line, is defined by

$$\alpha = \cos^{-1} \left[\frac{\bar{r} \cdot \bar{R}}{r R} \right] \quad (2.26)$$

or

$$\alpha = \cos^{-1} \left[\frac{\bar{r} \cdot \bar{R}_t + r^2}{r R} \right] \quad (2.27)$$

where $0 < \alpha < \pi$ and where \bar{r} is the planetocentric position vector of the spacecraft.

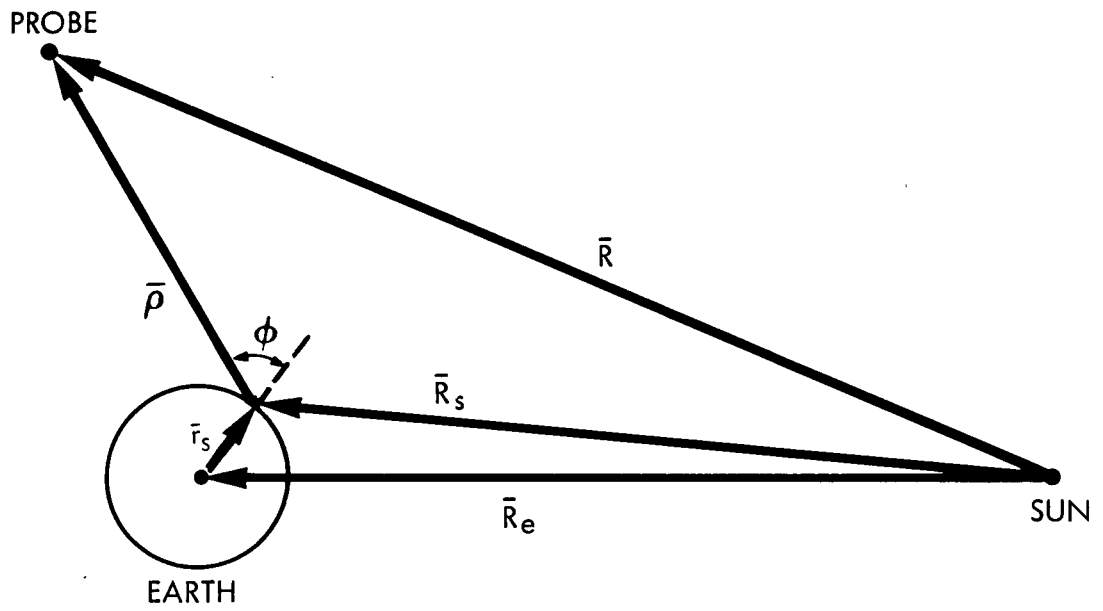


Figure 3 Earth-Based Observation Geometry

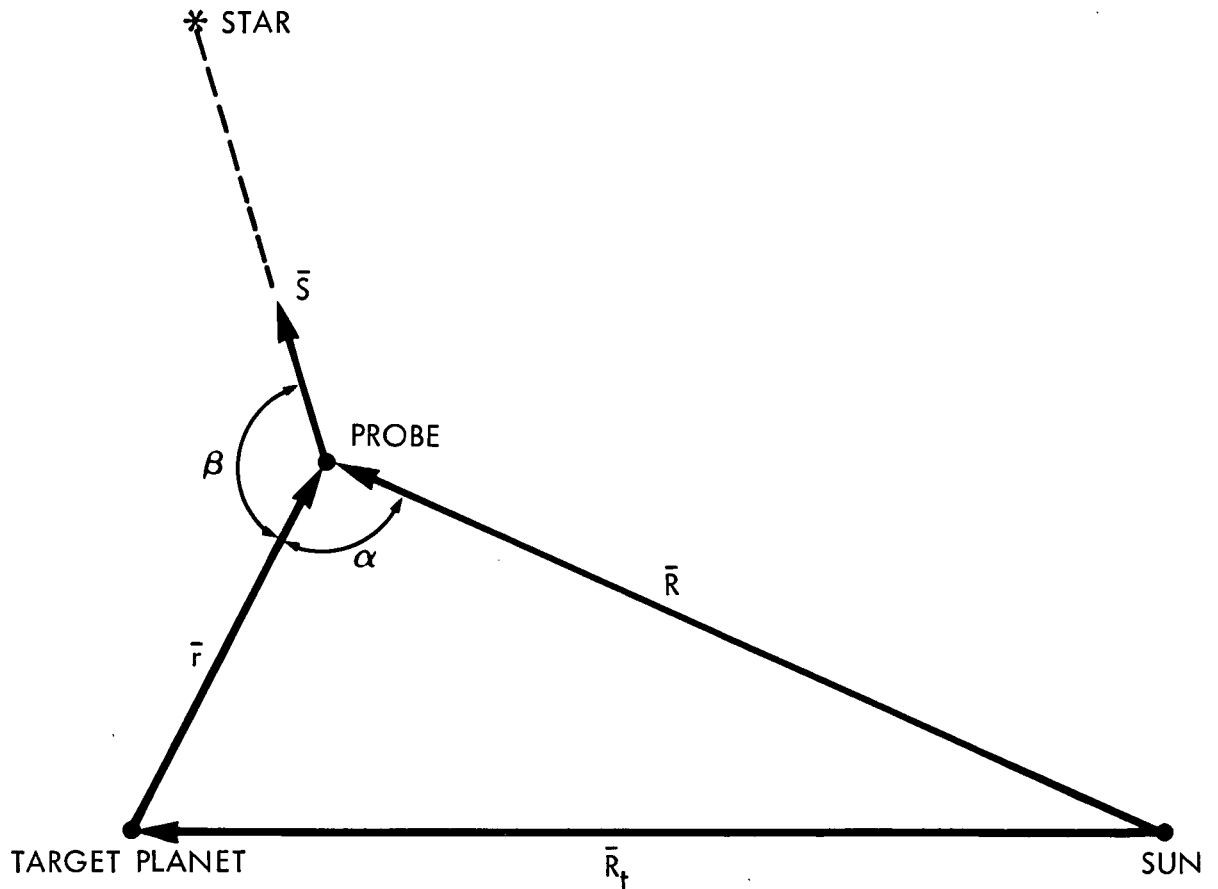


Figure 4 Onboard Observation Geometry

The Star-Planet Angle, the smaller angle between the probe-planet line and the line from the probe to a navigation star, is defined by

$$\beta = \cos^{-1}[-(\bar{r} \cdot \bar{s})/r] \quad (2.28)$$

where \bar{s} is a unit vector in the direction of the navigation star.

Motion of the Tracking Stations

Range and range-rate measurements were assumed to be taken from a tracking station whose heliocentric position vector \bar{R}_s is given by

$$\bar{R}_s = \bar{R}_e + \bar{r}_s \quad (2.29)$$

where \bar{R}_e is the heliocentric position of the earth, and \bar{r}_s is the geocentric position of the tracking station. Given the right ascension, α_s , declination, δ_s , and geocentric distance, r_s , of the tracking station at time t , the heliocentric position of the station is defined by

$$\bar{R}_s = \bar{R}_e + [E]r_s \begin{bmatrix} \cos \delta_s \cos \alpha_s(t) \\ \cos \delta_s \sin \alpha_s(t) \\ \sin \delta_s \end{bmatrix} \quad (2.30)$$

where $[E]$ is a 3x3 rotation matrix which transforms the right-ascension declination system to the heliocentric system. If the heliocentric system is the ecliptic system, $[E]$ is defined as

$$[E] = \begin{bmatrix} 1 & 0 & 0 \\ 0 & \cos i_\epsilon & \sin i_\epsilon \\ 0 & -\sin i_\epsilon & \cos i_\epsilon \end{bmatrix} \cdot \quad (2.31)$$

The argument i_ϵ is the obliquity of the ecliptic. Tracking station geometry is illustrated in Fig. 5.

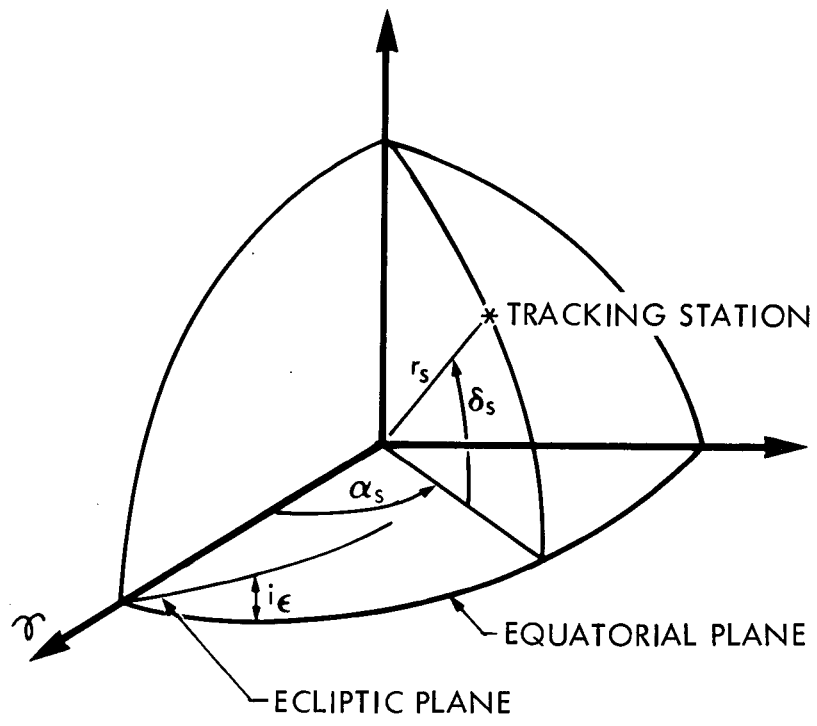


Figure 5 Tracking Station Geometry

With the assumption that the earth's rotation is uniform, the right ascension of the tracking station can be expressed as

$$\alpha_s(t) = \alpha_s(t_0) + \dot{\alpha}_s(t - t_0) \quad (2.32)$$

where $\alpha_s(t_0)$ is defined at some epoch time t_0 . Differentiation of Eq. (2.30) with respect to time yields

$$\dot{\bar{R}}_s = \dot{\bar{R}}_e + [E]r_s \dot{\alpha}_s \begin{bmatrix} -\cos \delta_s \sin \alpha_s(t) \\ \cos \delta_s \cos \alpha_s(t) \\ 0 \end{bmatrix} . \quad (2.33)$$

2.3 Error Simulation Models

Errors in the components of the observation, initial state and guidance velocity correction vectors were modeled as normally distributed scalar random errors with zero mean and known variance. The errors were simulated by sampling at random from a standard normal distribution (zero mean and unit variance) and then scaling the error by the square root of the given variance.

The density function for the standard normal error z is given by

$$p(z) = (2\pi)^{-1/2} \exp(-z^2/2) . \quad (2.34)$$

The probability that a sampled value of the standard distribution will be less than a given value \bar{z} is given by the cumulative distribution function⁽¹⁰⁾

$$F = (2\pi)^{-1/2} \int_{-\infty}^{\bar{z}} \exp(-z^2/2) dz . \quad (2.35)$$

The inverse of Eq. (2.35) can be approximated by the curve fit equation⁽¹¹⁾

$$\bar{z} \cong \Gamma - \frac{c_0 + c_1\Gamma + c_2\Gamma^2}{1 + d_1\Gamma + d_2\Gamma^2 + d_3\Gamma^3} \quad (2.36)$$

$$\Gamma = [\ln(F^{-2})]^2 \quad (2.37)$$

where the coefficients c_i and d_i have the following values:

$$\begin{aligned} c_0 &= 2.515517 & d_1 &= 1.432788 \\ c_1 &= 0.802853 & d_2 &= 0.189269 \\ c_3 &= 0.010328 & d_3 &= 0.001308 . \end{aligned}$$

Sampling of the standard normal distribution was accomplished by first sampling at random from a uniform distribution to obtain a value for F ($0 \leq F \leq 1$) and then computing the standard normal error from Eq. (2.36). The simulated error is then computed as the product of the standard error and the square root of the given variance.

Simulation of the Observations

The observational data were simulated by adding random errors to the observation value computed from the simulated value of the true state, i.e.,

$$Y = Y_{\text{true}} + \varepsilon . \quad (2.38)$$

The true state is obtained by numerically integrating Eq. (2.4) using the simulated initial state vector. If the components of the error vector are assumed to be uncorrelated, the observation covariance matrix can be written

$$R = \begin{bmatrix} \sigma_\rho^2 & 0 & 0 & 0 \\ 0 & \sigma_\rho^2 & 0 & 0 \\ 0 & 0 & \sigma_\alpha^2 & 0 \\ 0 & 0 & 0 & \sigma_\beta^2 \end{bmatrix} . \quad (2.39)$$

The errors in the components can then be generated independently by the method of the preceding paragraph.

Simulation of the Initial State Errors

For the purposes of mission simulations, an initial state error is specified in one of two ways: 1) input an initial state error, or 2) generate a random state error. When the second method is used, the components of the error vector are assumed to be uncorrelated with each other and are generated by the method described in the previous paragraphs.

Simulation of the Guidance Correction Errors

The uncertainty in the commanded velocity correction $\Delta\hat{V}$ was assumed to originate from two independent sources: 1) uncertainty in the magnitude of $\Delta\hat{V}$ due to a random error in the total impulse applied by the control rocket, and 2) uncertainty in the orientation of the correction vector due to random errors in the direction of the thrust vector. The error model adopted for this study and derived below was first proposed by Battin⁽¹²⁾.

Consider a coordinate system with the z-axis oriented along the commanded correction vector $\Delta\hat{V}$ as shown in Fig. 6. In the reference coordinate system the correction vector is given by

$$\Delta\hat{V} = |\Delta\hat{V}| D \begin{bmatrix} 0 \\ 0 \\ 1 \end{bmatrix} \quad (2.40)$$

where D is the transformation matrix which relates the new coordinate system to the reference coordinate system.

With the assumption that the error in the magnitude of the correction is a proportional error, the magnitude of the actual correction can be written

$$|\Delta V| = (1 + \kappa) |\Delta\hat{V}| \quad (2.41)$$

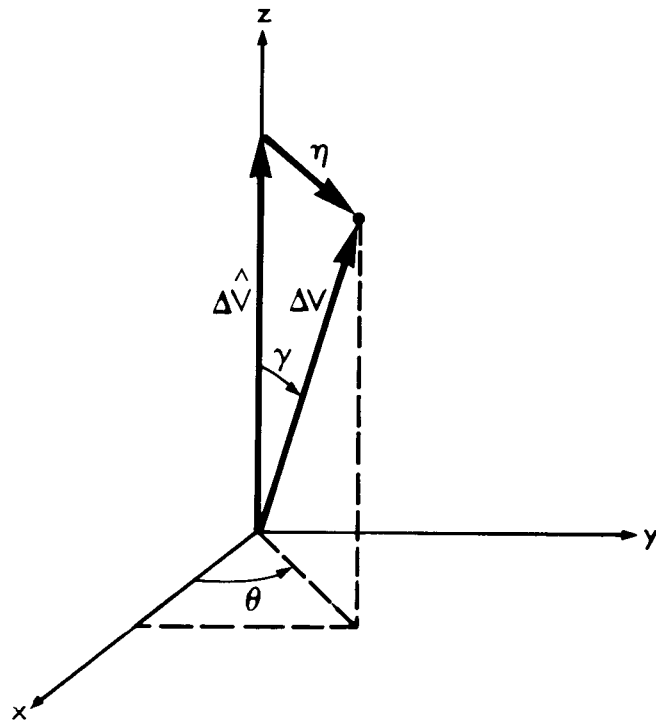


Figure 6 Guidance Correction Geometry

where κ is a small random variable. The actual correction vector is then given by

$$\Delta V = (1 + \kappa) |\Delta \hat{V}| D \begin{bmatrix} \sin \gamma \cos \theta \\ \sin \gamma \sin \theta \\ \cos \gamma \end{bmatrix} \quad (2.42)$$

where γ is a small positive random variable and θ is a random variable which is uniformly distributed in the interval $-\pi$ to π . The error parameters κ , γ , and θ are assumed to be statistically independent. The error in the velocity correction vector can be expressed as

$$\eta = \Delta V - \Delta \hat{V} \quad (2.43)$$

With the small angle assumption for γ , Eq. (2.43) can be written

$$\eta = |\Delta \hat{V}| D \left\{ (1 + \kappa) \gamma \begin{bmatrix} \cos \theta \\ \sin \theta \\ 0 \end{bmatrix} + \kappa \begin{bmatrix} 0 \\ 0 \\ 1 \end{bmatrix} \right\} \quad (2.44)$$

Now consider the covariance N of the error vector η , i.e.,

$$N = \text{cov} [\eta] = E[\eta\eta^T] \quad (2.45)$$

Substitution of Eq. (2.44) into Eq. (2.45) yields

$$N = E[\kappa^2] E[\Delta \hat{V} \Delta \hat{V}^T] + E[\gamma^2] (1 + \kappa^2) D \begin{bmatrix} 1 & 0 & 0 \\ 0 & 1 & 0 \\ 0 & 0 & 0 \end{bmatrix} D^T \quad (2.46)$$

Neglecting the term involving κ^2 and simplifying, Eq. (2.46) becomes

$$N = \sigma_\kappa^2 V + \frac{\sigma_\gamma^2}{2} [(\text{Trace } V)I - V] \quad (2.47)$$

$$V = E[\Delta \hat{V} \Delta \hat{V}^T]$$

where κ and γ are assumed to be distributed with zero mean and known variances $\sigma_{\kappa}^2 = E[\kappa^2]$, and $\sigma_{\gamma}^2 = E[\gamma^2]$.

2.4 Linear Estimation Theory

When the dynamical system and the observational relationships can be satisfactorily approximated by linear equations, Eqs. (2.12) and (2.19) respectively, the well developed theory of linear estimation can be employed to determine the "best" estimate of the state. The statistical principle of maximum likelihood is used here to derive a sequential estimation algorithm for interplanetary navigation. The procedure followed is described in greater detail in Reference 13. Under the assumptions of this study the resulting algorithm is the same as that obtained using the principle of minimum variance.

The estimation problem considered here can be stated as follows. Find the maximum likelihood estimate \hat{x}_k of the epoch state x_k given the sequence of observation vectors y_1, y_2, \dots, y_m which contain random errors. Because the initial state (injection condition) x_0 is unknown and because the mathematical model used to describe the dynamical system is inexact, the true epoch state x_k is never known.

Maximum Likelihood Estimation

Consider a set of m independent random samples y_1, y_2, \dots, y_m drawn from a population characterized by the joint probability density function

$$p(y_1, y_2, \dots, y_m; x) = p_1(y_1, x) p_2(y_2, x) \dots p_m(y_m, x)$$

where x is a parameter of the distribution. The likelihood function is defined as

$$L = \prod_{i=1}^m p_i(y_i, x) . \quad (2.48)$$

The value of x which maximizes Eq. (2.48) is defined as the best estimate \hat{x} (in the maximum likelihood sense) and is called the maximum likelihood estimate of x .

The Maximum Likelihood Principle may be stated as follows: select \hat{x} to maximize the probability of the occurrence of the sample actually observed. That is to say, of all possible samples the one that was actually observed is the one most likely, and therefore x should be chosen to maximize the probability of its occurrence.

Statistical Assumptions

Consider the m linear observation-state relationships

$$y_i = H_i x_k + \varepsilon_i ; \quad i = 1, 2, \dots, m \quad (2.49)$$

where ε_i , the observation error vectors, are assumed to be normally distributed about a zero mean and to have a known covariance R , i.e.,

$$E[\varepsilon_i] = 0 , \quad E[\varepsilon_i \varepsilon_j^T] = R \delta_{ij} ; \quad i, j = 1, 2, \dots, m \quad (2.50)$$

where δ_{ij} is the kronecker delta, i.e., $\delta_{ij} = 0$, if $i \neq j$ and $\delta_{ij} = 1$, if $i = j$. Hence, it is assumed that the observation errors are not correlated in time, i.e.,

$$E[\varepsilon_i \varepsilon_j^T] = \phi ; \quad i \neq j . \quad (2.51)$$

The injection condition, x_o , and the error in its estimate, $\tilde{x}_o = x_o - \hat{x}_o$, are assumed to have the following apriori statistics:

$$\begin{aligned} E[\tilde{x}_o] &= E[x_o] = 0 \\ E[\tilde{x}_o \tilde{x}_o^T] &= E[x_o x_o^T] = P_o . \end{aligned} \quad (2.52)$$

It is further assumed that the injection condition, x_0 , and the observation errors, ϵ_k , are not correlated, i.e.,

$$E[x_0 \epsilon_k^T] = 0, \quad \text{for all } k. \quad (2.53)$$

The Likelihood Function

The best estimate of the actual state deviation vector x_k will be the vector \hat{x}_k which maximizes the likelihood function

$$L = p(y_1, y_2, \dots, y_m, x_k) = p(y_1, \dots, y_m | x_k) p(x_k) \quad (2.54)$$

where $p(y_1, y_2, \dots, y_m, x_k)$ is the joint density function of observations and state deviation x_k and where $p(x_k)$ is the density function of the random state vector x_k . If no a priori statistics on x_0 are considered then $p(x_k)$ is constant and the problem reduces to maximizing the conditional density function $p(y_1, y_2, \dots, y_m | x_k)$.

Given the multivariate Gaussian density function for the observation error vector ϵ_i

$$p(\epsilon_i) = (2\pi)^{-p/2} |R_i|^{-1/2} \exp[-\frac{1}{2} \epsilon_i^T R_i^{-1} \epsilon_i] \quad (2.55)$$

and introducing the transformation

$$\epsilon_i = y_i - H_i x_k \quad (2.56)$$

the following conditional density function is obtained:

$$p(y_i | x_k) = (2\pi)^{-p/2} |R_i|^{-1/2} \exp[-\frac{1}{2} (y_i - H_i x_k)^T R_i^{-1} (y_i - H_i x_k)]. \quad (2.57)$$

With the assumption that the observation vectors are uncorrelated in time, the conditional density function can be written

$$\begin{aligned}
p(y_1, y_2, \dots, y_m | x_k) &= \prod_{i=1}^m p(y_i | x_k) \\
&= (2\pi)^{-\frac{pm}{2}} \prod_{i=1}^m |R_i|^{-\frac{1}{2}} \exp[-\frac{1}{2} \sum_{i=1}^m (y_i - H_i x_k)^T R_i^{-1} (y_i - H_i x_k)] .
\end{aligned} \tag{2.58}$$

Assuming that the true state is normally distributed about a mean conditioned on apriori information only, the density function for x_k can be written

$$p(x_k) = 2\pi^{-n/2} |\bar{P}_k|^{-\frac{1}{2}} \exp[-\frac{1}{2}(x_k - \bar{x}_k)^T \bar{P}_k^{-1}(x_k - \bar{x}_k)] \tag{2.59}$$

where $\bar{x}_k = \Phi(t_k, t_0)\bar{x}_0$ is the mean at time t_k , $\bar{x}_0 = \hat{x}_0$ is the apriori mean, and $\bar{P}_k = \Phi(t_k, t_0)P_0 \Phi(t_k, t_0)^T$ is the apriori state covariance matrix mapped to time t_k .⁽¹³⁾

From Eqs. (2.53) and (2.54) the likelihood function Eq. (2.49) can be written

$$\begin{aligned}
L &= (2\pi)^{-(mp+n)/2} |R|^{-m/2} |\bar{P}_k|^{\frac{1}{2}} \exp\{-\frac{1}{2}[\sum_{i=1}^m (y_i - H_i x_k)^T R_i^{-1}(y_i - H_i x_k) \\
&\quad + (x_k - \bar{x}_k)^T \bar{P}_k^{-1}(x_k - \bar{x}_k)]\} .
\end{aligned} \tag{2.60}$$

Maximizing the Likelihood Function

Since $\log L$ is a monotonic function and reaches its maximum value when L is a maximum, maximizing $\log L$ is equivalent to maximizing L . For convenience define

$$J = \log L = J_1 - \frac{1}{2} J_2 \tag{2.61}$$

where

$$J_1 = \log[(2\pi)^{-(mp+n)/2} |R|^{-m/2} |\bar{P}_k|^{-1/2}], \quad (2.62)$$

$$J_2 = \sum_{i=1}^m (y_i - H_i x_k)^T R_i^{-1} (y_i - H_i x_k) \\ + (x_k - \bar{x}_k)^T \bar{P}_k^{-1} (x_k - \bar{x}_k). \quad (2.63)$$

For J to be a maximum with respect to the choice of x_k requires that the term J_2 be a minimum. For an extremal solution the first variation of J_2 must vanish, i.e.,

$$\delta J_2 = 0 = \sum_{i=1}^m [-(y_i - H_i \hat{x}_k)^T R_i^{-1} H_i \delta x_i \\ - (H_i \delta x_k)^T R_i^{-1} (y_i - H_i \hat{x}_k)] \\ + (\hat{x}_k - \bar{x}_k)^T \bar{P}_k^{-1} \delta x_k + \delta x_k^T \bar{P}_k^{-1} (x_k - \bar{x}_k) \quad (2.64)$$

where \hat{x}_k is that value of x_k which maximizes L .

Since the first two terms on the right hand side are the scalar transpose of each other, they are equal. Likewise the second two terms are equal. Since δx_k is arbitrary, it is necessary that

$$\sum_{i=1}^m [-H_i^T R_i^{-1} (y_i - H_i \hat{x}_k)] + \bar{P}_k^{-1} (\hat{x}_k - \bar{x}_k) = 0. \quad (2.65)$$

Grouping terms leads to

$$\left[\sum_{i=1}^m H_i^T R_i^{-1} H_i + \bar{P}_k^{-1} \right] \hat{x}_k = \left[\sum_{i=1}^m H_i^T R_i^{-1} y_i + \bar{P}_k^{-1} \bar{x}_k \right].$$

If the matrix which multiplies x_k is non-singular the maximum likelihood estimate can be obtained as

$$\hat{x}_k = \left[\sum_{i=1}^m H_i^T R_i^{-1} H_i + \bar{P}_k^{-1} \right]^{-1} \left[\sum_{i=1}^m H_i^T R_i^{-1} y_i + \bar{P}_k^{-1} \bar{x}_k \right] \quad (2.66)$$

To insure that the solution obtained is a minimum the second variation of J_2 with respect to x_k must be positive definite, i.e.,

$$\sigma^2 J_2 = \delta x_k^T \left[\sum_{i=1}^m H_i^T R_i^{-1} H_i + \bar{P}_k^{-1} \right] \delta x_k > 0 . \quad (2.67)$$

Therefore, for Eq. (2.66) to maximize the likelihood function, Eq. (2.67) must be satisfied.

Batch Processing

Equation (2.66) can be used to compute the best estimate of the epoch state, \hat{x}_k , given the observation vectors y_1, \dots, y_m and apriori statistics \bar{x}_0 and P_0 . The procedure is called "batch processing" if all the observations are processed in a single batch. Several points regarding Eq. (2.66) should be noted before proceeding:

- 1) The solution requires the processing of all observational data.
- 2) The solution requires the inversion of an $n \times n$ matrix (first bracketed matrix in Eq. (2.66)).
- 3) If no apriori data is considered, at least n independent scalar measurements must be processed to insure that the matrix to be inverted is full rank.
- 4) If apriori information is available, a single scalar observation can be processed to provide a new estimate for all n components of the state vector.
- 5) After processing all observational data to obtain a solution for the initial state x_0 , a new nominal trajectory may be generated and the data reprocessed to obtain an improved estimate for x_0 . Successive iterations will reduce errors caused by nonlinear effects.

Sequential State Estimation

For the special case when a single p-vector of observations is processed (i.e., $m = 1$) and the i^{th} observation coincides with the epoch time t_k , Eq. (2.66) reduces to

$$\hat{x}_k = (H_k^T R^{-1} H_k + \bar{P}_k^{-1})^{-1} (H_k^T R^{-1} y_k + \bar{P}_k^{-1} \bar{x}_k). \quad (2.68)$$

It can be shown in a straightforward manner that the first term on the left hand side of Eq. (2.64) is the covariance matrix of the estimate error $\tilde{x} = x - \hat{x}$, i.e.,

$$\begin{aligned} P_k &= E[(x_k - \hat{x}_k)(x_k - \hat{x}_k)^T] \\ &= (H_k^T R^{-1} H_k + \bar{P}_k^{-1})^{-1} \end{aligned} \quad (2.69)$$

Note that \bar{x}_k and \bar{P}_k can be obtained by mapping \hat{x}_{k-1} and P_{k-1} through the transition matrix⁽⁹⁾, i.e.,

$$\bar{x}_k = \Phi(t_k, t_{k-1}) \hat{x}_{k-1} \quad (2.70)$$

$$\bar{P}_k = \Phi(t_k, t_{k-1}) P_{k-1} \Phi^T(t_k, t_{k-1}). \quad (2.71)$$

Thus Eq. (2.68) can be used to sequentially estimate the state after each observation. Note, however, that the solution of Eq. (2.68) requires the inversion of the $n \times n$ matrix, $(H_k^T R^{-1} H_k + \bar{P}_k^{-1})$. The order of the matrix inversion required to compute P_k can be reduced from $n \times n$ to $p \times p$ by application of the Schur identity to Eq. (2.68). The result, derived in Appendix D, is

$$P_k = \bar{P}_k - \bar{P}_k H_k^T (H_k \bar{P}_k H_k^T + R)^{-1} H_k \bar{P}_k. \quad (2.72)$$

Eq. (2.72) offers two important computational advantages over Eq. (2.69). First, the matrix inversion required is of the order $p \times p$ rather than $n \times n$.

In particular, if a single observation is made ($p=1$), Eq. (2.72) requires only a scalar division. Secondly, Eq. (2.72) does not require the inverse of matrix \bar{P}_k as does Eq. (2.69).

It will be convenient in the discussion which follows to define the $n \times p$ matrix

$$K_k = \bar{P}_k H_k^T (H_k \bar{P}_k H_k^T + R)^{-1} . \quad (2.73)$$

Eq. (2.72) can then be expressed as

$$P_k = (I - K_k H_k) \bar{P}_k . \quad (2.74)$$

Substituting Eq. (2.74) into Eq. (2.68) leads to

$$\hat{x}_k = (I - K_k H_k) \bar{P}_k (H_k^T R^{-1} y_k + \bar{P}_k^{-1} \bar{x}_k) \quad (2.75)$$

which can be rearranged to give

$$\hat{x}_k = (I - K_k H_k) \bar{x}_k + (I - K_k H_k) \bar{P}_k H_k^T R^{-1} y_k . \quad (2.76)$$

The coefficient of y_k in Eq. (2.76) is just K_k as is shown in the following development:

$$\begin{aligned} (I - K_k H_k) \bar{P}_k H_k^T R^{-1} &= \bar{P}_k H_k^T R^{-1} - \bar{P}_k H_k^T (H_k \bar{P}_k H_k^T + R)^{-1} H_k \bar{P}_k H_k^T R^{-1} \\ &= \bar{P}_k H_k^T [R^{-1} - (H_k \bar{P}_k H_k^T + R)^{-1} H_k \bar{P}_k H_k^T R^{-1}] \\ &= \bar{P}_k H_k^T (H_k \bar{P}_k H_k^T + R)^{-1} [(H_k \bar{P}_k H_k^T + R) R^{-1} - H_k \bar{P}_k H_k^T R^{-1}] \\ &= \bar{P}_k H_k^T (H_k \bar{P}_k H_k^T + R)^{-1} \\ &= K_k \end{aligned} \quad (2.77)$$

Thus Eq. (2.71) can be written

$$\hat{x}_k = \bar{x}_k - K_k H_k \bar{x}_k + K_k y_k \quad (2.78)$$

which can be rearranged to give

$$\hat{x}_k = \bar{x}_k + K_k (y_k - H_k \bar{x}_k) . \quad (2.79)$$

Sequential Estimation Algorithm

The computational algorithm for the sequential estimation scheme derived here can be summarized as follows:

- 1) Given the observation Y_k at the current time t_k , and \hat{x}_{k-1} and P_{k-1} at the previous observation time t_{k-1} :
- 2) Integrate $\dot{X} = F(X,t)$ from t_{k-1} to t_k with initial condition $X(t_{k-1}) = X^*(t_{k-1})$ to obtain $X^*(t_k)$.
- 3) Integrate $\dot{\Phi} = A\Phi$ from t_{k-1} to t_k with initial condition $\Phi_{k-1} = I$ to obtain $\Phi(t_k, t_{k-1})$.
- 4) Compute $Y_k^* = G(X_k^*, t_k)$ and evaluate $y_k = Y_k - Y_k^*$.
- 5) Evaluate H_k using $X^*(t_k)$.
- 6) Compute \bar{x}_k and \bar{P}_k from

$$\begin{aligned} \bar{x}_k &= \Phi(t_k, t_{k-1}) \hat{x}_{k-1} \\ \bar{P}_k &= \Phi(t_k, t_{k-1}) P_{k-1} \Phi^T(t_k, t_{k-1}). \end{aligned}$$

- 7) Compute K_k from

$$K_k = \bar{P}_k H_k^T (H_k \bar{P}_k H_k^T + R)^{-1}.$$

- 8) Compute \hat{x}_k and P_k from

$$\hat{x}_k = \bar{x}_k + K_k [y_k - H_k \bar{x}_k]$$

$$P_k = [I - K_k H_k] \bar{P}_k.$$

- 9) Store \hat{x}_k and P_k .
- 10) Repeat the process at the next observation time t_{k+1} .

2.5 Guidance Theory

The purpose of the guidance system is to provide the necessary control of the velocity vector to achieve specified mission objectives. For this study the mission objectives are specified in terms of a 3-vector of targeting parameters. The impulsive velocity change required to null the predicted deviation in the targeting vector is expressed as a function of the state deviation. With the usual assumption of small state deviations, a guidance law is derived which expresses the commanded velocity correction $\Delta \hat{V}$ as a linear function of the state estimate \hat{x} . This linearization makes possible the development of a simple computational algorithm for planetary approach guidance.

Targeting Vector

In general, the targeting vector T is some nonlinear function of the state, i.e.,

$$T = T(\bar{r}, \bar{v}). \quad (2.80)$$

For this study the targeting vector was defined as

$$T = \begin{bmatrix} B \cdot R \\ B \cdot T \\ t_e \end{bmatrix} \quad (2.81)$$

where t_e is the time of encounter and where $B \cdot R$ and $B \cdot T$ are projections of the targeting vector \bar{B} along the ordinate and abscissa of the R-T coordinate system defined in Appendix F. The vector \bar{B} is the normal vector directed from the center of the target planet to the approach asymptote.

Expanding Eq. (2.80) about the nominal trajectory and neglecting terms of order higher than the first yields

$$T = T^* + \left[\frac{\partial T}{\partial \bar{r}} \right]^* \delta \bar{r} + \left[\frac{\partial T}{\partial \bar{v}} \right]^* \delta \bar{v} . \quad (2.82)$$

When the deviations $\delta \bar{r}$ and $\delta \bar{v}$ are small enough so that this linearization is valid, the deviation of the targeting vector before and after the guidance correction can be written

$$\delta T^- = M_1 \delta \bar{r} + M_2 \delta \bar{v}^- \quad (2.83)$$

$$\delta T^+ = M_1 \delta \bar{r} + M_2 \delta \bar{v}^+ \quad (2.84)$$

where

$$M_1 = \left[\frac{\partial T}{\partial \bar{r}} \right]^*$$

$$M_2 = \left[\frac{\partial T}{\partial \bar{v}} \right]^*$$

and $()^-$ and $()^+$ indicate quantities just before and after the correction.

Solving Eqs. (2.83) and (2.84) for the required correction gives

$$\Delta V = \delta \bar{v}^+ - \delta \bar{v}^- = M_2^{-1} [\delta T^+ - \delta T^-] \quad (2.85)$$

Substituting back in for δT^- gives

$$\Delta V = M_2^{-1} [\delta T^+ - (M_1 \delta \bar{r} + M_2 \delta \bar{v}^-)] . \quad (2.86)$$

Assuming a full correction is made, $\delta T^+ = 0$ and Eq. (2.86) becomes

$$\Delta V = -M_2^{-1} M_1 \delta \bar{r} - I \delta \bar{v} \quad (2.87)$$

Recalling that

$$x = \begin{bmatrix} \delta \bar{r} \\ \delta \bar{v} \end{bmatrix}$$

Eq. (2.87) can be written

$$\Delta V = Bx \quad (2.88)$$

where $B = [-M_2^{-1} M_1 \mid -I]$.

Updating the State Estimate Error Covariance Matrix, P

Eq. (2.88) expresses the velocity correction required to null the target error as a linear function of the deviation of the actual state from the nominal state. However, since the actual state is never known, it is necessary to compute the commanded guidance correction from the best estimate of the state \hat{x} , i.e.,

$$\Delta \hat{V} = B\hat{x}. \quad (2.89)$$

Considering execution errors, the actual correction will be

$$\Delta V' = \Delta \hat{V} + \eta. \quad (2.90)$$

where η , the execution error vector, is assumed to be distributed with zero mean and known covariance N , i.e.,

$$N = E[\eta\eta^T] \quad (2.91)$$

as defined by Eq. (2.47).

If a full correction is made, the new state estimate becomes

$$\hat{x}^+ = \hat{x}^- + J\Delta\hat{V} \quad (2.92)$$

where $J = \begin{bmatrix} 0 \\ -\mathbf{I} \end{bmatrix}$ is a 6x3 compatibility matrix. The error in the state estimate after the correction is given by

$$\tilde{x}^+ = \tilde{x}^- + J\eta. \quad (2.93)$$

The state estimate covariance matrix after the correction is defined by

$$P^+ = E[\tilde{x}^+ \tilde{x}^{+T}]. \quad (2.94)$$

Substituting for \tilde{x}^+ yields

$$P^+ = E[\tilde{x}^- \tilde{x}^{-T} + \tilde{x}^- \eta^T J^T + J\eta \tilde{x}^{-T} + J\eta\eta^T J^T]. \quad (2.95)$$

With the assumption that the execution errors and the state estimate errors are uncorrelated (i.e., $E[\tilde{x}^- \eta^T] = 0$), the covariance of \tilde{x}^+ becomes

$$P^+ = P^- + JNJ^T \quad (2.96)$$

where $P^- = E[\tilde{x}^- \tilde{x}^{-T}]$ and $N = E[\eta\eta^T]$.

Updating the State Error Covariance Matrix, S

Consider the update of the state error vector

$$x^+ = x^- + J\Delta V'. \quad (2.97)$$

Using Eqs. (2.89) and (2.90) gives

$$x^+ = x^- + JB\hat{x}^- + J\eta. \quad (2.98)$$

Substituting for \hat{x} yields

$$x^+ = x^- + JB(x-\hat{x})^- + J\eta \quad (2.99)$$

and thus

$$\mathbf{x}^+ = (\mathbf{I} + \mathbf{JB})\mathbf{x}^- - \mathbf{JB}\tilde{\mathbf{x}}^- + \mathbf{J}\eta . \quad (2.100)$$

The state error covariance matrix after the guidance correction can be written

$$\mathbf{S}^+ = \mathbf{E}[\mathbf{x}^+ \mathbf{x}^{+T}] . \quad (2.101)$$

Substitution of Eq. (2.100) into Eq. (2.101) yields

$$\begin{aligned} \mathbf{S}^+ = & \mathbf{E}[(\mathbf{I} + \mathbf{JB})\mathbf{x}^- \mathbf{x}^{-T} (\mathbf{I} + \mathbf{JB})^T - \mathbf{JB}\tilde{\mathbf{x}}^- \mathbf{x}^{-T} (\mathbf{I} + \mathbf{JB})^T \\ & - (\mathbf{I} + \mathbf{JB})\mathbf{x}^- \tilde{\mathbf{x}}^{-T} \mathbf{B}^T \mathbf{J}^T - \mathbf{J}\eta \mathbf{x}^{-T} (\mathbf{I} + \mathbf{JB})^T \\ & + \mathbf{JB}\tilde{\mathbf{x}}^- \tilde{\mathbf{x}}^{-T} \mathbf{B}^T \mathbf{J}^T - \mathbf{J}\eta \tilde{\mathbf{x}}^{-T} \mathbf{B}^T \mathbf{J}^T + \mathbf{J}\eta \eta^T \mathbf{J}^T] . \end{aligned} \quad (2.102)$$

Before simplifying Eq. (2.102), consider the correlation of the state estimate error $\tilde{\mathbf{x}}$ and the state deviation \mathbf{x} , i.e.,

$$\begin{aligned} \mathbf{E}[\tilde{\mathbf{x}} \mathbf{x}^T] &= \mathbf{E}[\tilde{\mathbf{x}} (\tilde{\mathbf{x}} + \hat{\mathbf{x}})^T] \\ \mathbf{E}[\tilde{\mathbf{x}} \mathbf{x}^T] &= \mathbf{E}[\tilde{\mathbf{x}} \tilde{\mathbf{x}}^T] + \mathbf{E}[\tilde{\mathbf{x}} \hat{\mathbf{x}}^T] . \end{aligned} \quad (2.103)$$

Using the property that the state estimate and the error in the state estimate are uncorrelated⁽¹⁴⁾, Eq. (2.103) becomes

$$\mathbf{E}[\tilde{\mathbf{x}} \mathbf{x}^T] = \mathbf{P} . \quad (2.104)$$

Furthermore, the execution error is assumed to be statistically independent of both the state deviation and the state estimate error, i.e.,

$$\mathbf{E}[\eta \mathbf{x}^T] = \mathbf{E}[\eta \tilde{\mathbf{x}}^T] = \mathbf{0} . \quad (2.105)$$

Using Eqs. (2.104) and (2.105) and the symmetry property of the covariance matrix (i.e., $\mathbf{P}^T = \mathbf{P}$), Eq. (2.102) can be simplified to yield

$$S^+ = (I + JB)(S^- - P^-)(I + JB)^T + P^- + JNJ^T . \quad (2.106)$$

Recalling Eq. (2.96)

$$S^+ = (I + JB)(S^- - P^-)(I + JB)^T + P^+ . \quad (2.107)$$

Eq. (2.107) is the update equation for the state deviation covariance matrix when a guidance correction is made.

Velocity Correction Covariance Matrices

Although the true velocity correction, ΔV , is never known its covariance matrix can be expressed as

$$E[\Delta V \Delta V^T] = E[Bx^- x^-^T B^T] = BS^-B^T . \quad (2.108)$$

Likewise, the covariance matrix of the error in the estimate of the required correction, U , can be expressed by

$$U = E[(\Delta V - \Delta \hat{V})(\Delta V - \Delta \hat{V})^T] . \quad (2.109)$$

Substitution of Eqs. (2.88) and (2.89) into Eq. (2.109) leads to the following development:

$$\begin{aligned} U &= E[(Bx^- - B\hat{x})(Bx^- - B\hat{x})^T] \\ U &= B E[(x^- - \hat{x})(x^- - \hat{x})^T] B^T \\ U &= B P^- B^T . \end{aligned} \quad (2.110)$$

The covariance matrix of the commanded velocity correction, $\Delta \hat{V}$, is defined by

$$V = E[\Delta \hat{V} \Delta \hat{V}^T] . \quad (2.111)$$

Substitution of Eq. (2.89) into Eq. (2.111) yields

$$\begin{aligned}
 V &= E[B \hat{x} \hat{x}^T B^T] \\
 V &= BEx^- - \tilde{x}^-^T B^T \\
 V &= BE[x^- x^{-T} - x^- \tilde{x}^{T} - \tilde{x}^- x^{-T} + \tilde{x}^- \tilde{x}^{-T}] B^T \\
 V &= B[S^- - P^-] B^T
 \end{aligned} \tag{2.112}$$

since $E[x^- \tilde{x}^{-T}] = 0$.

Statistics of the Magnitude of the Velocity Correction

Under the assumptions of this study, the commanded velocity correction can be characterized by the following statistics:

$$E[\Delta \hat{V}] = \phi \tag{2.113}$$

$$E[\Delta \hat{V} \Delta \hat{V}^T] = V \tag{2.114}$$

where the expectation is taken over the ensemble of all possible trajectories. However, to evaluate guidance propulsion requirements the statistics of the magnitude of the correction, $|\Delta \hat{V}|$, are needed. Unfortunately the mean and variance of $|\Delta \hat{V}|$ are not readily obtained from Eqs. (2.113) and (2.114). Guidance requirements in Chapter 4 are expressed in terms of the RMS (root-mean-square) value of $|\Delta \hat{V}|$ given by⁽¹²⁾

$$\Delta V_{\text{rms}} = \sqrt{\text{Trace } V} \quad . \tag{2.115}$$

Statistics of the Targeting Error

The actual error in the targeting vector is given by

$$\delta T = T - T^* = Bx. \tag{2.116}$$

The covariance of the error is defined by

$$\text{cov}[\delta T] = E[\delta T \delta T^T] = E[Mx x^T M^T] \quad (2.117)$$

where $M = \left[\frac{\partial T}{\partial x} \right]^* = [M_1 \mid M_2]^*$.

Since M is deterministic, Eq. (2.117) can be written

$$\text{cov}[\delta T] = MSM^T. \quad (2.118)$$

A convenient parameter for evaluating targeting uncertainty is the target RMS defined by

$$T_{\text{rms}} = \sqrt{\text{Trace}(MSM^T)}. \quad (2.119)$$

Guidance Algorithm

The computational algorithm for the guidance scheme derived in the previous section can be summarized as follows:

Given \hat{x} , P^- and S^- at the correction time t_k :

- (1) Evaluate $\hat{X} = X^* + \hat{x}$, $M_1 = \left[\frac{\partial T}{\partial \bar{r}} \right]^*$ and $M_2 = \left[\frac{\partial T}{\partial \bar{v}} \right]^*$.
- (2) Compute \hat{T} from \hat{X} and evaluate $\delta T = \hat{T} - T^*$. If $|\delta T| < \epsilon$, where ϵ is a small tolerance, skip to step (7), otherwise go to step (3).
- (3) Solve for the linear correction

$$\Delta V = -M_2^{-1} \delta T$$

- (4) Update the state vector $\hat{X} = \hat{X}_{\text{old}} + J\Delta V$
- (5) Evaluate M_1 and M_2 at the new state \hat{X} and repeat steps (2) through (5).
- (6) Form $B = [-M_2^{-1} \mid M_1 \mid -I]$

(7) Compute covariance matrix N from Eq. (2.47)

(8) Update P : $P^+ = P^- + JNJ^T$

(9) Update S : $S^+ = [I + JB][S^- - P^-][I + JB]^T + P^+$

(10) Compute V and Trace V :

$$V = B[S^- - P^-]B^T$$

(11) Compute U and Trace U :

$$U = BP^- B^T$$

(12) Compute ΔV_{rms} : $\Delta V_{\text{rms}} = \sqrt{\text{Trace } V}$

(13) Compute T_{rms} : $T_{\text{rms}} = \sqrt{\text{Trace } MS^+M^T}$.

The derivations presented in this chapter constitute the theoretical basis for the navigation analysis reported in Chapter 4 and the guidance analysis presented in Chapter 5. In selecting algorithms and error models to simulate the navigation and guidance process, special emphasis was placed on methods which are rapid enough to be practical, yet are realistic enough to be meaningful. The computational algorithms and models were incorporated into two computer programs which are described in the following chapter.

CHAPTER 3

COMPUTATIONAL DEVELOPMENT

The computational algorithms derived in Chapter 2 were incorporated into two special purpose computer programs to facilitate the navigation and guidance analysis. The programs, designated STEP V and STEP VI, were developed to satisfy the requirement for efficient research-oriented mission analysis computer programs. They differ only in that STEP V performs in a conventional batch mode while STEP VI is used in an interactive mode. Both programs were designed for operation on the CDC 6600 computer. This chapter contains a general description of the two programs. A more complete documentation is contained in Reference 15.

3.1 Description of the Programs

STEP V is a research-oriented FORTRAN IV computer program designed specifically for the preliminary analysis of interplanetary missions. The program simulates the navigation and guidance process for the encounter phase of a planetary flyby mission. The nominal and the simulated encounter trajectories are generated simultaneously through parallel numerical integrations of the equations of motion. A state transition matrix is generated by numerical integration of the perturbation equations. All integrations are performed with a fourth order Adams-Moulton predictor-corrector scheme using a fourth order Runge-Kutta starter. Observational data are simulated at specified intervals by adding randomly generated errors to observations computed on the "true"

(simulated) trajectory. A linear sequential estimation scheme is used to process the observations and to provide an estimate of the state after each observation. The error in the estimate is computed by differencing the true and the estimated states.

Guidance corrections, which null the estimated error in the target vector, can be executed at specified times. Options are provided to plot time histories of errors in the estimate for the simulated case as well as pertinent properties of the error covariance matrix associated with the state estimate. A basic flow chart of STEP V logic is presented in Figure 7.

STEP VI, an adaptation of STEP V, can perform all of the computational capabilities described above while operating in an interactive mode. The program was designed to take advantage of the interactive graphics capability of the Control Data Corporation 252 Display Console at The University of Texas at Austin. Primary program functions are shown in Figure 8 and described below.

Overall program control is from the console keyboard. Executions of STEP VI subprograms which control (1) problem input, (2) input data manipulation, (3) problem setup, (4) problem execution, (5) output data plotting, and (6) display storage are accomplished by commands from the console keyboard. In addition, certain display instructions can be input directly from the keyboard to the CDC 252 system. Since the program normally occupies central memory for the entire working session, storage requirements were minimized by dividing the program into three functional segments. The control program, which converts the keyboard commands into STEP VI subroutine calls, is the main segment and is always resident in central memory. Segment A, comprised of subroutines which perform functions 1, 2 and 5 shown in Figure 8, is loaded from disk when one of its subroutines is first called by the main segment. Segment B replaces Segment A in central memory when a subroutine which

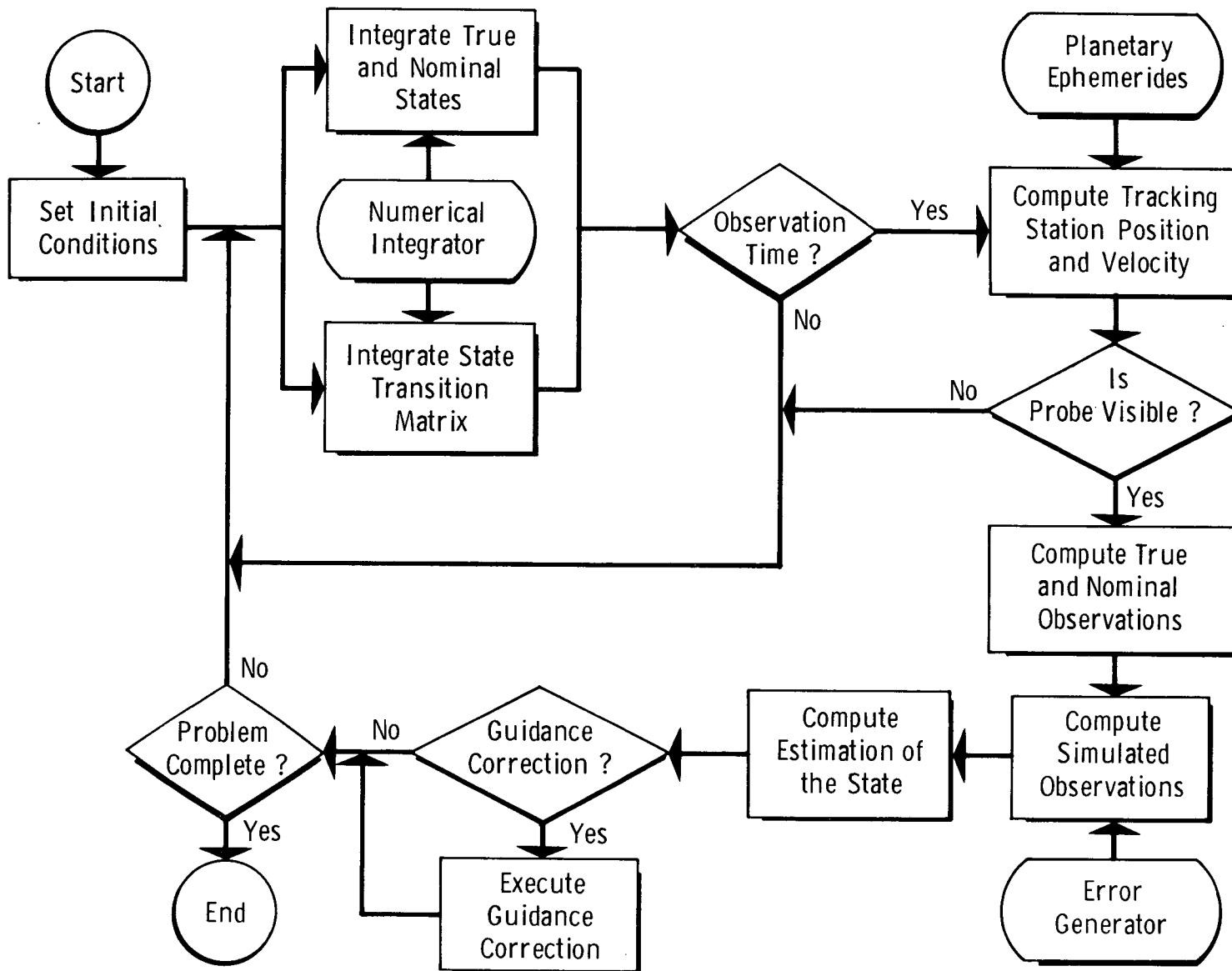


Figure 7 Step V Computational Logic

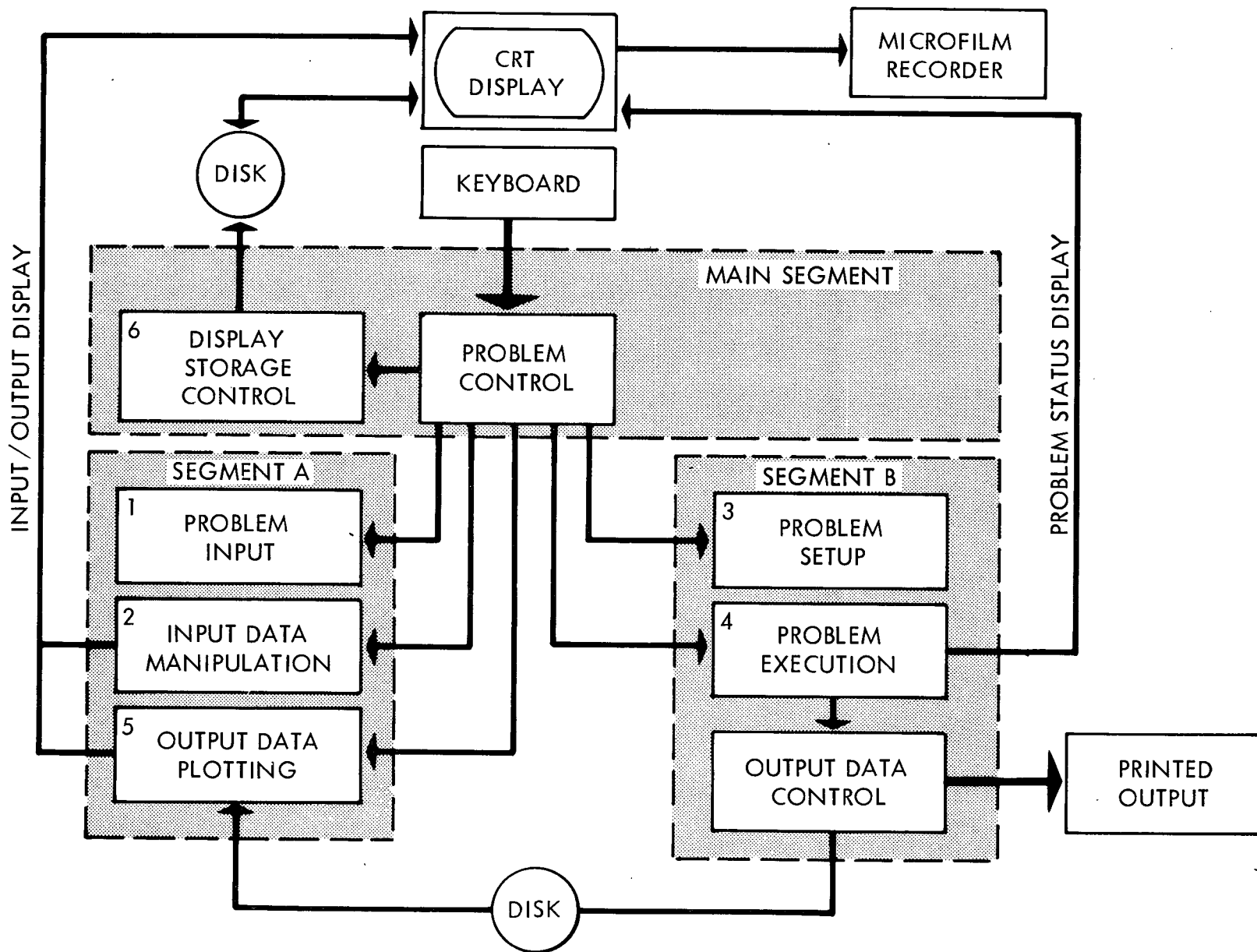


Figure 8 Step VI Program Structure

accomplishes functions 3 or 4 is called by the main segment. To conserve storage, output data generated by Segment B is stored on disk and read off by Segment A when the plotting command is given.

3.2 Description of Interactive Program Operation

An interactive session is initiated by reading the program into the CDC 6600 system input queue as a batch job. When the program is assigned a system control point and update compilations performed (if any), the main segment is loaded and a message is displayed on the CRT to indicate that the program is waiting for a keyboard command. The mission analyst causes the first problem to be loaded by keying in a simple command (the letter "I"). The command causes Segment A to be loaded, the input routine to read the first problem, and a problem identification message to be displayed. The analyst may proceed with the first problem or he may sequence to any other problem by repeating the input command. When the desired problem has been read, the mission analyst can display all input parameters and execute changes to them from the keyboard. Changes are accomplished by typing in two identifying numbers and the new value of the parameter. When a change is executed, the new value is displayed to the right of the original input value. When the analyst is satisfied with all input parameters, he keys in the setup command which causes Segment B to be loaded, all problem setup operations to be performed, and the message "GO" to be displayed.

Numerical integration of the trajectories (nominal and simulated), and thus execution of the problem, are controlled by the keyboard command "GO, I1, I2." The parameter I1 is an integer which specifies the number of integration steps to be performed. The parameter I2 is an integration status display indicator. If the status display option is selected, the current time-to-go (to

encounter) and distance-to-go are displayed on the CRT during execution. If a guidance correction time has been specified, problem execution will stop when the correction time is reached. Pertinent guidance data are automatically displayed at that point. The analyst then has the option to execute the correction and continue, or skip the correction and return problem control to the keyboard. When the specified integration is complete, problem control is automatically returned to the keyboard.

At this point the analyst may plot the data generated on the run just completed by giving a simple plot command. The plot command calls Segment A back into memory and causes selected data to be automatically scaled and plotted on the CRT. By keying in the appropriate commands the plotted data can be recorded directly on microfilm and/or stored on magnetic disk for recall later in the session. Each plot is tagged with the time, the date, and a unique identification number. The tag information is also recorded on the printed output.

After completion of a problem the mission analyst may terminate the session, rerun the problem with new input, or read in a new problem. If a Monte Carlo analysis has been specified in the input data, the analyst need only key in the setup command to generate a new set of initial state-errors.

Central processor time for a typical planetary approach problem averages less than one minute. However, since the program operates in a multi-programming environment, the elapsed session time for the same problem will vary from 2 to 5 minutes. Maximum storage required is 70,000 octal locations.

CHAPTER 4

APPROACH NAVIGATION ANALYSIS

A comprehensive analysis of the approach phase of Jupiter, Saturn and Uranus encounter was made to define reference approach navigation accuracies at those planets. For the purposes of the analysis, the approach phase is defined as that segment of the encounter trajectory extending from the SOI (sphere of influence) to periapsis. This is the critical period in the mission profile when the state of the spacecraft relative to the planet must be determined with sufficient accuracy to permit the execution of one or more guidance corrections.

When the spacecraft reaches the target planets' SOI, the uncertainty in its heliocentric state will have been improved by many months of Earth-based radar tracking data. However, the state of the spacecraft relative to the target planet will be known to a much lesser degree of accuracy due to the relatively large uncertainties remaining in the ephemeris of the outer planets. Approach navigation must reduce this uncertainty to acceptable levels before an effective guidance correction can be performed. Navigation errors which remain at the time of a guidance correction will result in an incorrect guidance execution. If the guidance errors remain uncorrected, they will propagate through the encounter resulting in much larger post-encounter errors.

4.1 Assumed Error Sources

2.4

During the planetary approach phase, navigation errors result from errors in the observations as well as from errors in the assumed dynamical model. For this study, the primary source of error was assumed to be a random noise in the observation. Other sources of observation error not considered in this analysis include errors in the Earth-based tracking station location and center-finding errors inherent in the planet and sun sensors. Since these errors are systematic in nature, they can be reduced significantly by including the biases as parameters to be estimated. The principal source of error in the dynamical model was assumed to be the uncertainty in the position of the outer planets. Another source of model error not considered here is due to the uncertainty in the mass of the planet. As with the other systematic errors the uncertainty can be reduced by including the planet mass as a parameter to be estimated.

Nominal one-sigma values for the assumed error sources are listed in Table 1. These data are based on projected improvements in the accuracy of the Deep Space Network⁽¹⁶⁾. Onboard angle errors are considered to be typical of optical measurement systems currently under development at the Jet Propulsion Laboratory⁽¹⁷⁾. Planet position errors are based on an expected 0.2 arc-sec uncertainty for each planet⁽¹⁸⁾. All error sources used in this study are considered to be on the conservative side of projected values for the late 1970s.

4.2 Reference Navigation Accuracy

Computer simulations of the navigation process for Jupiter, Saturn and Uranus encounter were made for the nominal 1977 Grand Tour mission defined in Chapter 1 and Appendix A. For the purpose of defining reference navigation accuracy data, the following ground rules were adopted:

Table 1 Nominal One-Sigma Values for Assumed Error Sources

Source	One-Sigma Values
Observations:	
Range	15 m
Range-rate	.5 mm/sec
Sun-planet angle	10 arc-sec
Star-planet angle	10 arc-sec
Planet Position:	
Jupiter	750 km
Saturn	1400 km
Uranus	2700 km

- (1) Continuous Earth-based tracking data are available from a single station except when the spacecraft is occulted by the Earth.
- (2) An equivalent data rate of one observation every 144 minutes (0.1 days) for all observation types. A realistic Earth-based data rate (i.e., one observation per minute) is simulated by scaling the nominal observation variance by the ratio of the realistic data rate to the assumed data rate (i.e., the ratio 1/144).
- (3) The error in the location of the Earth-based tracking station is zero.
- (4) The initial state error is zero (initial values of the true and nominal state deviation vectors are equal).
- (5) The a priori estimate of the state deviation is zero ($\hat{x}_0 = 0$). The a priori covariance matrix of the estimate, P_0 , is a diagonal matrix defined in Table 2.

Reference navigation accuracy data are presented in Figures 9 through 27. These results are based on, and subject to the limitations of, the linear estimation theory derived in Chapter 2. The data presented are of three basic types: (1) state estimate uncertainty derived from the state estimate error covariance matrix, (2) target error ellipses derived from the target estimate covariance matrix, and (3) target error data obtained from mission simulations.

State Estimate Uncertainty

Reference state estimate uncertainty during Jupiter, Saturn and Uranus approach are presented in Figures 9 through 11. These data consist

Table 2 Diagonal Elements of the Apriori State Estimate
Covariance Matrix P_0

Element	Jupiter	Saturn	Uranus
P_{011} (km^2)	5.63 (5)	2.00 (6)	7.62 (6)
P_{022} (km^2)	5.63 (3)	2.00 (6)	7.62 (6)
P_{033} (km^2)	5.63 (5)	2.00 (6)	7.62 (6)
P_{044} (km^2/sec^2)	4.00 (-8)	4.00 (-8)	8.00 (-8)
P_{055} (km^2/sec^2)	4.00 (-8)	4.00 (-8)	8.00 (-8)
P_{066} (km^2/sec^2)	4.00 (-8)	4.00 (-8)	8.00 (-8)
P_{077} (km^2)	5.63 (5)	1.96 (6)	7.29 (6)
P_{088} (km^2)	5.63 (5)	1.96 (6)	7.29 (6)
P_{099} (km^2)	5.63 (5)	1.96 (6)	7.29 (6)

of RMS (root-mean-square) values of the uncertainty in the space-craft's planetocentric position and velocity and the heliocentric position of the planet, as well as an overall measure of state uncertainty. RMS uncertainty in position, velocity and planet position are defined by the square root of the sum of the component variances, i.e.,

$$\begin{aligned}
 \text{Position RMS} &= (P_{11} + P_{22} + P_{33})^{\frac{1}{2}} \\
 \text{Velocity RMS} &= (P_{44} + P_{55} + P_{66})^{\frac{1}{2}} \\
 \text{Planet Position RMS} &= (P_{77} + P_{88} + P_{99})^{\frac{1}{2}}
 \end{aligned} \tag{4.1}$$

where the variances $P_{11}, P_{22}, \dots, P_{99}$ are the diagonal elements of the state estimate error covariance matrix. Overall state uncertainty is expressed as the "entropy" of the system. The concept of entropy as a measure of state uncertainty is well accepted in the field of information theory⁽¹⁷⁾. In 1967 Potter and Fraser⁽¹⁸⁾ derived the following expression for the entropy of a sequential estimator as a function of the determinant of the state estimate covariance matrix:

$$\text{Entropy} = (\frac{1}{2})\log_2 |P| + E_0 \tag{4.2}$$

where $E_0 = (n/2)\log_2 (2\pi e)$, n is the dimension of the state vector, and e is the base of the natural logarithm. Although entropy as used here has no physical significance, it is considered a convenient figure-of-merit for overall performance of the navigation process.

State Estimate Uncertainty During Jupiter Approach

Reference navigation accuracy data for the state estimate during Jupiter approach are presented in Figure 9 for (1) range rate, RR, (2) onboard angles, OBA, and (3) range-rate plus onboard angles, RR + OBA.

Time histories of position RMS during Jupiter approach are shown in Figure 9a. From Figure 9a it can be seen that the OBA information alone is not sufficient to reduce significantly the uncertainty in spacecraft position. In fact, the information rate from onboard angles is not adequate to prevent a growth in the position RMS during the period from E-30 (encounter minus 30 days) to E-6 days. Range-rate data alone give much better position accuracy for the same period. A significant overall improvement in position accuracy is achieved by combining range-rate observations with the onboard angle observations.

Velocity RMS time histories for Jupiter approach are shown in Fig. 9b. These data are characterized by a sharp peak in the velocity uncertainty just prior to encounter, followed by a rapid decrease at encounter. This phenomena was observed to occur at each planet for all observation types, and can be explained by the following considerations. The change in the covariance matrix P is governed by two effects, viz., a decrease caused by the information content of the observations and an increase due to the dynamical propagation of the covariance matrix. For a short period just prior to encounter the information rate is not great enough to offset the growth in the velocity elements of the covariance matrix, thus causing the velocity RMS to increase sharply before the information term begins to dominate again. The onboard angle data reduce the uncertainty slightly up to E-12 days at which point the characteristic velocity uncertainty growth begins. Range-rate data give good velocity information up to E-8 days before the velocity uncertainty growth takes over. Onboard angle data combined with range-rate data give only slight improvement along most of the curve but virtually eliminate the velocity uncertainty peak.

Time histories of Jupiter position uncertainty are presented in Fig. 9c. These data show that range-rate observations alone provide a significant

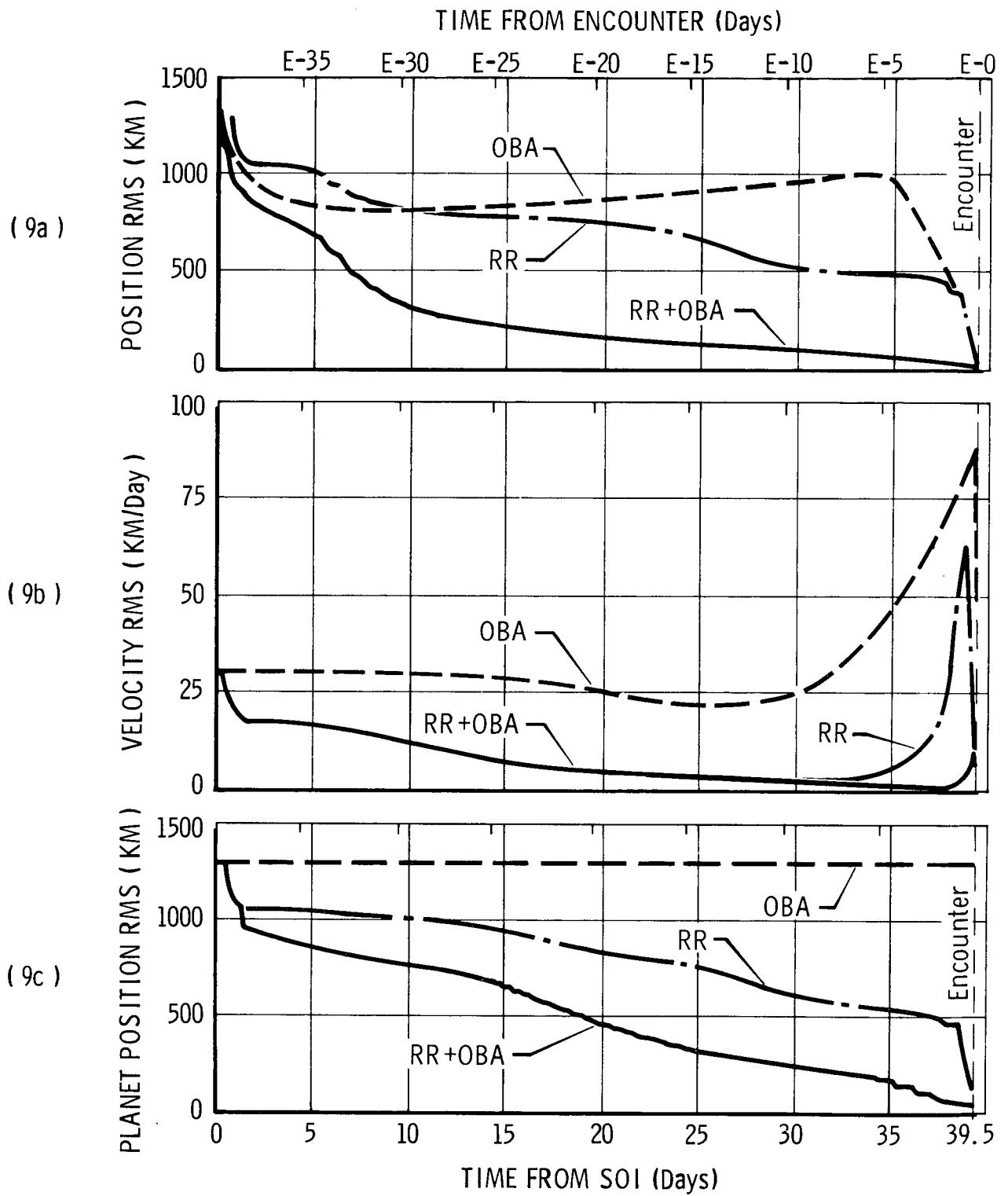


Figure 9 State Estimate Uncertainty During Jupiter Approach

improvement in the position uncertainty of Jupiter while onboard angle measurements alone provide no information. However, range-rate and onboard angle measurements compliment each other to provide a significant overall improvement in Jupiter position uncertainty over the range-rate only case.

State Estimate Uncertainty During Saturn Approach

Reference navigation accuracy data for the state estimate during Saturn approach are presented in Fig. 10 for (1) range-rate, RR (2) onboard angles, OBA, and (3) range-rate plus onboard angles, RR + OBA.

Position RMS time histories, Fig. 10a, show that the onboard angles data give slightly better position accuracy than do the range-rate data up to about E-15. After E-15 the range-rate data is superior and yields much better results near periapsis. As was the case at Jupiter, a combination of range-rate and onboard angle measurements gives much better position accuracy than either range-rate or onboard angles alone. Overall position accuracy is considerably better at Jupiter approach than at Saturn approach.

Velocity RMS time histories for Saturn approach are presented in Figure 10b. As can be seen from Figure 10b range-rate data give a much better velocity estimate than the onboard angle data. For onboard angle data the velocity uncertainty growth starts at about E-5, reaches a peak of 125 km/day and then drops sharply at periapsis. The combined range-rate and onboard angle data give a steady and rapid decrease in velocity uncertainty.

As can be seen from the time histories of Saturn position uncertainty in Fig. 10c, both range-rate data and range-rate plus onboard angle data provide an improved estimate of planet position during approach. The onboard angles alone provide virtually no information regarding planet position.

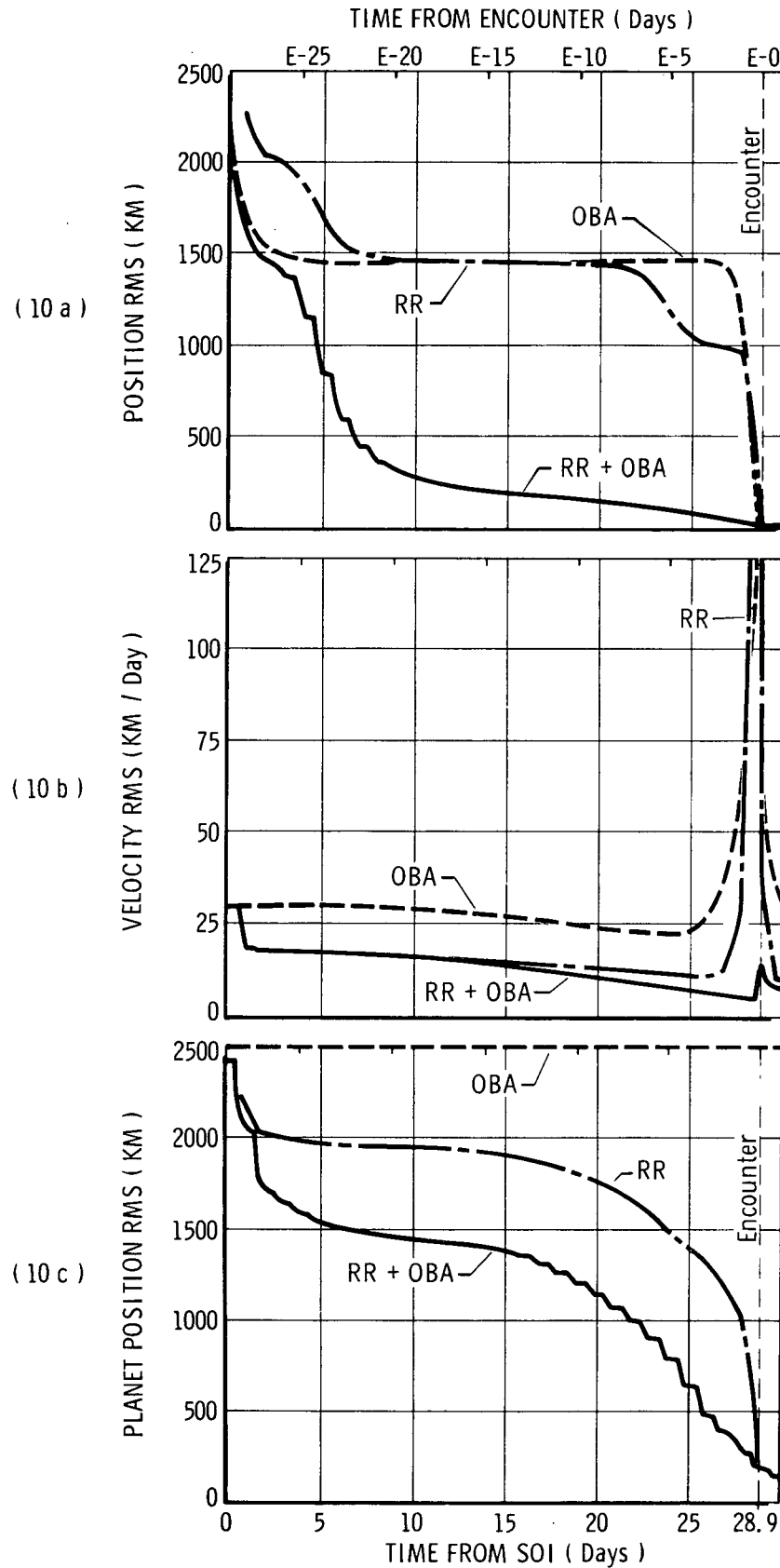


Figure 10 State Estimate Uncertainty During Saturn Approach

State Estimate Uncertainty During Uranus Approach

Reference navigation accuracy data for the state estimate during Uranus approach are presented in Fig. 11 for (1) range-rate, RR, (2) onboard angles, OBA, and (3) range-rate plus onboard angles, RR + OBA.

From the position RMS time histories, Fig. 11a, it can be seen that the onboard angle data provide better position accuracy at Saturn than do the range-rate data up to E-10. After E-10, the range-rate data becomes superior. Range-rate plus onboard data provide a significant improvement over both the range-rate case and the onboard angle case after E-25.

Velocity RMS time histories for Uranus approach are presented in Fig. 11b. As was the case with Jupiter and Saturn, range-rate data provide better velocity accuracy during Uranus approach than do the onboard angle data. Unlike Jupiter and Saturn, however, combining onboard angle data with range-rate data results in a significant decrease in velocity uncertainty throughout Uranus approach.

Time histories of Uranus position RMS are presented in Fig. 11c. Only slight improvement in Uranus position uncertainty can be achieved prior to periapsis passage with range-rate data. Although the onboard angle data alone provide virtually no Uranus position information, they significantly reduce the uncertainty when combined with range-rate data.

Target Estimate Accuracy

Reference navigation accuracy data for Jupiter, Saturn, and Uranus approach target parameters B·R and B·T are shown in Figures 12 through 17. The data consist of target error ellipses in B·R - B·T target space. The error covariance matrix associated with the estimate of the target parameters is used to generate a contour of constant probability which, for the

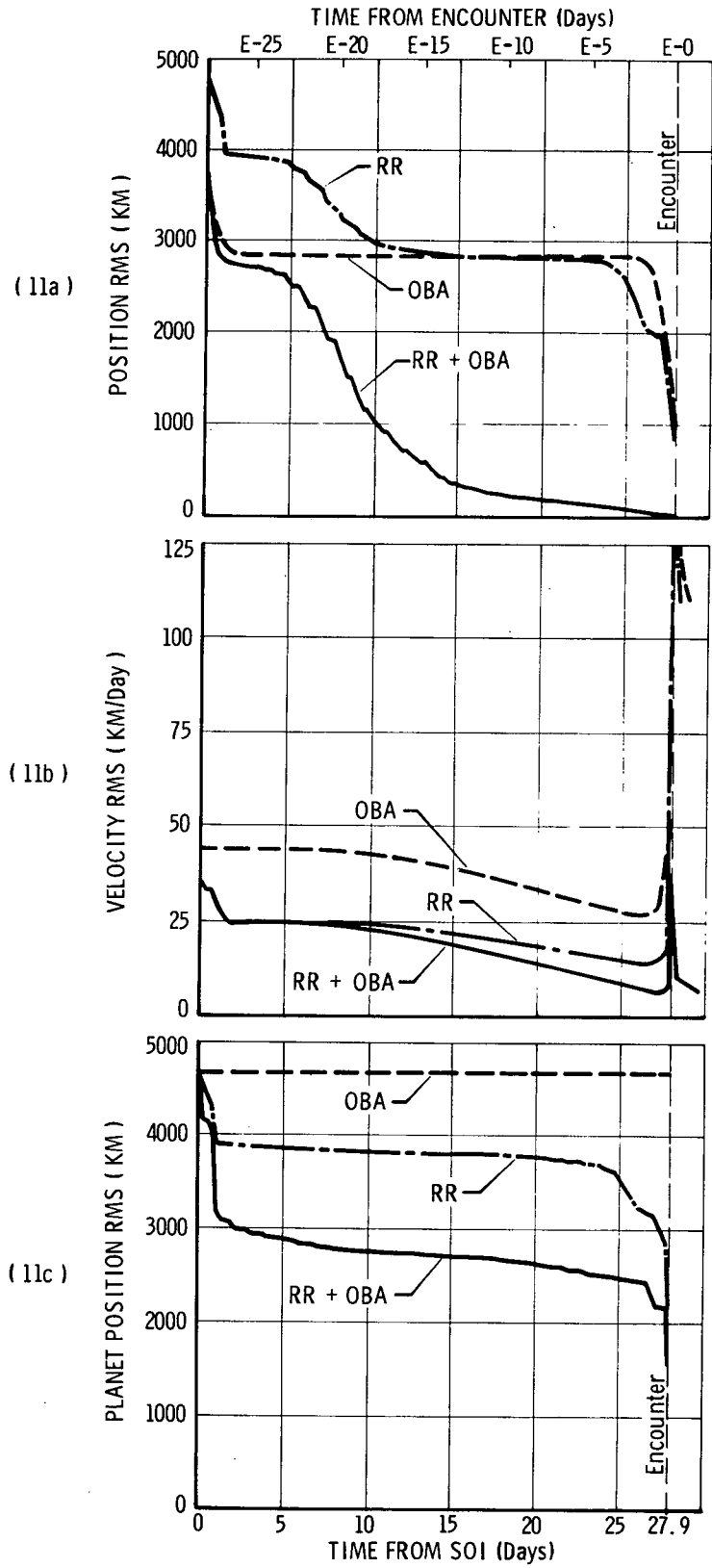


Figure 11 State Estimate Uncertainty During Uranus Approach

linearized problem considered here, is an ellipse centered at the estimated values of B·R and B·T (see Appendix E). The reference ellipses presented in this chapter are based on one-sigma values for B·R and B·T. Correspondingly, there is a 40 percent probability that the actual (true) values of the targeting parameters lie within the error ellipse. Error ellipses corresponding to any probability value P_r can be derived from the reference ellipse by multiplying the ordinate and abscissa by the factor $[2 \ln(P_r^{-1})]$. For 86 and 99 percent ellipses this quantity has the values of 2 and 3 respectively.

Jupiter Target Error Ellipses

Reference navigation accuracy data for Jupiter approach target parameters B·R and B·T are shown in Figures 12 and 13. In Fig. 12 the standard target error ellipses are compared at E-30, E-15, and E-5 days. These times were selected as representative of the period during which an approach guidance maneuver will be considered. Fig. 13 demonstrates the relative navigation accuracy of various combinations of the observation types. The error ellipses in these figures represent the dispersion of the true target points (B·R and B·T) relative to the estimated target point. (Recall that the target point is the point where the approach asymptote pierces the target plane. See Figure 39 for a definition of error ellipse nomenclature.)

Target error ellipses for range-rate, RR, observations only are shown in Figure 12a. These data indicate a slight decrease (100-200km) in both coordinates from E-30 to E-15 days. During the next ten days of tracking the B·T coordinate decreases an order of magnitude while the B·R coordinate remains virtually unchanged. Since both the spacecraft approach asymptote and the orbit plane (and thus \bar{T}) lie very close to the ecliptic plane at Jupiter, most of the range-rate information goes into the estimate

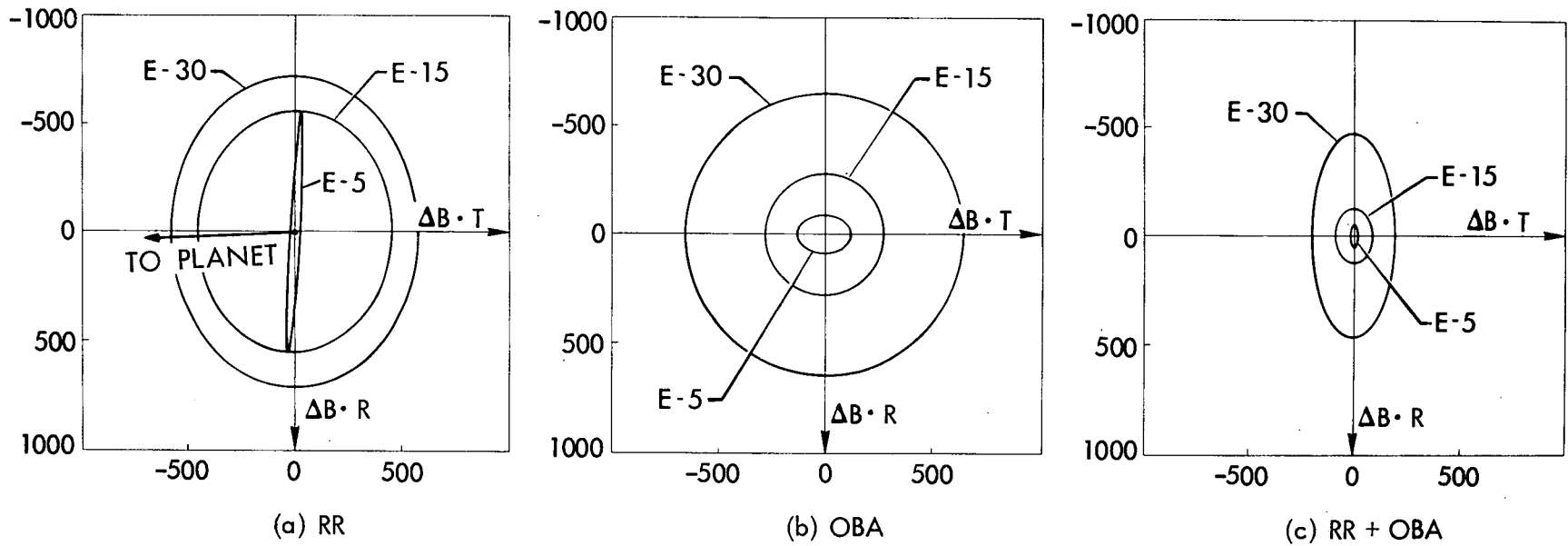


Figure 12 Navigation Target Error Ellipses for Jupiter Approach (RR, OBA, RR + OBA)

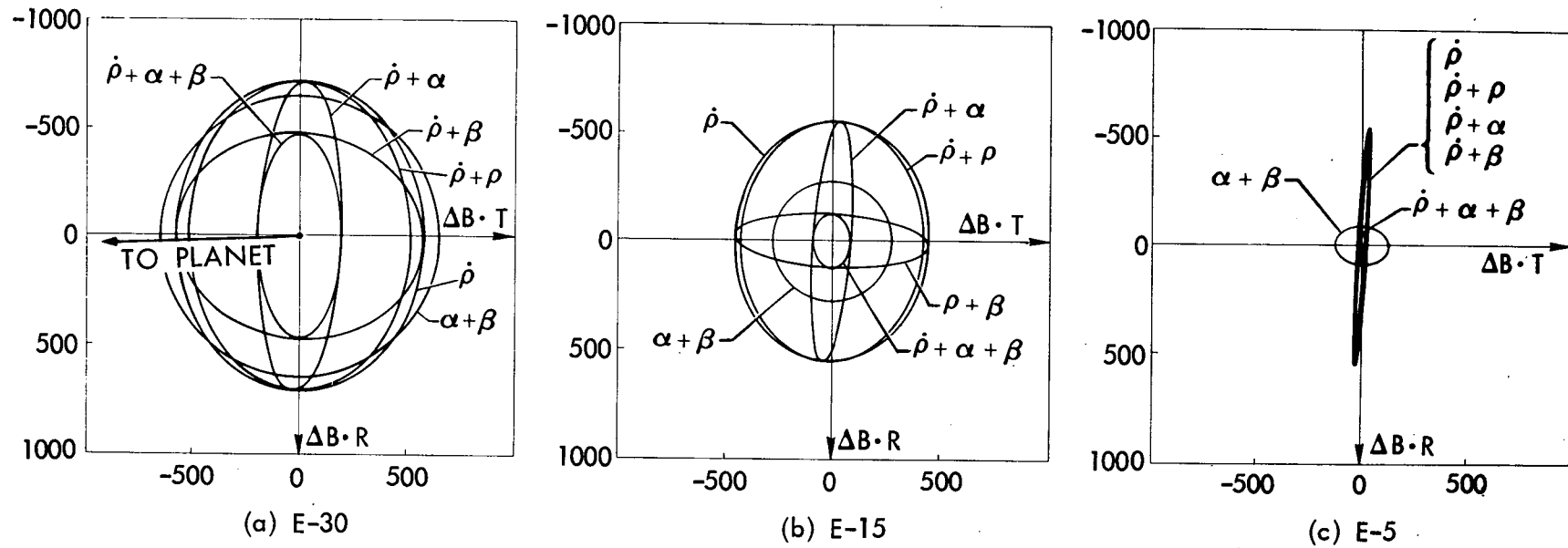


Figure 13 Navigation Target Error Ellipses for Jupiter Approach (E-30, E-15, E-5)

of the B·T component. B·R is essentially an out-of-plane component and is therefore more difficult to estimate with range-rate data alone.

In Fig. 12b the orbit determination ellipse for the onboard angles alone (sun-planet angle, α , and star-planet angle, β) are presented at E-30, E-15, and E-5 days. Note that onboard angle data give about a 370 km reduction in both B·R and B·T coordinates from E-30 to E-15. From E-15 to E-5 the B·T (in-plane) information is slightly better than the B·R (out-of-plane) information.

In Fig. 12c error ellipses for range-rate and onboard angle data show a rapid reduction in both B·R and B·T components when the data types are combined. Navigation accuracy is still better in the B·T direction than in the B·R direction due to high quality range-rate information in the in-plane direction.

Target error ellipses for various combinations of observation types are compared in Fig. 13. In addition to the data previously presented in Fig. 12 the data in Fig. 13 include error ellipses for range-rate plus sun-planet angle and range-rate plus star-planet angle. The sun-planet angle, α , being basically an in-plane angle, does not reduce the B·R component significantly over the range-rate only case. However, it does provide better in-plane information than range-rate alone as evidenced by the reduction in B·T at E-30 and E-15. At E-5 the difference between the range-rate plus sun-planet angle case and the range-rate case is negligible.

Saturn Target Error Ellipses

Reference navigation accuracy data for Saturn approach target parameters B·R and B·T are shown in Figures 14 and 15. In Fig. 14 the standard target error ellipses are compared at E-20, E-10 and E-2 days. The

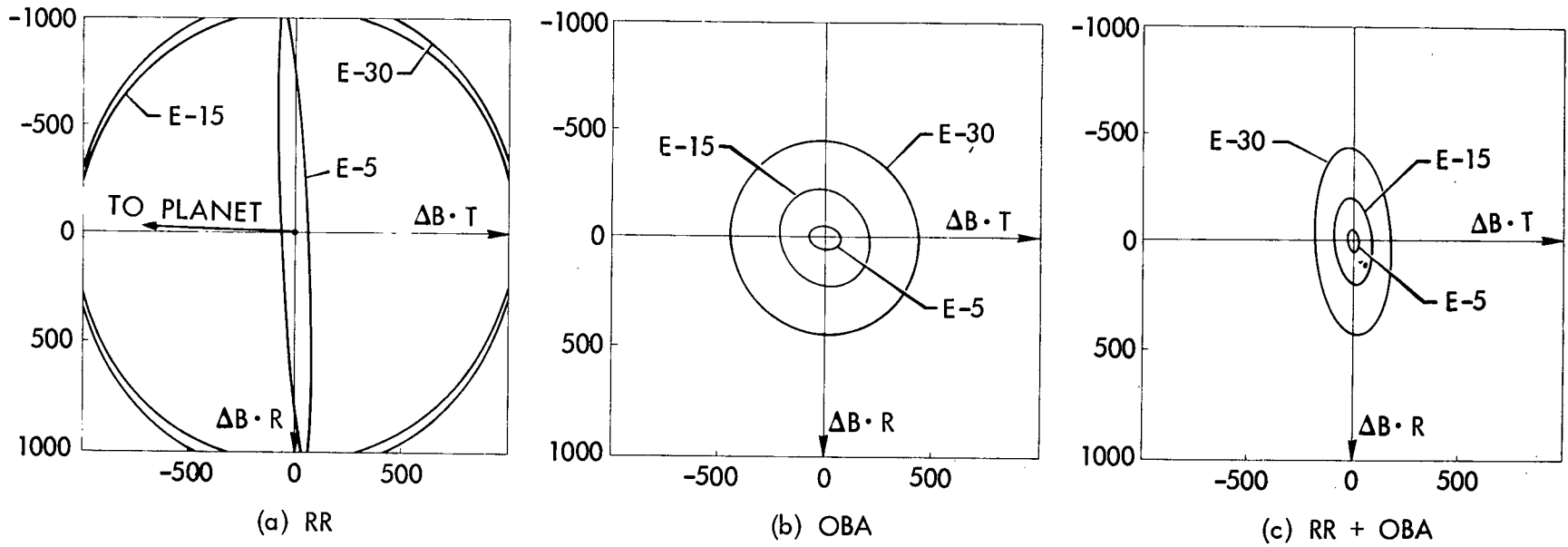


Figure 14 Navigation Target Error Ellipses at Saturn Approach (RR, OBA, RR + OBA)

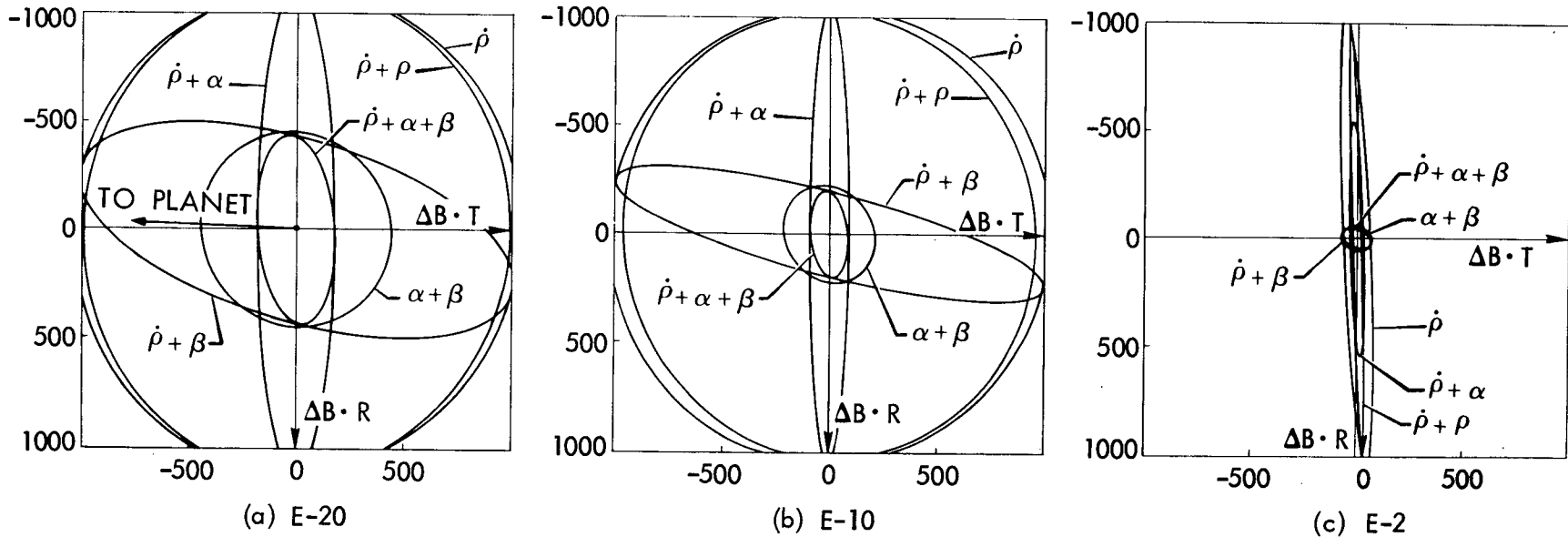


Figure 15 Navigation Target Error Ellipses at Saturn Approach (E-20, E-10, E-2)

relative accuracy of various observation combinations are presented in Fig. 15.

Target error ellipses for range-rate observations are shown in Fig. 14a. From that figure, it can be seen that virtually no target information is obtained from range-rate observations from E-20 to E-10 days. During the next 8 days of tracking a significant reduction in B·T is achieved with no significant decrease in B·R uncertainty. In contrast to the range-rate data, onboard angle data provide good target information throughout Saturn approach as can be seen from Fig. 14b. The error ellipses at E-20 and E-10 are nearly circular indicating that the onboard angles provide information of almost equal value in both the in-plane and out-of-plane directions. Range-rate plus onboard angle data provide about the same B·R accuracy as the onboard angle only case, but much improved B·T accuracy.

In Figure 15 the relative accuracy of the various data combinations is compared at E-20, E-10, and E-2 days. From Fig. 15 it can be seen that the star-planet angle, β , when combined with range-rate, $\dot{\rho}$, does not reduce the B·R component at Saturn significantly up through E-10 days. At E-2 days, however, the combination $\dot{\rho} + \beta$ gives a target accuracy comparable to the $\dot{\rho} + \alpha + \beta$ case and better than the $\alpha + \beta$ case. As was true at Jupiter approach, range-rate data alone provides a poor estimate for B·R.

Uranus Target Error Ellipses

Reference navigation accuracy data for Uranus approach target parameters B·R and B·T are presented in Figures 16 and 17. In Fig. 16 the standard target error ellipses are compared at E-20, E-10, and E-1 days. The relative accuracy of various observation combinations are presented in Fig. 17.

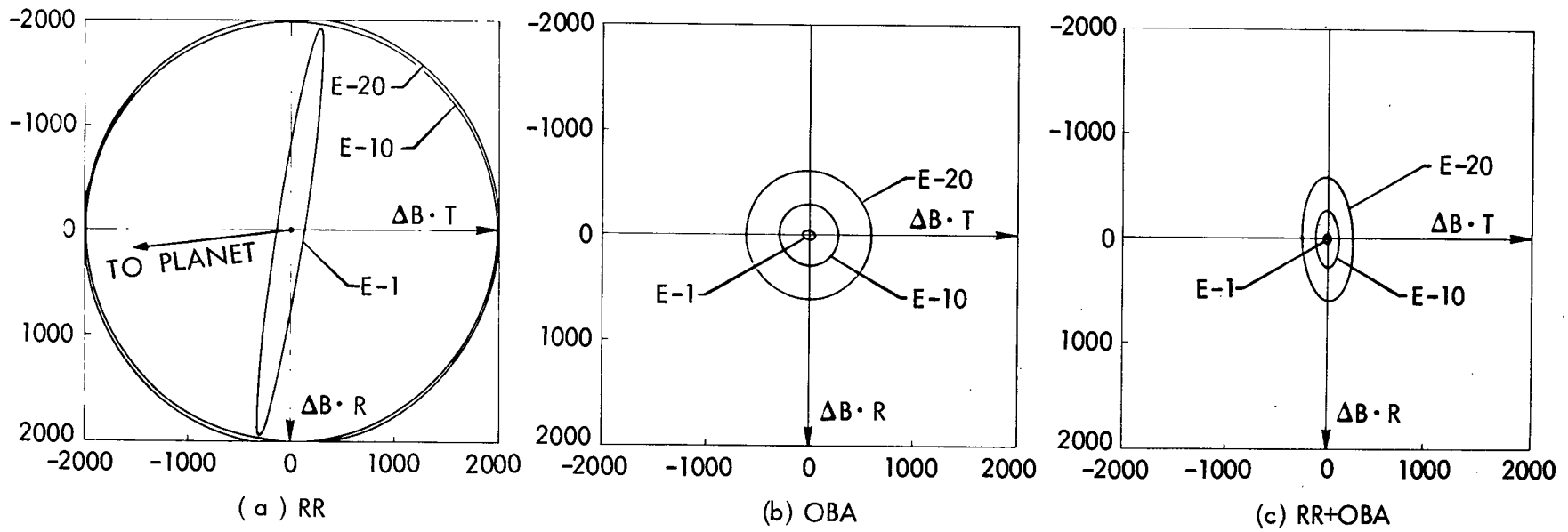


Figure 16 Navigation Target Error Ellipses at Uranus Approach (RR, OBA, RR + OBA)

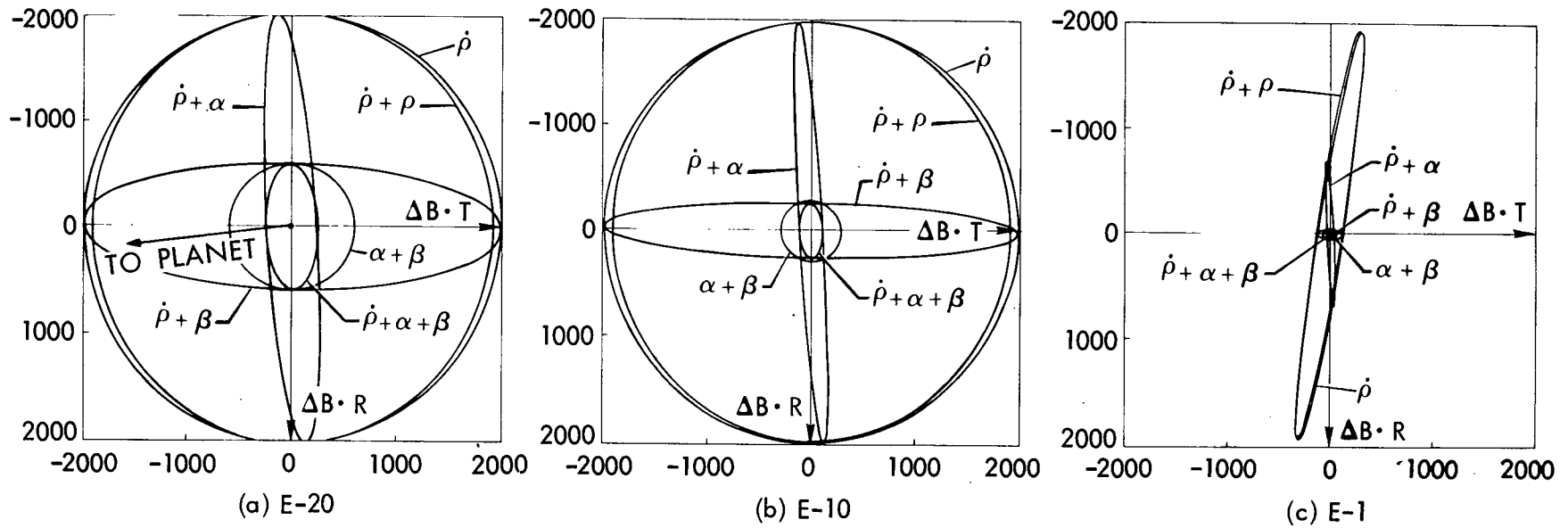


Figure 17 Navigation Target Error Ellipses at Uranus Approach (E-20, E-10, E-1)

Target error data for range-rate observations are shown in Fig. 16a. Range-rate data provides practically no target information from E-20 to E-10 days. The error ellipses at E-20 and E-10 are very nearly circular with a radius of about 2000 km. From E-10 to E-1 the B·T uncertainty is reduced to below 150 km with essentially no decrease in B·R uncertainty. Onboard angle data, however, give a uniform decrease in both B·R and B·T as shown in Fig. 16b. Combining range-rate data with onboard angle data results in a smaller B·T uncertainty than with onboard angle data only (Fig. 16c).

In Fig. 17 the relative accuracies of various data combinations are compared at E-20, E-10, and E-1 days. Significantly, the range-rate data are ineffective in reducing target errors until well into the approach phase. Adding the star-planet angle to the range-rate measurement (i.e., $\dot{\rho} + \beta$) decreases B·R uncertainty significantly while leaving B·T uncertainty virtually unchanged. Similarly, adding the sun-planet angle to the range-rate measurement (i.e., $\dot{\rho} + \alpha$) results in a large decrease in B·T uncertainty while leaving B·R uncertainty virtually unchanged. A combination of all three observations, $\dot{\rho} + \alpha + \beta$, yields good target accuracy in both the B·R and B·T components.

Tables 3, 4 and 5 summarize in tabular form the navigation data presented in the previous sections.

Overall State Uncertainty

Overall state uncertainties, as measured by the entropy of the estimation process, are presented in Fig. 18 for Jupiter, Saturn and Uranus approach. These data reflect the fact that although onboard angle measurements alone contain limited overall state information, they do provide valuable complimentary information when combined with range-rate data, thus making possible significantly improved navigation accuracy.

Table 3 Comparison of Navigation Accuracies at Jupiter Approach

TIME	E-30			E-15			E-5		
OBSERVATION	RR	OBA	RR + OBA	RR	OBA	RR + OBA	RR	OBA	RR + OBA
STATE UNCERTAINTY:									
Position RMS (km)	834	820	335	699	891	127	519	988	50
Velocity RMS (km/day)	12	29	12	4	23	3	5	30	2
Planet Position RMS (km)	1008	1299	774	773	1298	342	562	1298	192
Entropy	52	84	49	37	80	32	23	77	20
TARGET ERROR ELLIPSE:									
a (km)	719	652	475	559	284	125	554	129	55
b (km)	579	647	191	454	278	88	21	91	19
ψ (deg)	91	42	90	87	52	92	87	177	90
TARGET ERROR VARIANCES:									
$\sigma_{B \cdot R}^2$ (km ²)	5.2(+5)	4.2(+5)	2.3(+5)	3.1(+5)	7.9(+4)	1.6(+4)	3.1(+5)	8.3(+3)	3.0(+3)
$\sigma_{B \cdot T}^2$ (km ²)	3.4(+5)	4.2(+5)	3.6(+4)	2.1(+5)	7.8(+4)	7.8(+3)	4.4(+2)	1.7(+4)	3.7(+2)
$\sigma_{t_e}^2$ (days ²)	1.2(-7)	6.7(-7)	2.8(-8)	7.3(-7)	6.0(-6)	1.6(-8)	6.9(-9)	1.1(-6)	9.2(-11)

Table 4 Comparison of Navigation Accuracies at Saturn Approach

TIME	E-20			E-10			E-2		
OBSERVATION	RR	OBA	RR + OBA	RR	OBA	RR + OBA	RR	OBA	RR + OBA
STATE UNCERTAINTY:									
Position RMS (km)	1479	1450	315	1459	1466	147	1009	1440	51
Velocity RMS (km/day)	17	29	16	13	25	11	13	36	6
Planet Position RMS (km)	1957	2425	1470	1810	2423	1206	1209	2422	389
Entropy	60	88	55	51	85	44	37	80	35
TARGET ERROR ELLIPSE:									
a (km)	1111	460	441	1053	239	202	1033	72	51
b (km)	1040	437	179	1027	208	90	62	54	28
ψ (deg)	83	127	94	76	127	96	93	168	96
TARGET ERROR VARIANCES:									
$\sigma_{B \cdot R}^2$ (km ²)	1.2(+6)	2.0(+5)	1.9(+5)	1.1(+6)	5.2(+4)	4.0(+4)	1.1(+6)	3.0(+3)	2.5(+3)
$\sigma_{B \cdot T}^2$ (km ²)	1.1(+6)	2.0(+5)	3.3(+4)	1.1(+6)	4.8(+4)	8.4(+3)	6.1(+3)	5.0(+3)	8.0(-2)
$\sigma_{t_e}^2$ (days ²)	3.0(-7)	3.6(-6)	7.2(-8)	3.1(-7)	1.4(-6)	3.1(-9)	3.4(+9)	2.5(-6)	3.0(-11)

Table 5 Comparison of Navigation Accuracies at Uranus Approach

TIME	E-20			E-10			E-1		
OBSERVATIONS	RR	OBA	RR + OBA	RR	OBA	RR + OBA	RR	OBA	RR + OBA
STATE UNCERTAINTIES:									
Position RMS (km)	3270	2790	1699	2805	2803	219	1954	2491	42
Velocity RMS (km/day)	24	42	23	19	34	15	15	34	7
Planet Position RMS (km)	3811	4676	2781	3774	4674	2680	3157	4672	2357
Entropy	55	79	49	47	76	38	32	69	22
TARGET ERROR ELLIPSE:									
a (km)	2034	613	595	1992	297	261	1957	58	36
b (km)	2002	603	241	1982	283	115	131	36	28
ψ (deg)	77	137	92	30	134	92	81	170	99
TARGET ERROR VARIANCES:									
$\sigma_{B \cdot R}^2$ (km ²)	4.1 (+6)	3.7 (+5)	3.5 (+5)	3.9 (+6)	8.4 (+4)	6.8 (+4)	3.7 (+6)	1.3 (+3)	1.3 (+3)
$\sigma_{B \cdot T}^2$ (km ²)	4.0 (+6)	3.7 (+5)	5.8 (+4)	4.0 (+6)	8.4 (+4)	1.3 (+4)	1.0 (+5)	3.3 (+3)	7.7 (+2)
$\sigma_{t_e}^2$ (days ²)	2.8 (-4)	1.1 (-4)	4.2 (-5)	9.3 (-6)	2.3 (-6)	1.4 (-7)	1.1 (-9)	1.6 (-6)	2.5 (-12)

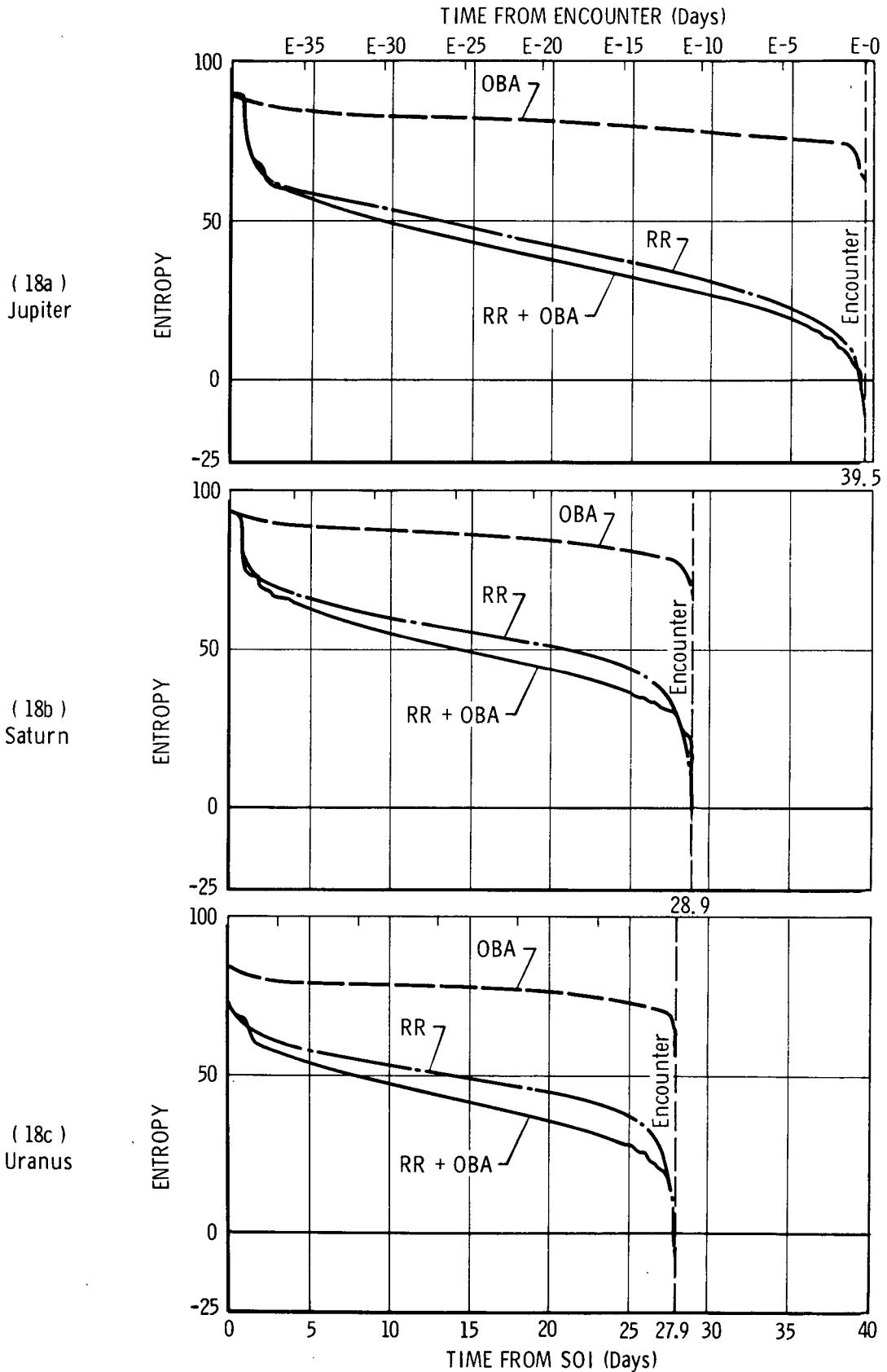


Figure 18 Time Histories of State Uncertainty (Jupiter, Saturn, Uranus)

Target Errors for Simulated Encounter

The two types of data presented previously are based on assumed statistical models for the error sources and represent predicted navigation error statistics for state and targeting components. The actual navigation errors for any single mission will depend upon observation errors which actually occur during the course of that single mission. Although the actual navigation errors are never known apriori, simulation of the orbit determination process using assumed error sources provides a means of studying the estimation process and evaluating the validity of the predicted error statistics. Example time histories of actual target errors for simulated encounters with Jupiter, Saturn and Uranus are shown in Figs. 19 through 27. For these simulations both the initial state error and the initial state estimate are, zero, i.e., $\hat{x}_0 = x_0 = 0$. The target error is defined as the true (simulated) value minus the estimated value of the components of the target vector.

Time histories of the target vector at Jupiter for the simulated mission are presented in Figs. 19, 20 and 21 for RR, OBA and RR + OBA cases, respectively. For all three cases the estimation process converged in a manner consistent with the predicted navigation accuracies listed in Table 3. For the RR case the characteristic velocity uncertainty growth, Fig. 9b, is reflected in an increased B·R error just prior to encounter, Fig. 19a. The velocity uncertainty for the OBA case, Fig. 10b, is reflected in increased t_e error near encounter, Fig. 20c. A combination of RR and OBA, Fig. 19c, provides a significant improvement in estimation accuracy over the RR and OBA cases.

Figs, 22, 23 and 24 consist of time histories of the target errors at Saturn for the RR, OBA and RR + OBA cases respectively. For all three

cases the error histories are consistent with the predicted navigation accuracies listed in Table 4. The RR data, Fig. 22, exhibit a B·R error growth just prior to encounter which coincides with the increase in velocity error covariance shown in Fig. 10. For the OBA case the velocity uncertainty is reflected in the error in time of encounter, t_e , Fig. 23c. Combining RR and OBA, Fig. 24, results in a significant improvement in all three components of the target vector.

Time histories of target errors at Uranus are presented in Figs. 25, 26 and 27 for the RR, OBA and RR + OBA respectively. From Fig. 25a it can be seen that the errors in B·R and B·T are not reduced significantly until encounter, a result which is consistent with predicted navigation accuracies listed in Table 5. The time-of-encounter estimate is very good after about E-10 days. The OBA data, Fig. 26, provide a better estimate for B·R and B·T but give a poor estimate for t_e just prior to encounter. This result is consistent with the predicted navigation accuracies presented in Table 5. A combination of RR and OBA data, Fig. 27, give a significant improvement over both RR and OBA data.

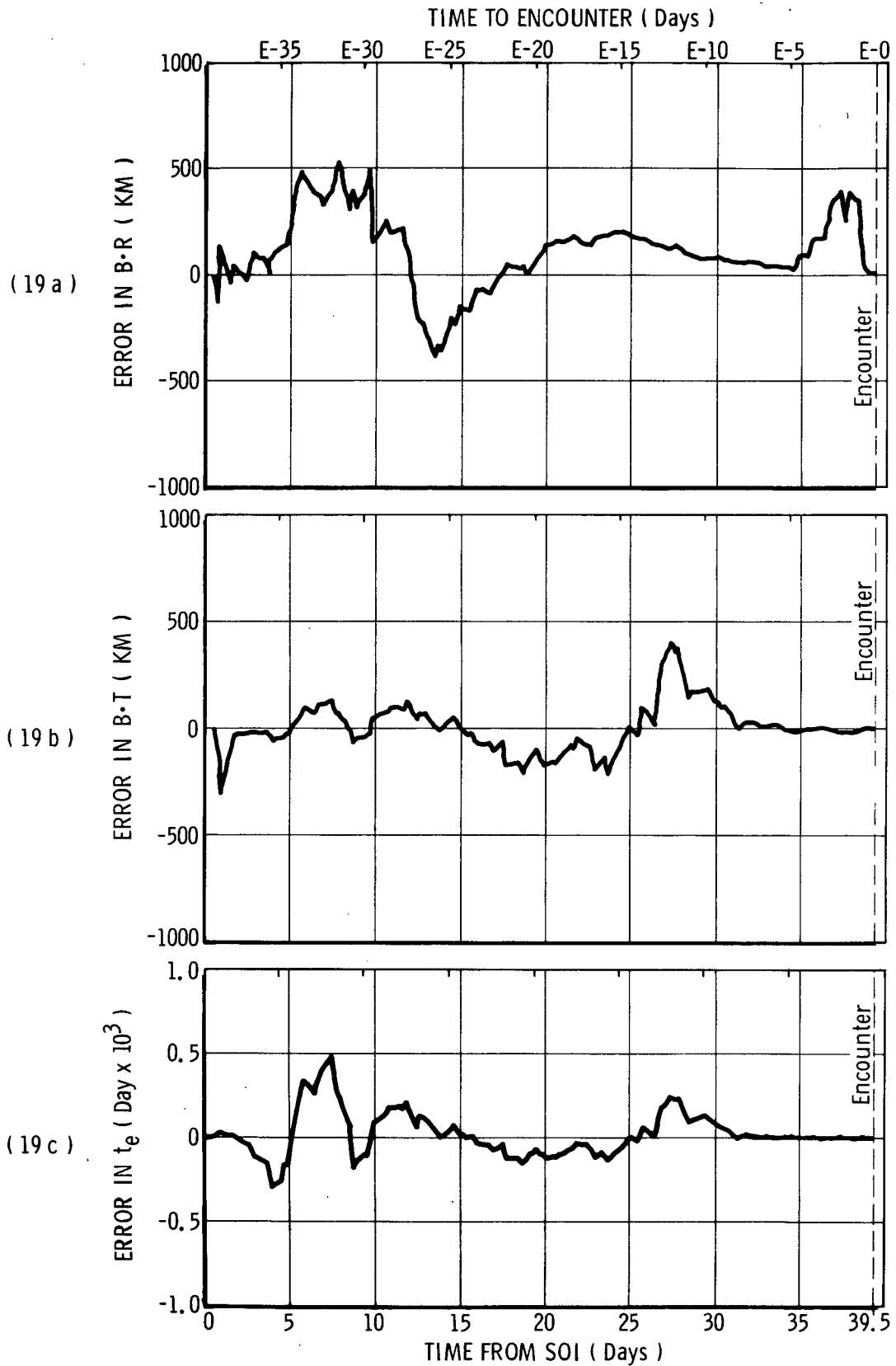


Figure 19 Time Histories of Target Errors at Jupiter Approach (RR)

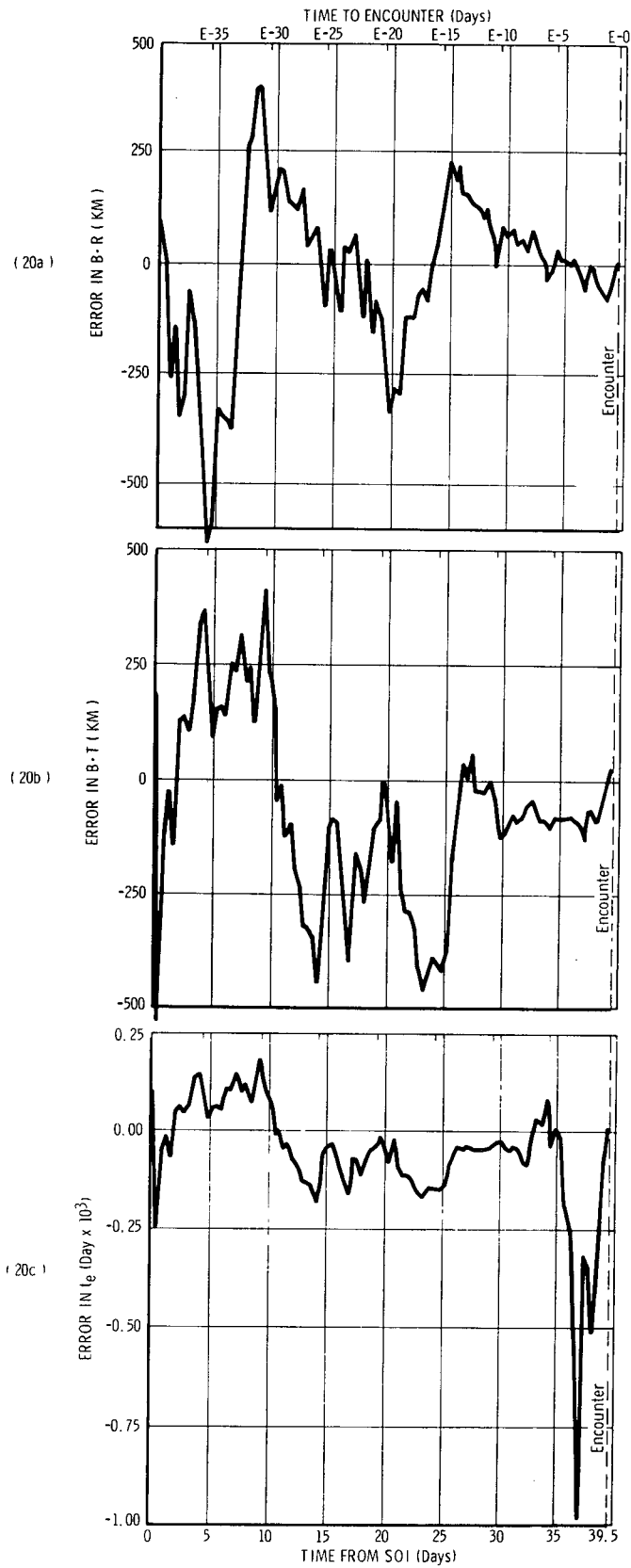


Figure 20 Time Histories of Target Errors at Jupiter Approach (OBA)

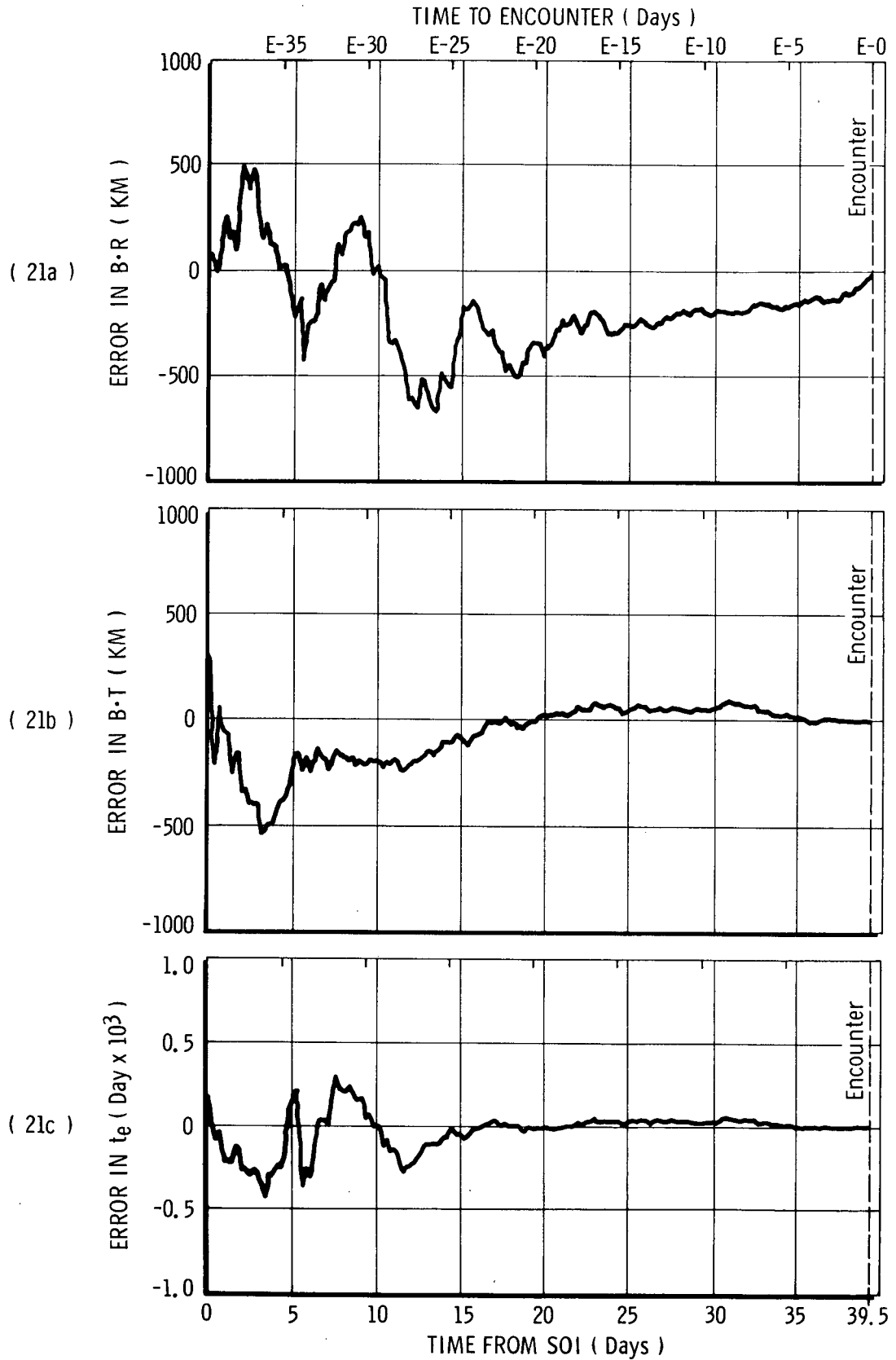


Figure 21 Time Histories of Target Errors at Jupiter Approach (RR + OBA)

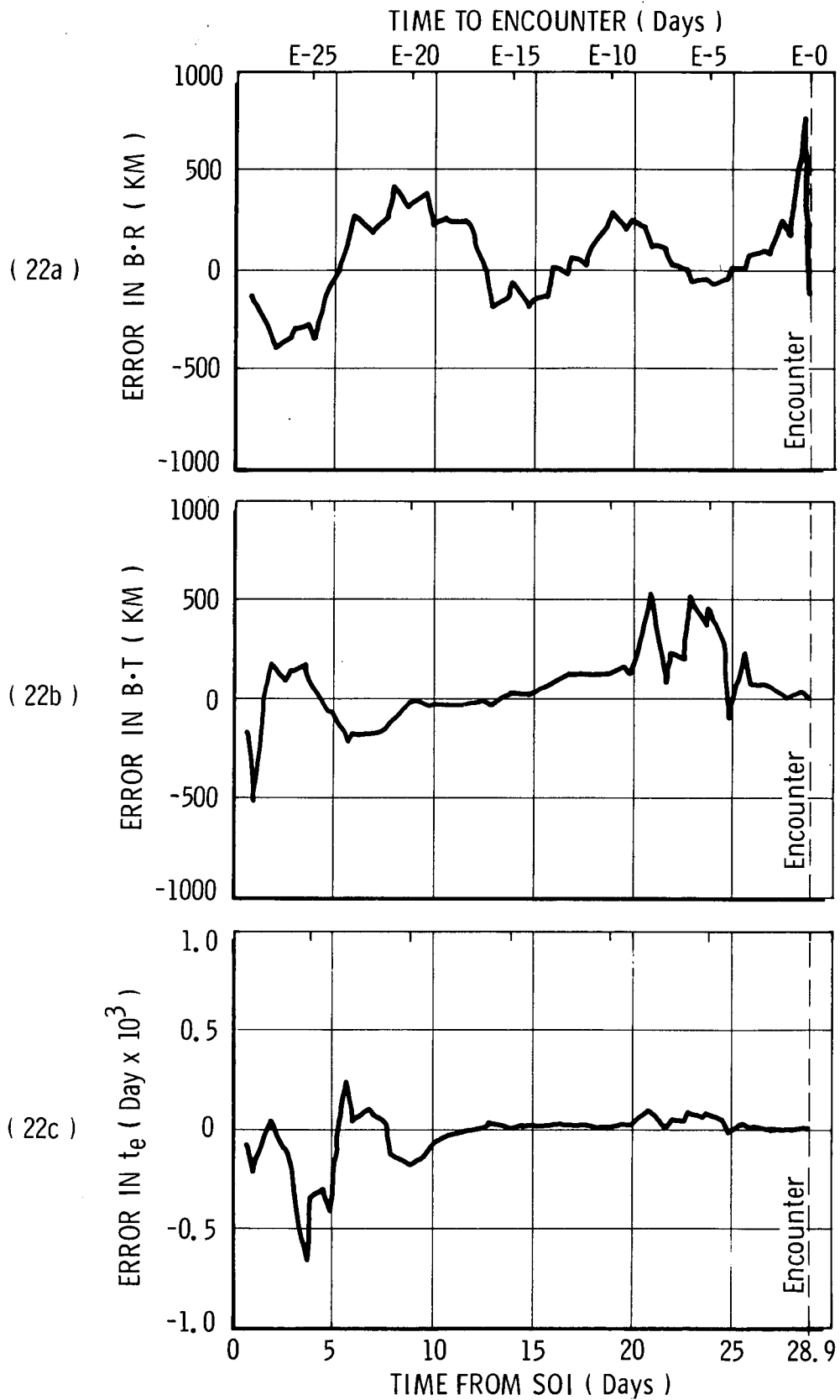


Figure 22 Time Histories of Target Errors at Saturn Approach (RR)

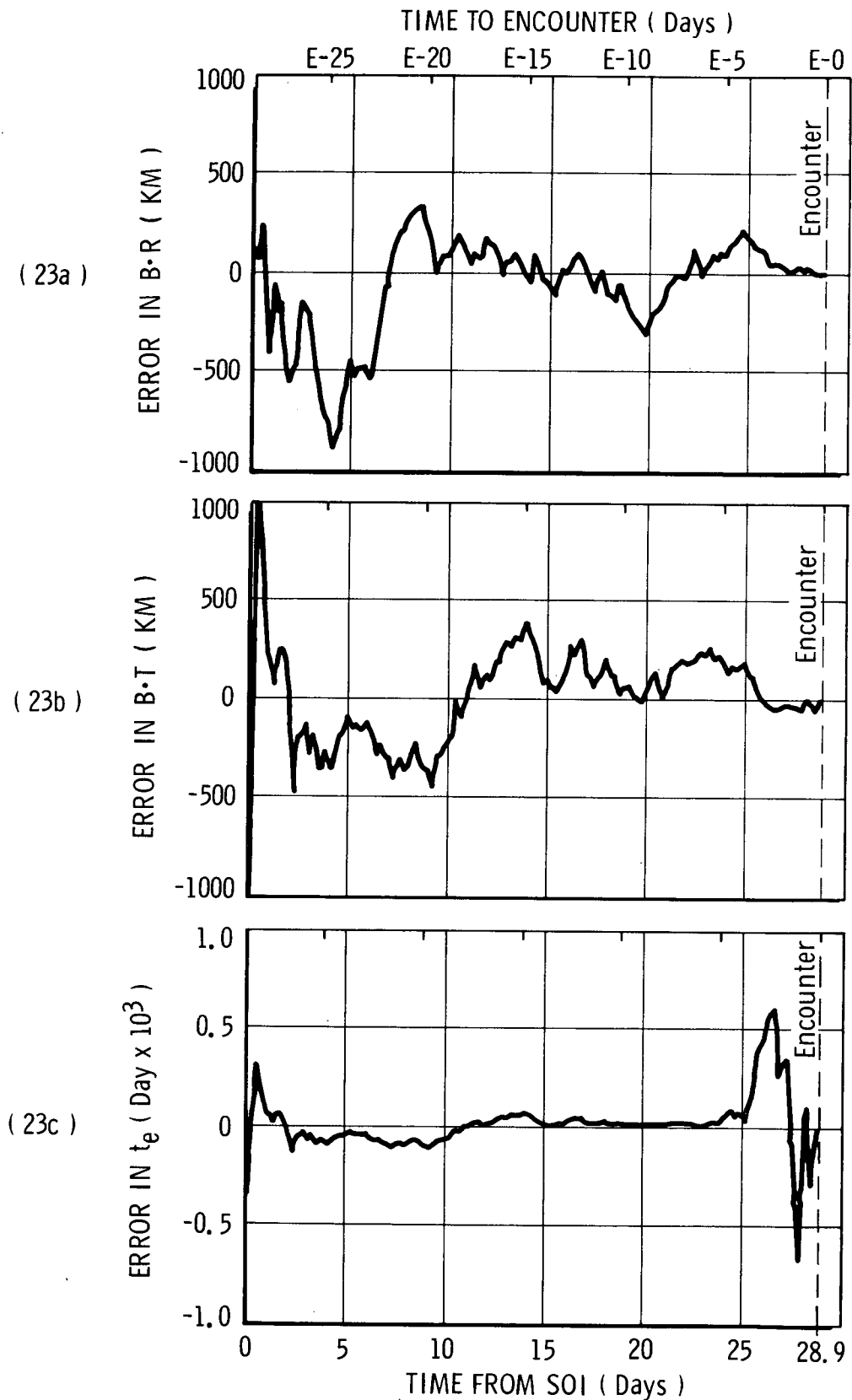


Figure 23 Time Histories of Target Errors at Saturn Approach (OBA)

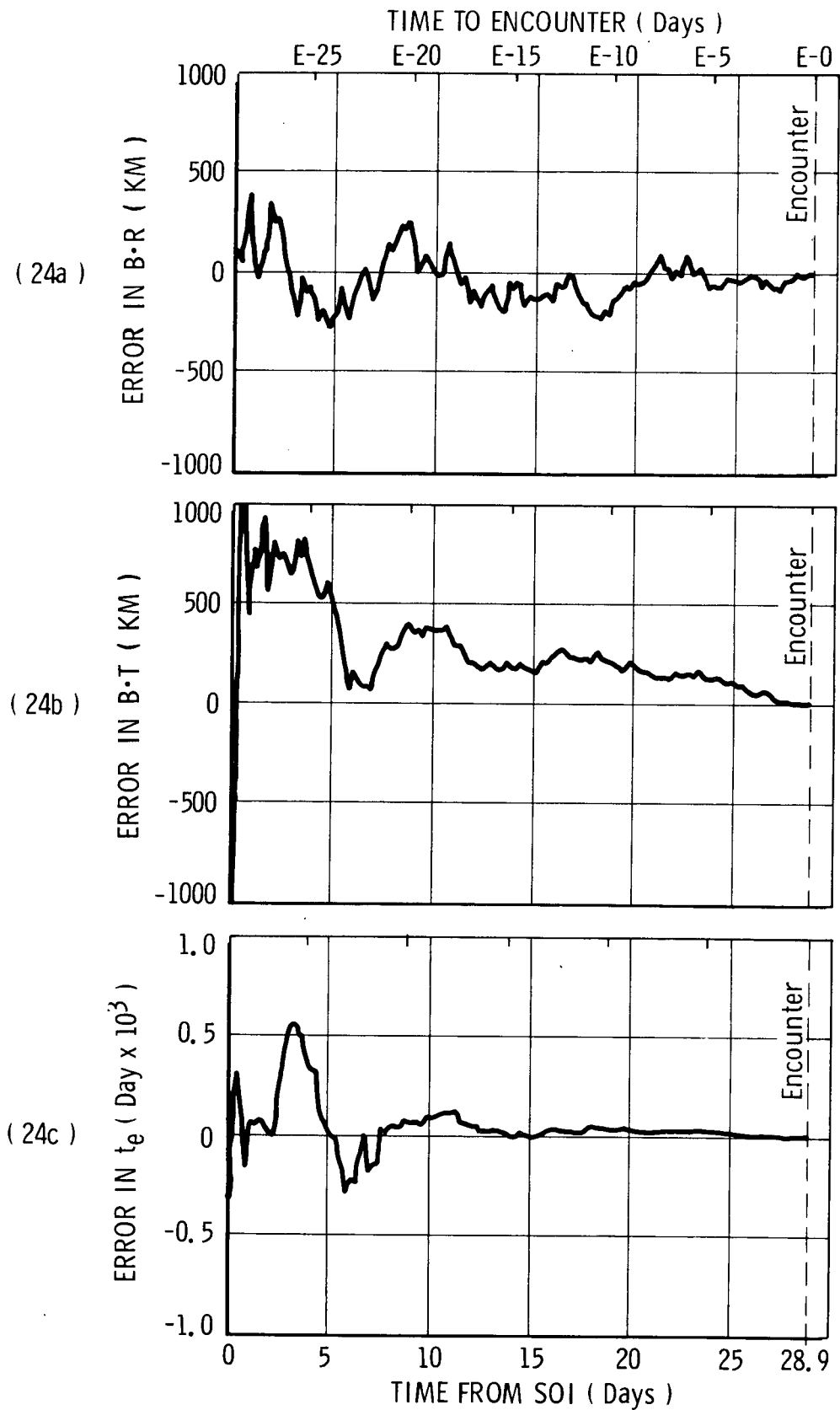


Figure 24 Time Histories of Target Errors at Saturn Approach, (RR + OBA)

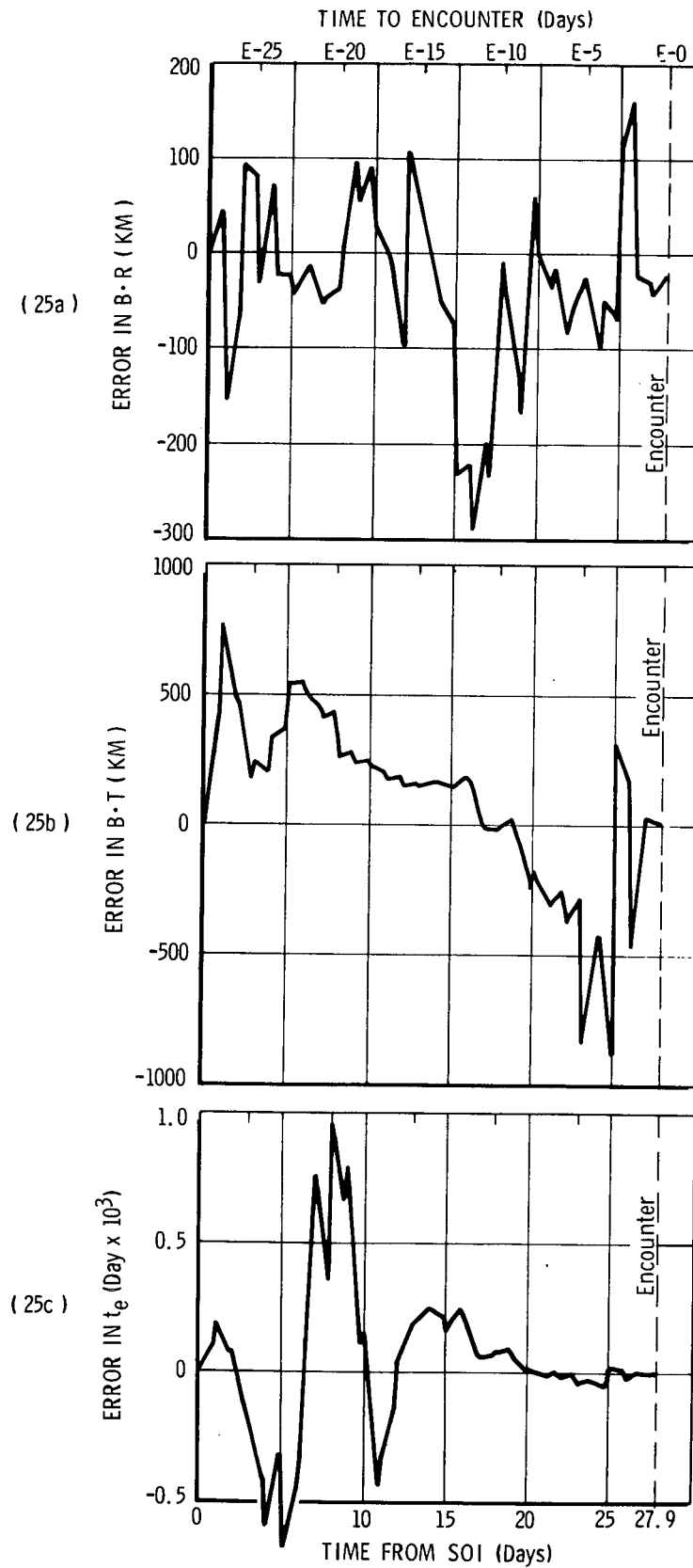


Figure 25 Time Histories of Target Errors at Uranus Approach (RR)

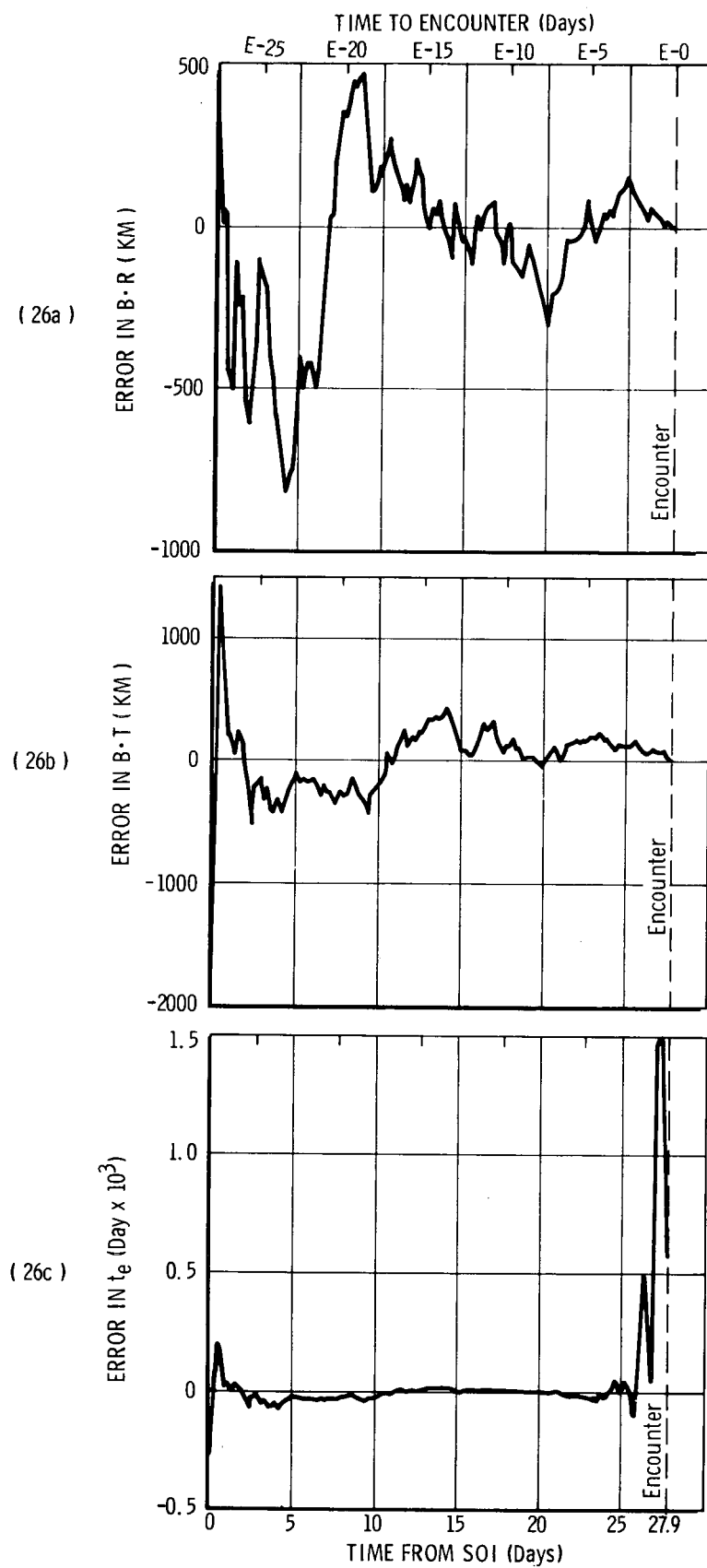


Figure 26 Time Histories of Target Errors at Uranus Approach (OBA)

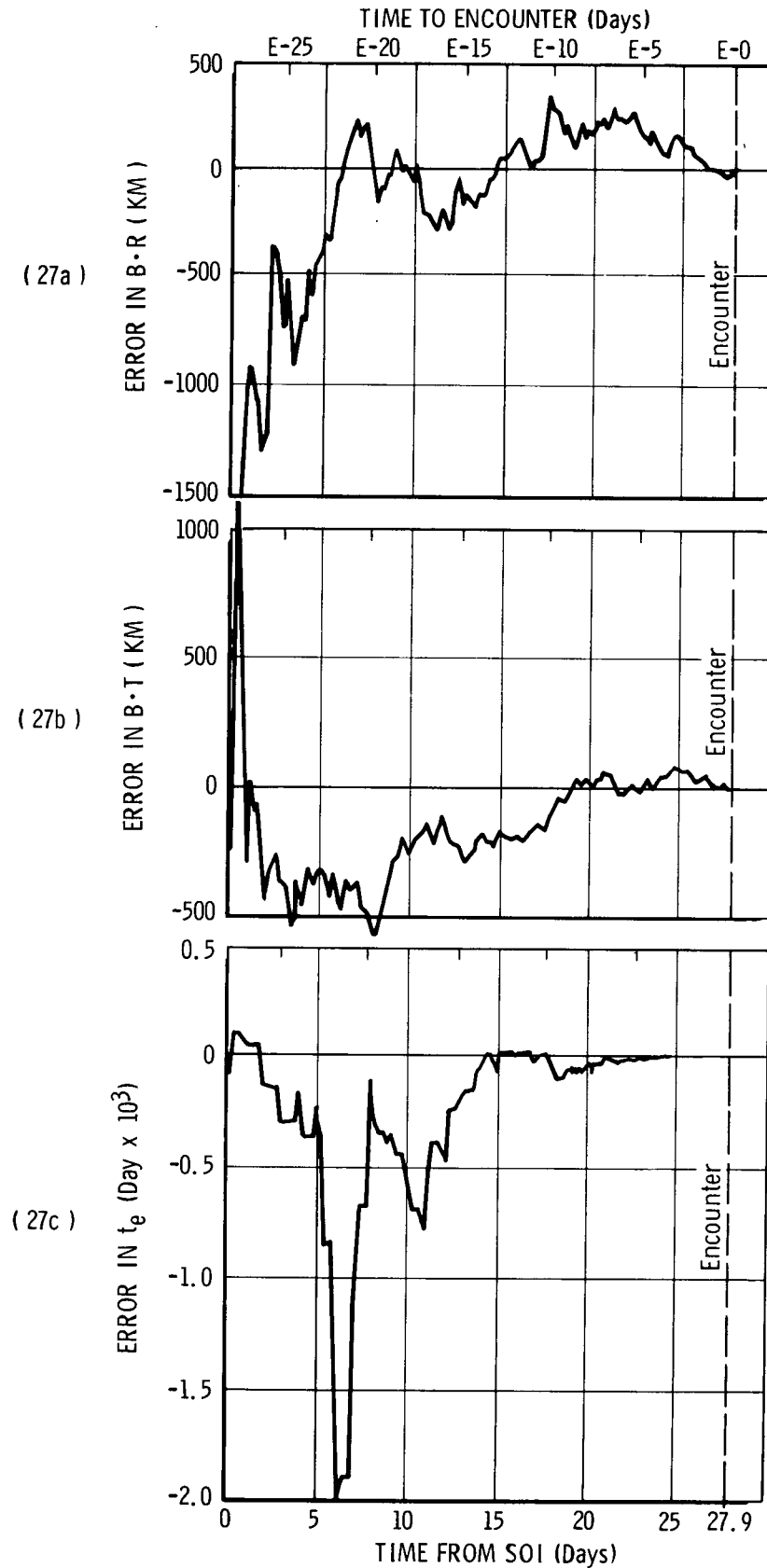


Figure 27 Time Histories of Target Errors at Uranus Approach (RR + OBA)

CHAPTER 5

APPROACH GUIDANCE ANALYSIS

Because of the extreme sensitivity of the Grand Tour mission to errors in the encounter trajectory at Jupiter, Saturn and Uranus, the success of the mission will depend to a large extent on the effectiveness of the approach guidance procedure. This chapter contains the results of an analysis of the approach guidance process for the 1977 Grand Tour Interior mission. The approach phase of the encounter at Jupiter, Saturn and Uranus was simulated to survey and define guidance requirements and target accuracies at those planets. A sensitivity analysis was conducted to determine the effects of observation accuracy, guidance execution accuracy, and initial state errors on the approach guidance requirements. Finally a Monte Carlo simulation of the approach navigation and guidance process at Saturn encounter was conducted for the purpose of testing the adequacy of the linear theory.

5.1 Assumed Execution Errors

In addition to the assumed error sources listed in Table 1, the analysis of this chapter considers errors in the execution of the guidance correction. (The execution error model is described in Chapter 2.) The uncertainty in the velocity correction is assumed to originate from two independent sources: (1) uncertainty in the magnitude of the correction due to a random error in the total impulse applied by the rocket engine, and (2) uncertainty in the orientation of the correction vector due to random errors

in the direction of the thrust vector. Nominal values of one-sigma guidance execution errors were assumed as follows:

Correction magnitude: $\kappa = 0.001$ (0.1 percent)
 Orientation Angle: $\gamma = 0.001$ degrees (3.6 arc sec).

The factor κ relates the execution error to the correction magnitude (error = $\kappa|\Delta V|$), and the angle γ is the angle between the commanded correction vector and the actual correction vector.

5.2 Preliminary Considerations

A graphical representation of various covariance matrices associated with the navigation and guidance process is presented in Figure 28. The initial state error covariance matrix, S_0 , and the initial state estimate error covariance matrix, P_0 , are assumed equal at the sphere of influence (SOI). As the orbit determination process proceeds, the estimate of the state improves and the P matrix decreases. The rate of decrease is dependent upon the frequency and the information content of the observations. The S matrix increases with time as the initial state uncertainty is propagated along the nominal trajectory. Since the initial state errors are assumed to be distributed about a zero mean, the probability ellipse representing S is centered on the nominal state, X^* . The probability ellipse representing P is centered at the current state estimate, \hat{X} . The probability ellipse describing the dispersion of the state deviation estimate, \hat{x} , defined by the covariance matrix S-P, is centered on X^* . When a guidance correction is executed, the velocity components of the P matrix are increased due to the uncertainty in the guidance execution (see Equation (2.96)). The S matrix decreases significantly at execution due to the input of navigation information. This decrease is

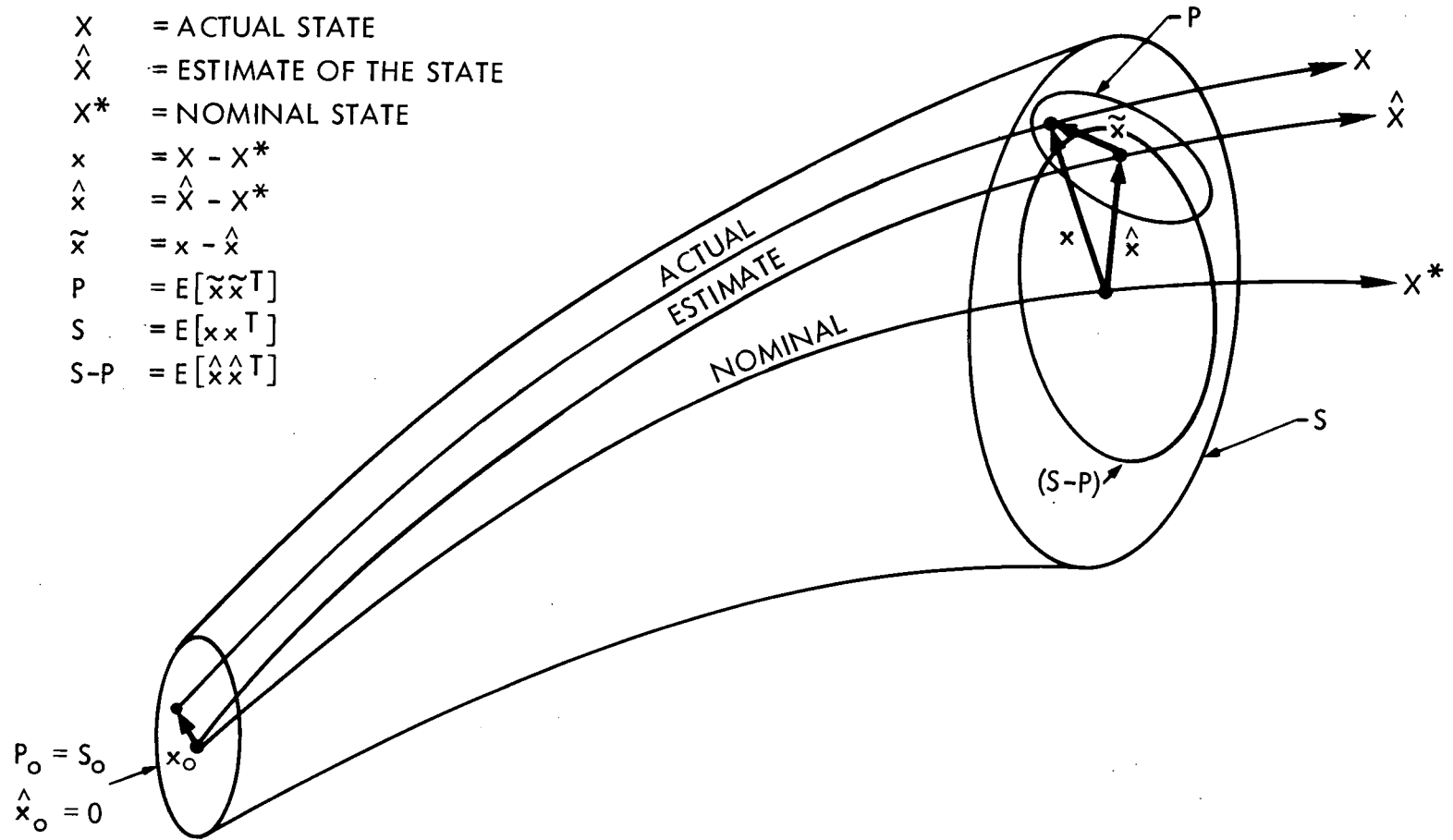


Figure 28 Geometric Representation of Navigation and Guidance Covariance Matrices

offset slightly by the added uncertainty resulting from guidance execution errors (see Equation (2.107)).

As derived in Chapter 2, ΔV_{rms} and δT_{rms} are given by

$$\Delta V_{\text{rms}} = \{\text{Trace} [B(S - P)B^T]\}^{\frac{1}{2}} \quad (5.1)$$

$$T_{\text{rms}} = \{\text{Trace} [M S^+ M^T]\}^{\frac{1}{2}} \quad (5.2)$$

where

$$M = [M_1^+ \mid M_2^-] = [\partial T / \partial \bar{r} \mid \partial T / \partial \bar{v}]$$

$$B = [-M_2^{-1} \mid M_1^+ \mid -I]$$

$$S = E[\mathbf{x}\mathbf{x}^T]$$

$$P = E[\bar{\mathbf{x}}\bar{\mathbf{x}}^T]$$

and where the subscripts $()^+$ and $()^-$ indicate values of the quantities before and after the correction. Since the first two components of the target vector T (i.e., $B \cdot R$ and $B \cdot T$) are of primary interest to this analysis, it is convenient to adopt the notation T' for the abbreviated target vector, i.e.,

$$T' = \begin{bmatrix} B \cdot R \\ B \cdot T \end{bmatrix}.$$

The state estimate error covariance matrix P and the state error covariance matrix S were assumed to be equal at the initial time (i.e., at entry into the target planet's SOI). Nominal values of the diagonal elements (variances) of the initial state error covariance matrix, P_0 , are listed in Table 2. Off-diagonal elements of P_0 were assumed to be zero.

The nominal heliocentric velocity \bar{v}_h^* of the spacecraft at the out-bound SOI is given by

$$\bar{v}_h^* = \bar{v}^* + \bar{v}_p^* \quad (5.3)$$

where \bar{V}^* is the nominal planetocentric velocity of the spacecraft and \bar{V}_p^* is the nominal heliocentric velocity of the planet. Neglecting the small error in the planet's heliocentric velocity and assuming that the departure correction required to account for small heliocentric position errors are negligible, the velocity correction required at departure is

$$\Delta V_3 = \bar{V} - \bar{V}^* \quad (5.4)$$

where \bar{V} is the actual planetocentric velocity of the spacecraft. At the SOI Eq. (5.4) can be closely approximated by

$$\Delta V_3 = \bar{V}_{\infty D} - \bar{V}_{\infty D}^* \quad (5.5)$$

where $\bar{V}_{\infty D}$ is the hyperbolic excess velocity. Furthermore, at the outbound SOI, the covariance matrix P becomes small relative to the covariance matrix S, thus

$$S(t_3) - P(t_3) \cong S(t_3). \quad (5.6)$$

The assumptions and approximations just described allow for the computation of the covariance matrix associated with the departure correction ΔV_3 without simulating the mission past the time of the second correction, i.e.,

$$\text{cov}[\Delta V_3] = C \{ \text{cov}[\delta T']_{t_2} \} C^T \quad (5.7)$$

where $C = \left[\frac{\partial \bar{V}_{\infty D}}{\partial T} \right]_{t_2}^*$ is the matrix of partial derivatives required to map from approach target space to departure target space (evaluated on the nominal path at time t_2). Analytical expressions for the matrix C are derived in Appendix G. The RMS value of the departure correction is defined by

$$\Delta V_{\text{rms}_3} = \{ \text{Trace} (\text{cov}[\Delta V_3]) \}^{1/2}. \quad (5.8)$$

5.3 Approach Guidance Requirements and Target Accuracies

Guidance execution times were surveyed to determine the variation of guidance requirements (ΔV_{rms}) and target accuracy ($\delta T'_{\text{rms}}$) during approach to Jupiter, Saturn and Uranus. Both a one and a two guidance correction strategy was considered for the range-rate (RR) and the range-rate plus onboard angle (RR + OBA) cases.

One Correction Survey

The variations of ΔV_{rms} and $\delta T'_{\text{rms}}$ with execution time are shown in Figures 29, 30 and 31 for one correction at approach to Jupiter, Saturn and Uranus respectively. Since the covariance matrices associated with errors in the state and the state estimate are assumed to be identically equal at the SOI (i.e., $P_o = S_o$), the ΔV_{rms} is zero initially (see Equation(5.1)). The ΔV_{rms} curves increase slowly at first and then increase asymptotically as periapsis is approached. The ΔV_{rms} curves for the two observation cases are very nearly the same with the RR curve falling slightly under the RR + OBA curve. The post-correction target accuracy, $\delta T'_{\text{rms}}$, decreases from SOI to encounter with the RR curve substantially above the RR + OBA curve for each planet.

Two Correction Survey

A survey of two approach guidance corrections was made to determine the effect of execution times on two selected indices of guidance performance. The navigation and guidance process was simulated for a matrix of five values of first correction time (t_1) and six values of second correction time (t_2). These data include the one-correction data previously presented since at the SOI the required velocity correction is zero. Representative contours of the two performance indices listed below were drawn in

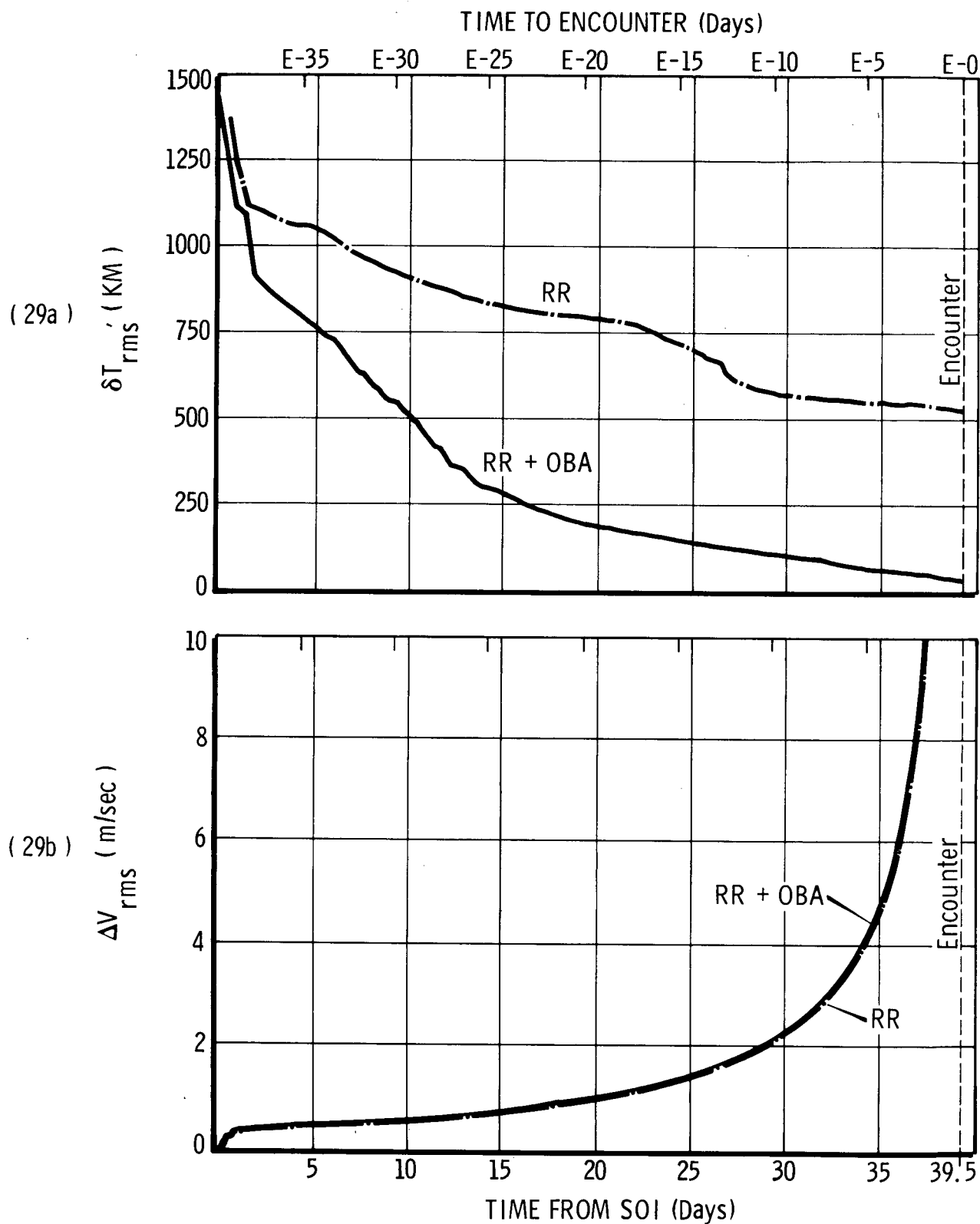


Figure 29 One Correction Guidance Survey at Jupiter Approach

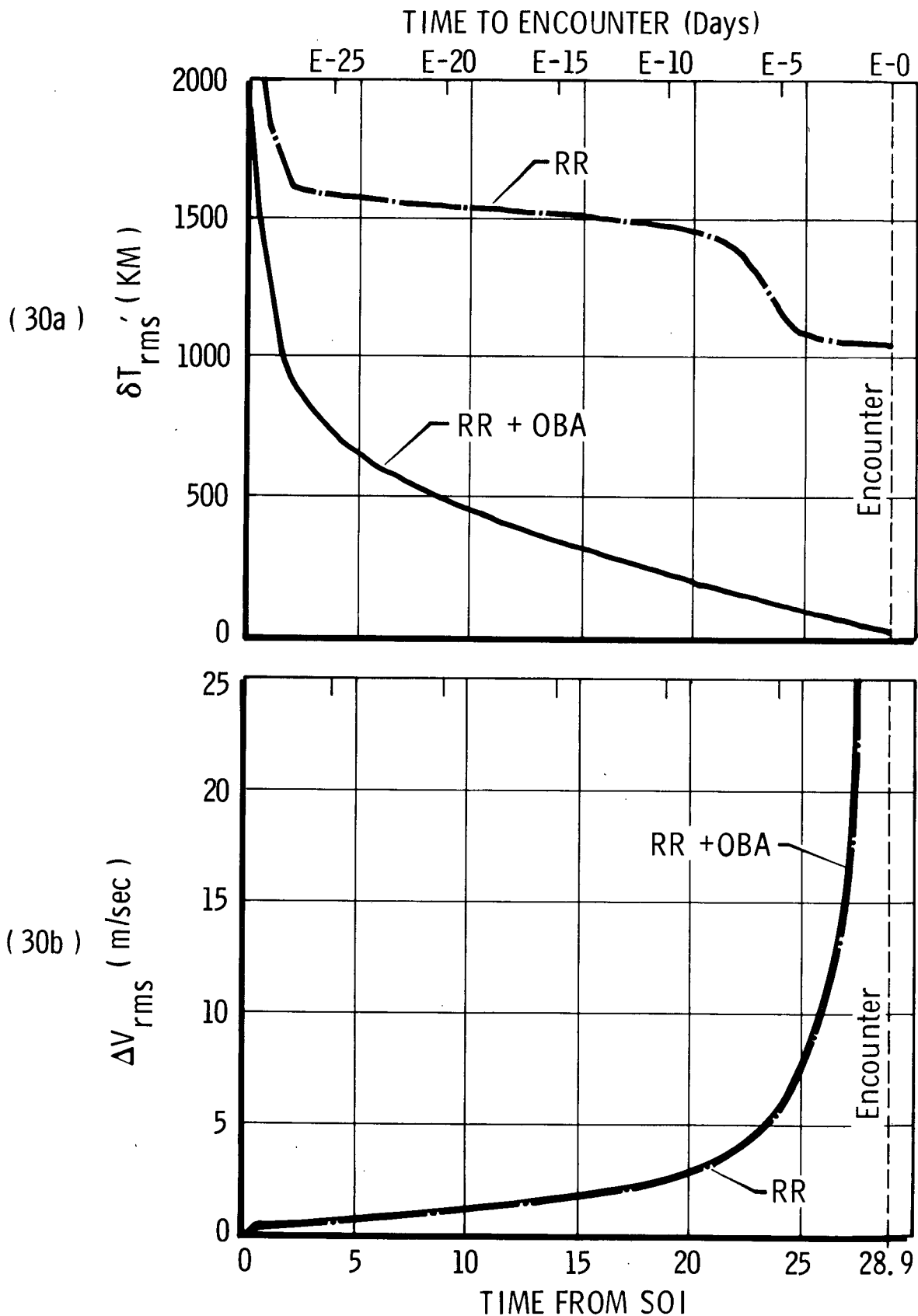


Figure 30 One Correction Guidance Survey at Saturn Approach

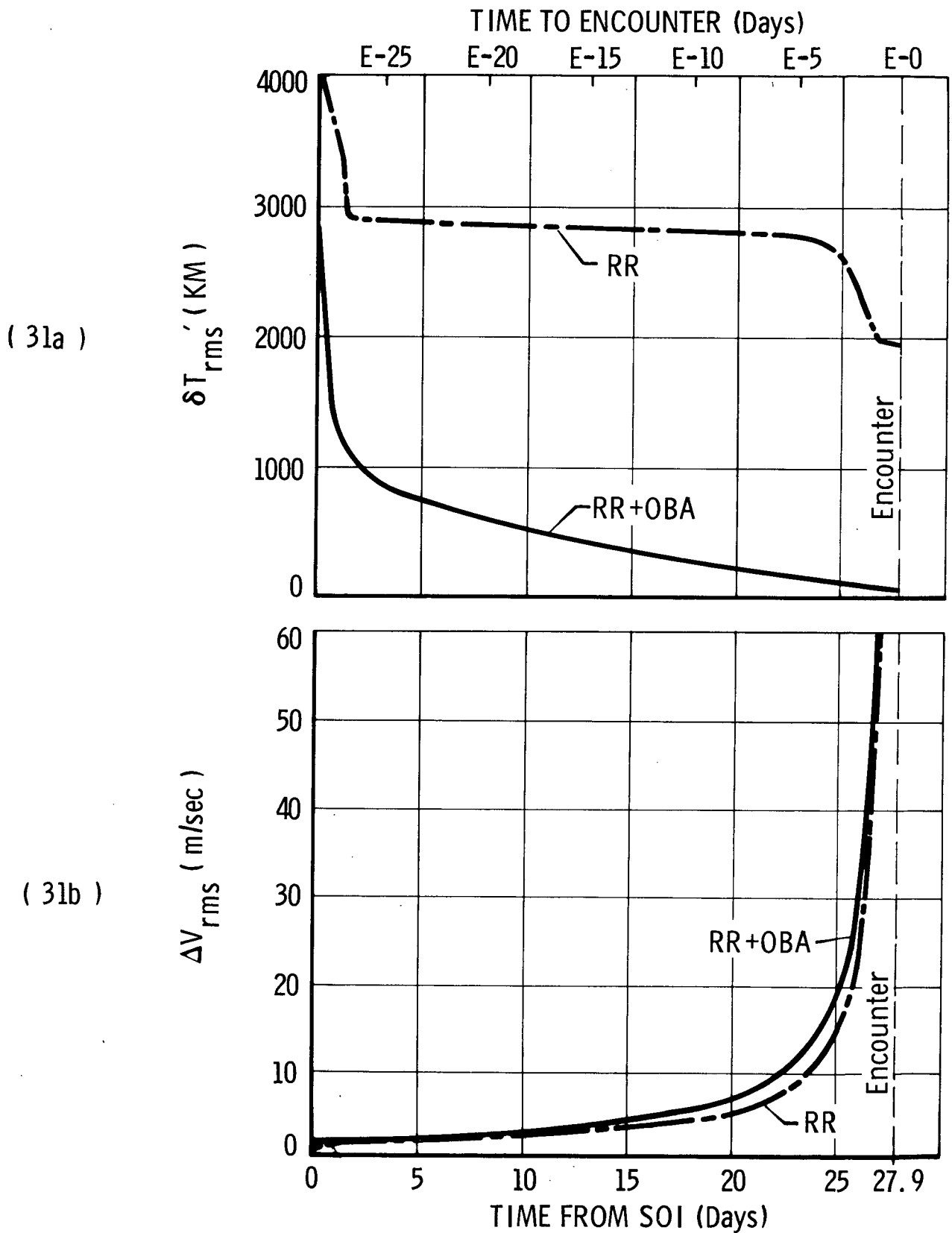


Figure 31 One Correction Guidance Survey at Uranus Approach

$t_1 - t_2$ space:

$$I_1 = \Delta V_{\text{rms}_1} + \Delta V_{\text{rms}_2}$$

$$I_2 = \Delta V_{\text{rms}_1} + \Delta V_{\text{rms}_2} + \Delta V_{\text{rms}_3}$$

ΔV_{rms_1} and ΔV_{rms_2} are the RMS values of the guidance corrections at t_1 and t_2 respectively. ΔV_{rms_3} is the correction required to null the velocity error at departure resulting from target errors remaining after the second correction. The departure correction requirement was defined by the correction required at outbound SOI to achieve the nominal hyperbolic excess velocity $\bar{V}_{\infty D}$.

Surveys of guidance performance index I_1 for the RR case and RR + OBA case are presented in Figures 32, 33 and 34 for Jupiter, Saturn and Uranus, respectively. These data exhibit a smooth gradient of increasing I_1 values as both the first and second guidance times increase. The index is much more sensitive to the second correction time than to the first correction time. The RR cases have slightly higher I_1 values than do the corresponding RR + OBA cases. A comparison of the Jupiter, Saturn and Uranus data, Figures 32, 33 and 34 respectively, shows that both I_1 and the gradient of I_1 increase with each successive planet. For all three planets the correction schedule which yields the lowest values of I_1 is a single correction at the latest time. However, since I_1 does not include the effect of target error remaining after the last approach correction, it is of limited interest as a performance index.

A more meaningful survey parameter is the performance index I_2 . Results of the I_2 survey are presented in Figures 35, 36 and 37 for Jupiter, Saturn and Uranus respectively. For the RR + OBA case at Jupiter, Figure 35a, the contour pattern is very similar to the one for I_1 , the index I_2 being

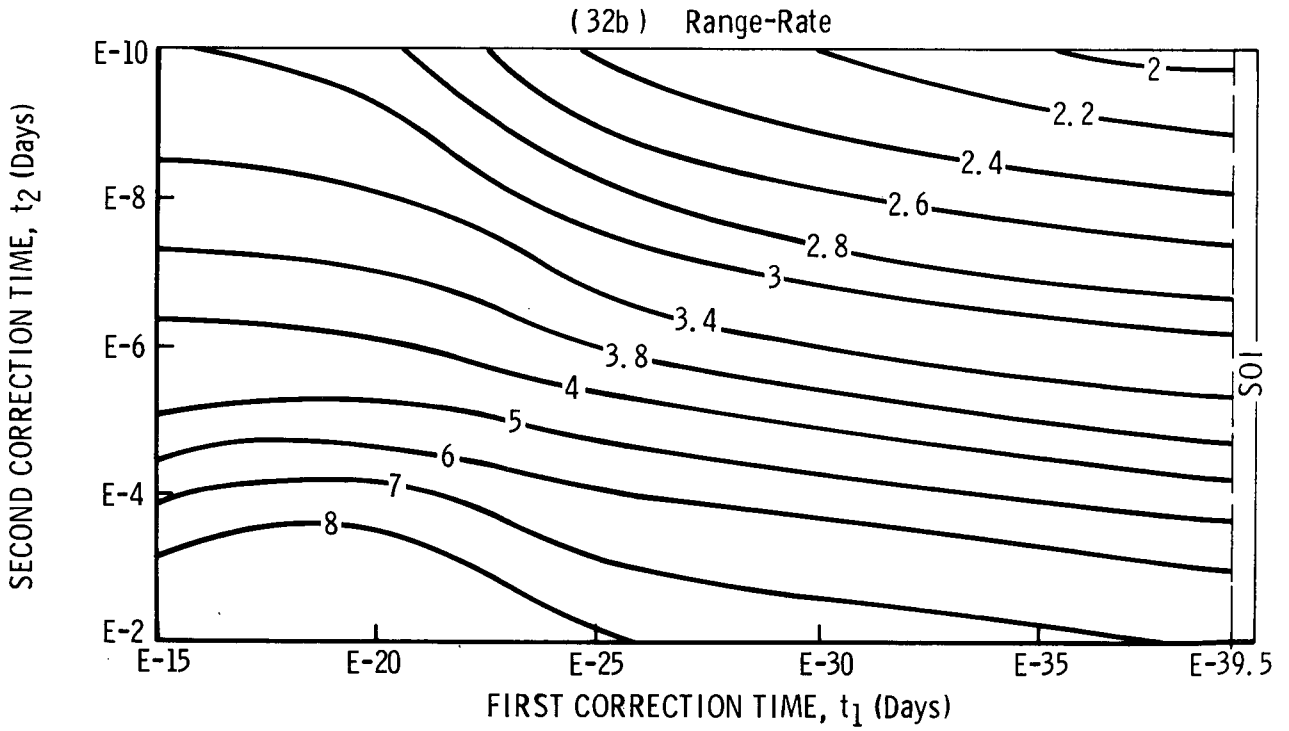
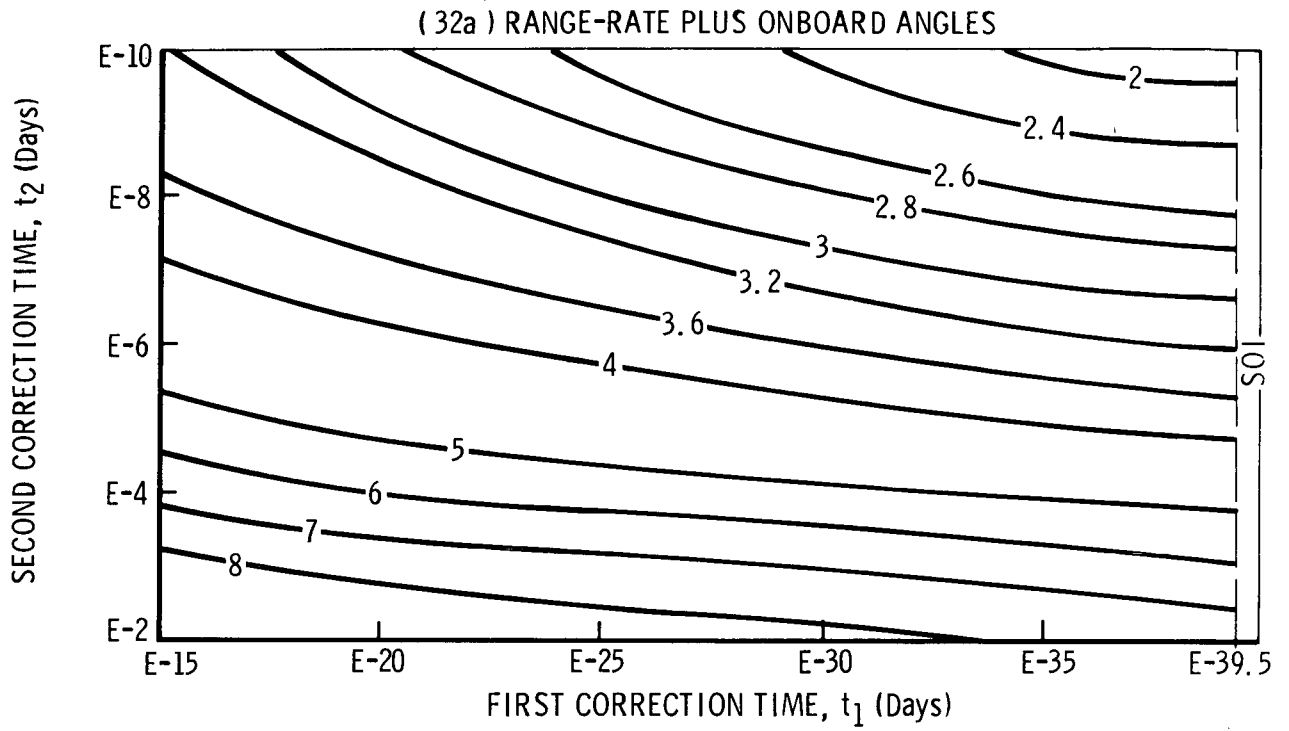


Figure 32 Survey of Guidance Performance Index I_1 , Jupiter

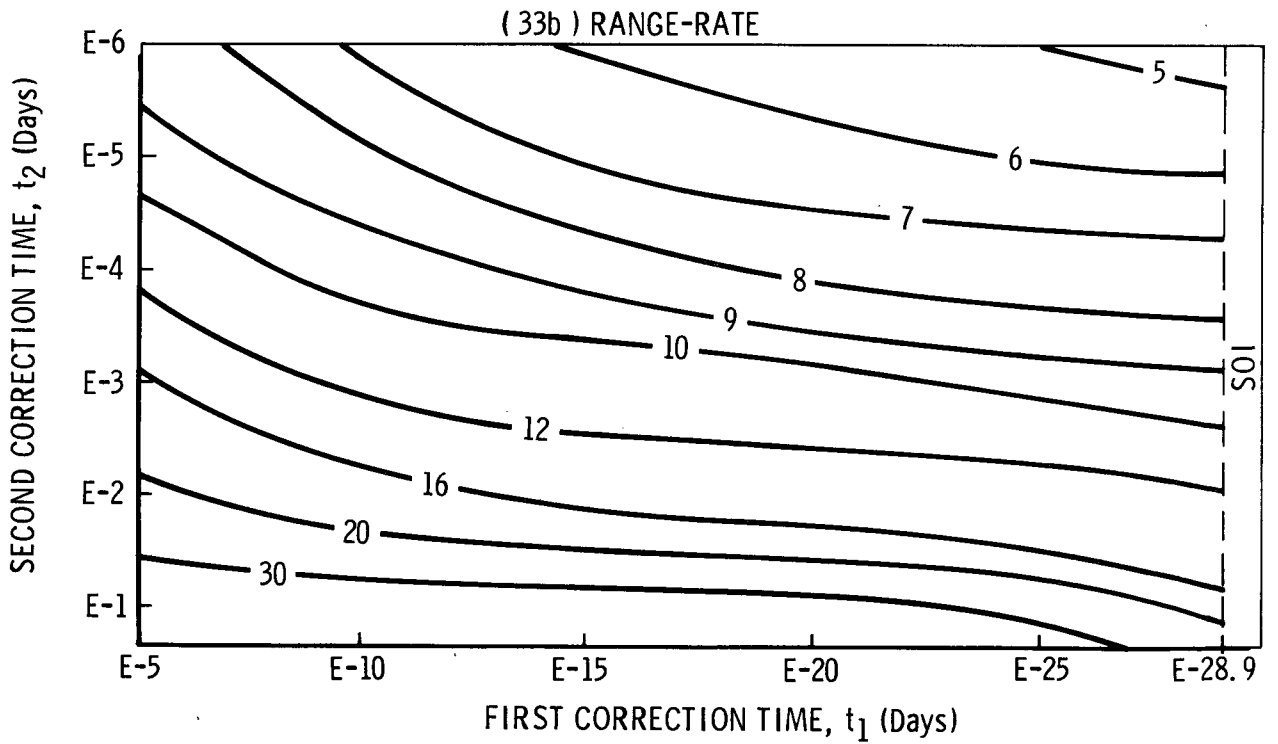
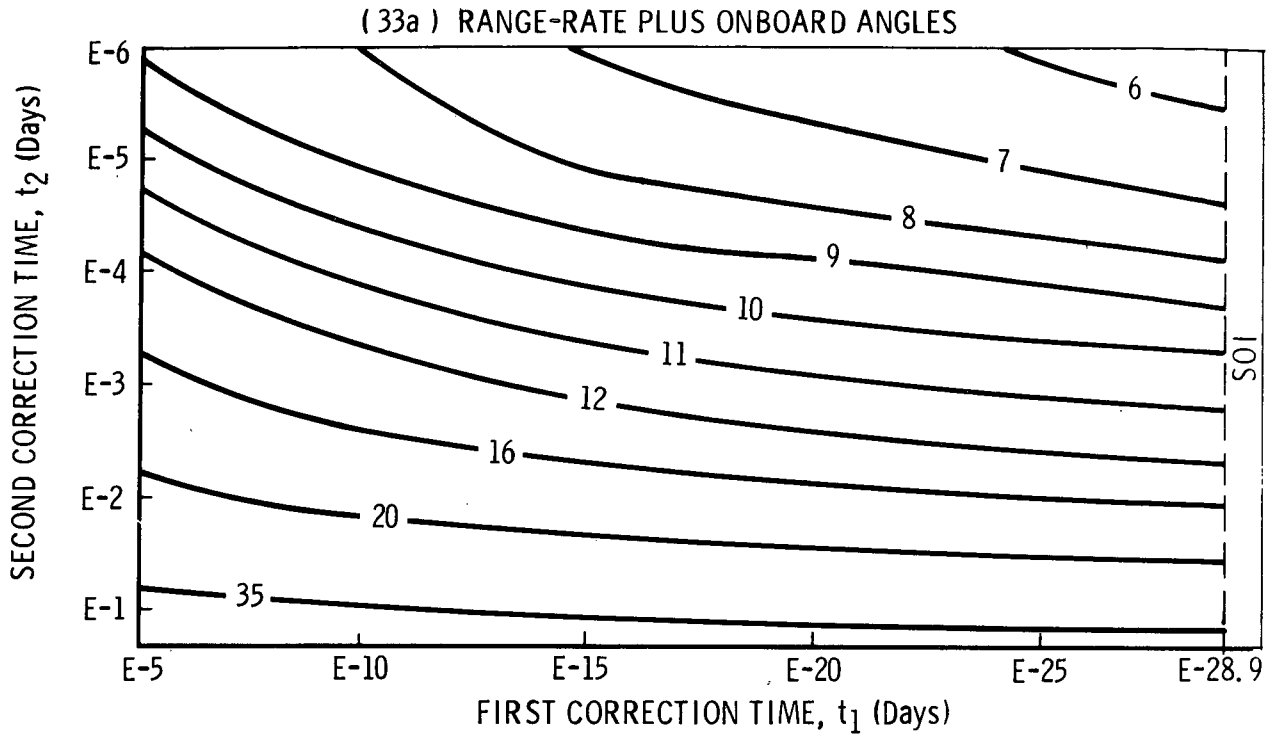


Figure 33 Survey of Guidance Performance Index I_1 , Saturn

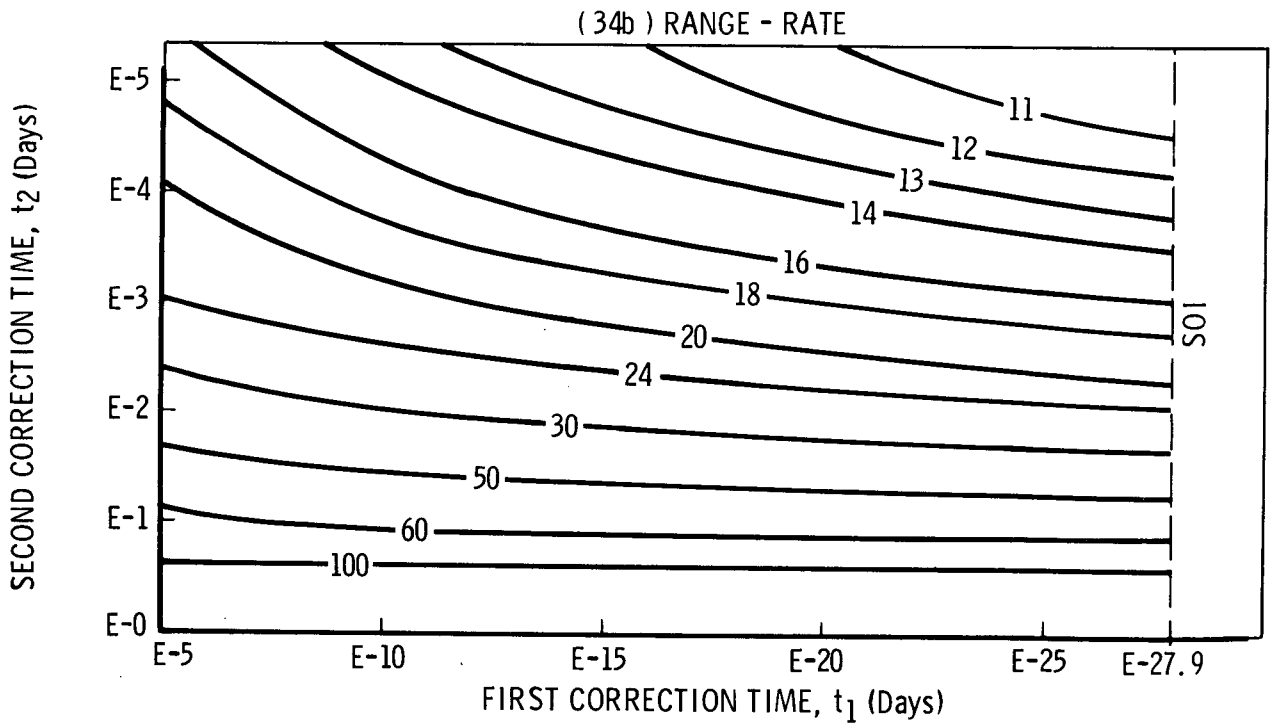
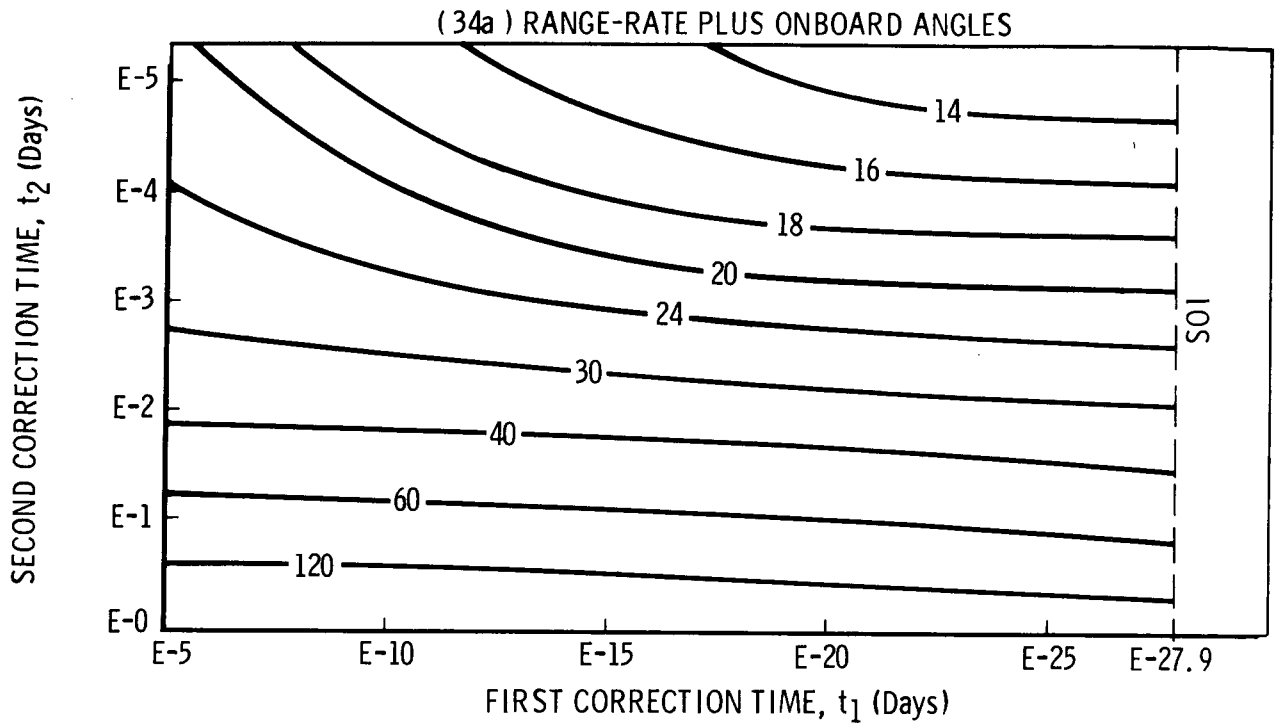


Figure 34 Survey of Guidance Performance Index I_1 , Uranus

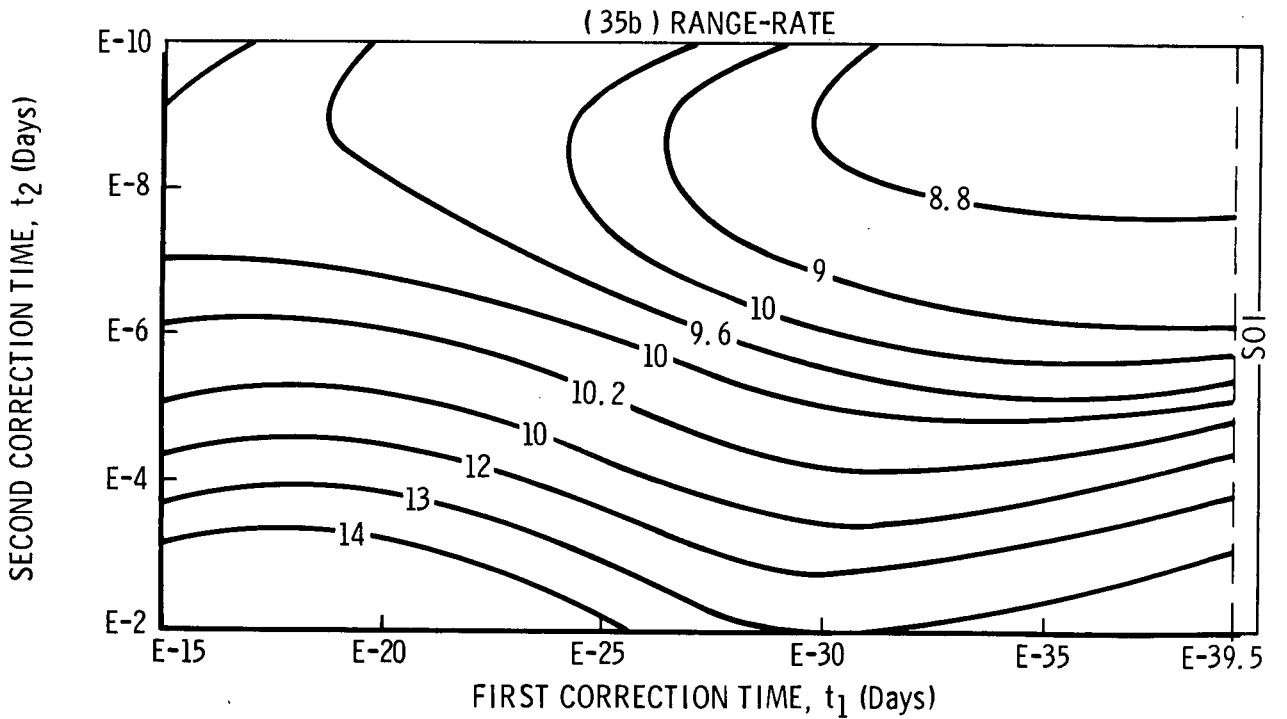
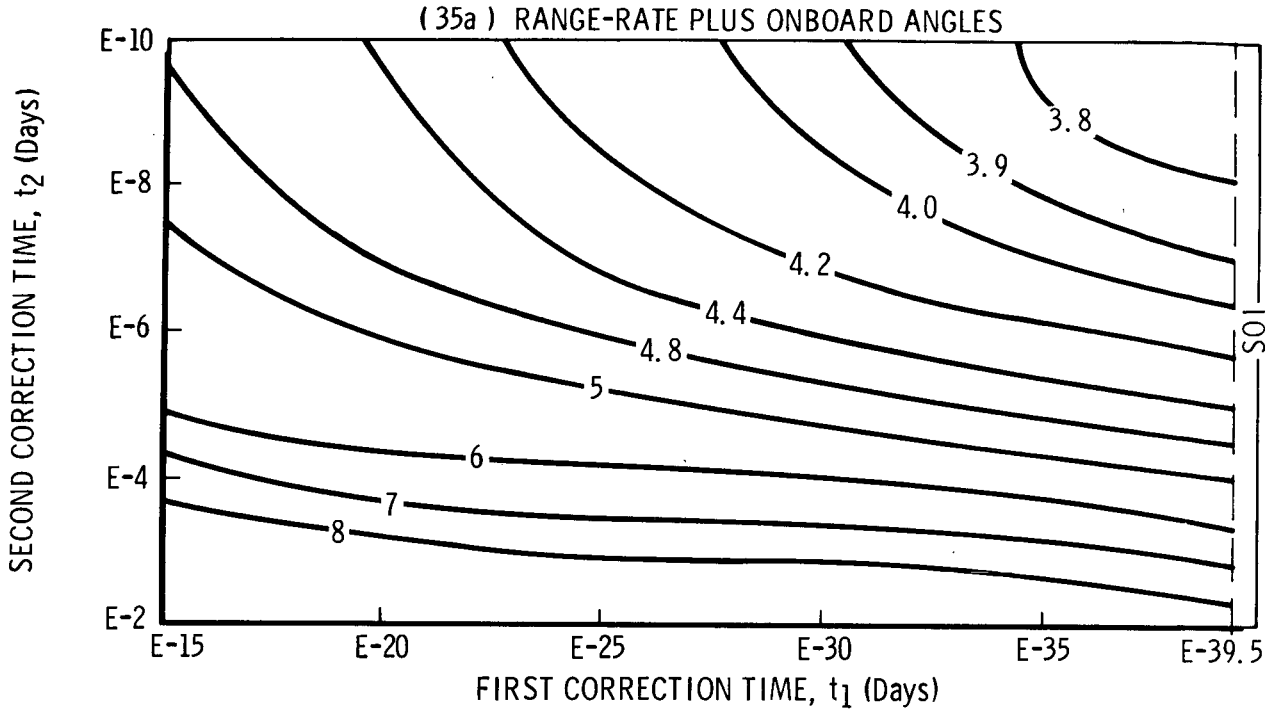


Figure 35 Survey of Guidance Performance Index I_2 , Jupiter

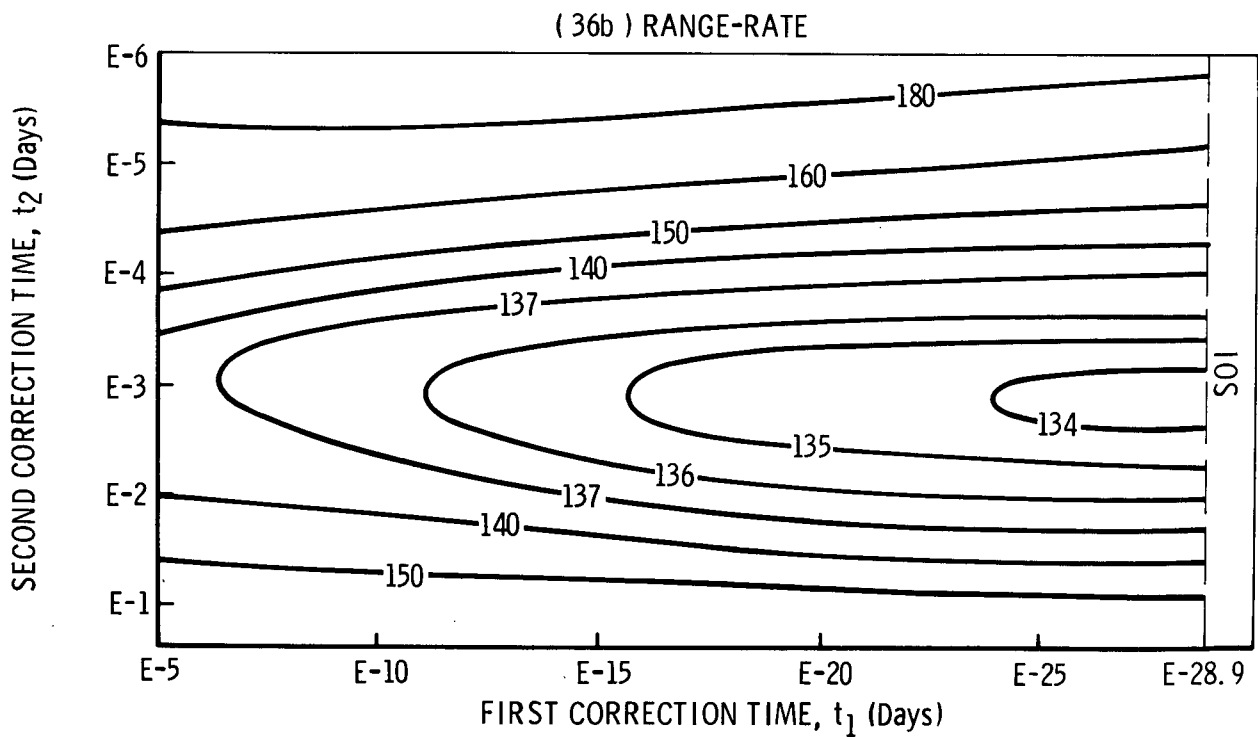
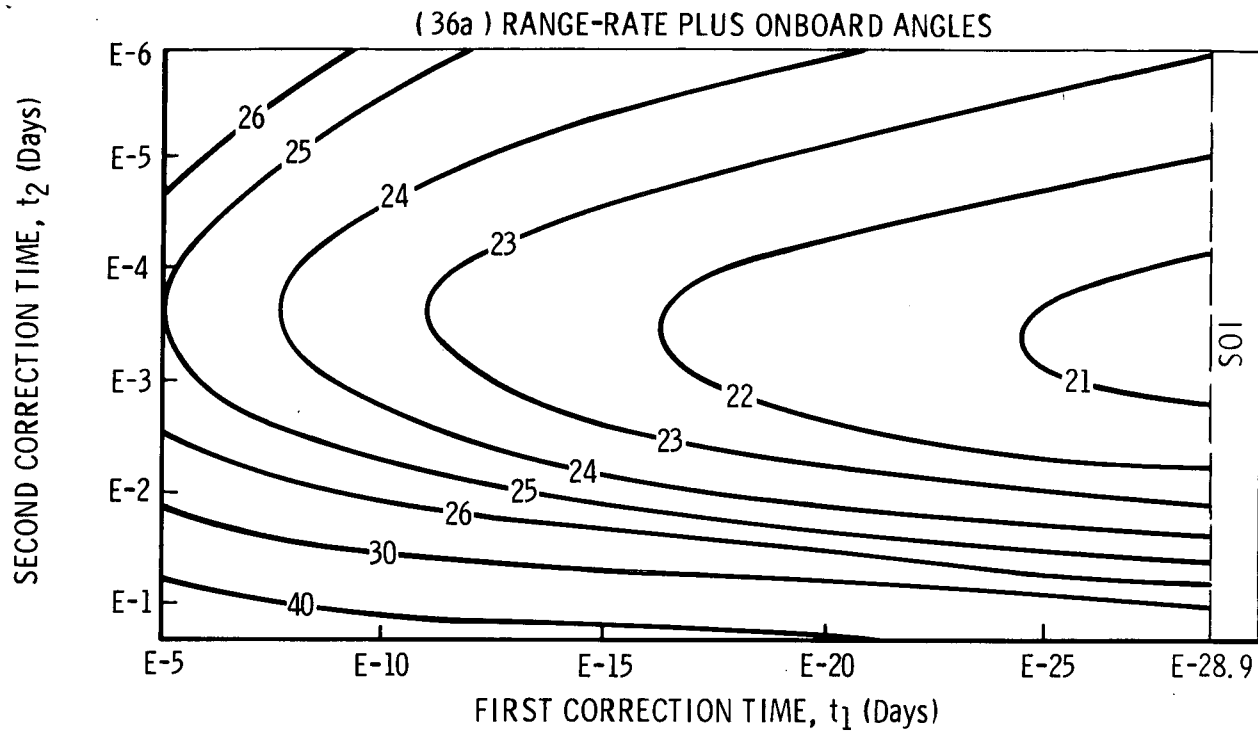


Figure 36 Survey of Guidance Performance Index I_2 , Saturn

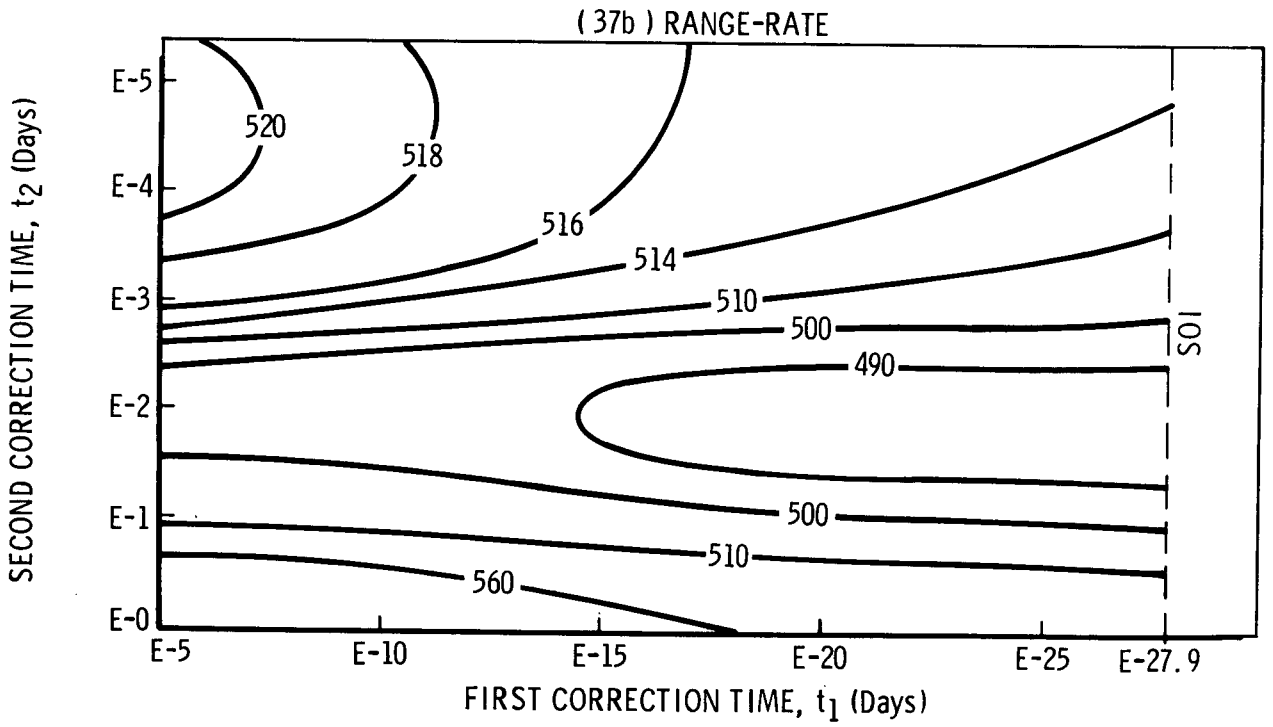
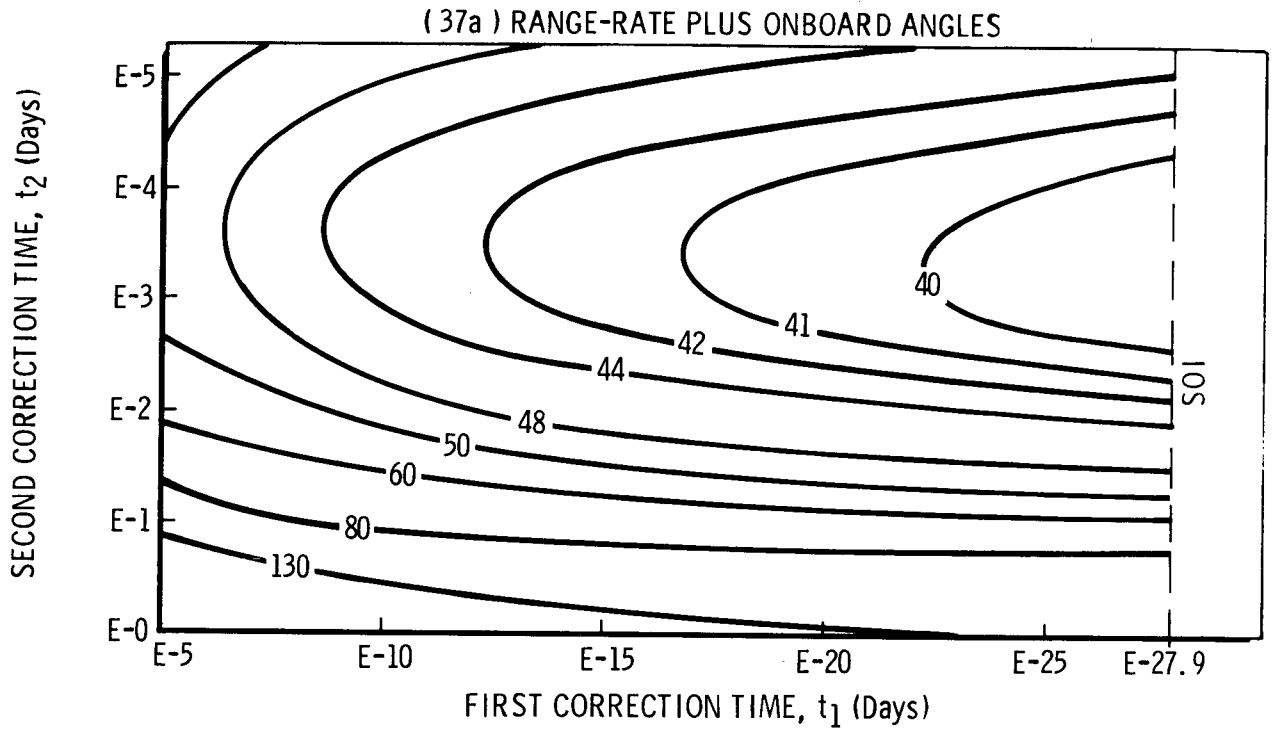


Figure 37 Survey of Guidance Performance Index I_2 , Uranus

much more sensitive to the second correction time than to the first. For a given first correction the second correction time for minimum I_2 appears to be near E-10 days. For the RR case at Jupiter, Figure 35b, a valley centered at about E-9 stretches across the survey area. The I_2 values for the RR case are larger than for the RR + OBA case and exhibit a much stronger gradient. The I_2 values for the RR case are on the order of two times greater than the corresponding I_2 values of the RR + OBA case.

The survey data for Saturn approach clearly define the region of minimum I_2 . For the RR + OBA case, Figure 36a, a valley extends across the space at $t_2 = E-3.5$. For the RR case the best second correction time decreases to $t_2 = E-3$. The I_2 values for the RR case are on the order of six times greater than the corresponding I_2 values of the RR + OBA case.

At Uranus the best times for the second correction are again easy to identify for the two observation cases. For the RR + OBA case, Figure 37a, the best second correction time is about E-3.5. The RR case exhibits a narrow horizontal valley at about $t_2 = 2$ with a steep I_2 gradient above and below the valley. A vertical ridge extends across the space at about $t_2 = E-4.5$. The I_2 values for the range-rate plus onboard angles case are roughly 12 times greater than the corresponding values for the RR case.

5.4 Guidance Sensitivity Analysis

The guidance survey presented in Section 5.2 provides important baseline data for preliminary assessment of the approach guidance propulsion requirements of the Grand Tour. A sensitivity analysis was performed on the nominal encounter profile at Jupiter, Saturn and Uranus to assess the sensitivity of these results to changes in the assumed error sources. For this analysis, the error sources and ground rules used for the reference navigation

accuracy analysis of Section 4.2 were retained. Both range-rate and onboard angle measurements were included. Additionally, the following approach guidance correction schedule was adopted:

Jupiter - one correction at E-9

Saturn - one correction at E-4

Uranus - one correction at E-3.

Results of the guidance sensitivity analysis are summarized in Table 6.

Standard deviations of range-rate and onboard angle observation errors were decreased to one-tenth of their nominal values (90 percent decrease) to determine the effect of improved observation accuracy. As can be seen from Table 6, the approach guidance correction requirements are insensitive to the observation accuracy. Post-correction target error, however, is moderately sensitive to changes in both RR and OBA accuracy. For the 90 percent decrease in RR error the target error decreased 33, 36 and 23 percent at Jupiter, Saturn and Uranus respectively. The 90 percent decrease in OBA error resulted in an 80, 87 and 86 percent decrease in target error at Jupiter, Saturn and Uranus, respectively.

One-sigma guidance correction errors were increased an order of magnitude (900 percent) to measure the effect of degraded guidance execution accuracy. Since only one approach guidance correction was specified, the approach velocity correction is not a function of guidance execution accuracy. Target error is relatively insensitive to guidance execution error. For the order of magnitude increase in the guidance magnitude errors, the resulting target error increases were 1.14, 2.26 and 7.90 percent at Jupiter, Saturn and Uranus, respectively. The corresponding target error increases due to increased orientation error were 1.72, 2.73 and 8.48 percent.

Table 6 Approach Guidance Sensitivities

Error Source	Parameter	Nominal Value	Change in Parameter %	JUPITER, $t_1 = E-9$				SATURN, $t_1 = E-4$				URANUS, $t_1 = E-3$			
				ΔV_{rms}		$\delta T'_{rms}$		ΔV_{rms}		$\delta T'_{rms}$		ΔV_{rms}		$\delta T'_{rms}$	
				m/sec	%	km	%	m/sec	%	km	%	m/sec	%	km	%
Observations															
Range-Rate	σ_ρ	.5 mm/sec	-90	0.00	0.00	-32	-33	0.01	0.00	-36	-36	0.00	0.00	-22	-23
Onboard Angles	$\sigma_\alpha, \sigma_\beta$	10 arc-sec	-90	0.00	0.00	-78	-80	0.01	0.00	-86	-87	0.00	0.00	-83	-86
Guidance Correction															
Magnitude	σ_κ	.001	900	0	0	1.12	1.14	0	0	2.24	2.26	0	0	7.60	7.90
Orientation	σ_γ	.001	900	0	0	1.68	1.72	0	0	2.70	2.73	0	0	8.19	8.48
Initial State Error	σ_{S_0}	*	100	4.88	214	0.10	0.10	15.19	200	0.15	0.15	19.1	200	0.51	0.52

*See Table 1

The diagonal elements (variances) of the initial state error covariance matrix, S_0 , were increased by a factor of four (100 percent increase in one-sigma values) to determine the effect of increased initial state errors. As can be seen from Table 6, the ΔV_{rms} values increase by 214, 200 and 200 percent at Jupiter, Saturn and Uranus, respectively. Thus, ΔV_{rms} is almost directly proportional to the standard deviation of the initial state errors. The post-correction target accuracy is relatively insensitive to the covariance of the initial state errors.

5.5 Monte Carlo Simulation

It is well known that the linear sequential estimation scheme used here yields poor results, and may diverge, if deviations from the nominal trajectory become too large. Furthermore, the scheme can provide a satisfactory state estimate while yielding an unrealistic error covariance matrix for the estimate. The guidance algorithm is also based on linear theory and is invalid for large state deviations. Therefore, it is necessary to test the validity of guidance statistics predicted by the linear navigation and guidance theory.

Initial State Errors

A Monte Carlo simulation of the navigation and guidance process during Saturn approach was conducted for the purpose of checking the adequacy of the linear theory. The Saturn approach was selected because it is generally considered to be the most critical encounter from a guidance standpoint. A one-correction guidance logic was adopted and a simulation was carried out for two different correction times: $t_1 = E-10$ and $t_1 = E-4$. For this analysis, the error sources and ground rules used for the guidance survey were retained except that the "true" initial state vector was simulated by adding a random

error vector to the nominal state vector. Components of the error vector were assumed to be uncorrelated and each was generated by sampling from its respective normal distribution (see Section 2.3). The distribution for each component is defined by a zero mean and a variance equal to the diagonal elements of the covariance matrix S_o . Since $S_o = P_o$, the variances are those values listed in Table 2. Values of the mean and standard deviation of each component are listed in Table 7 for the 35 simulation runs.

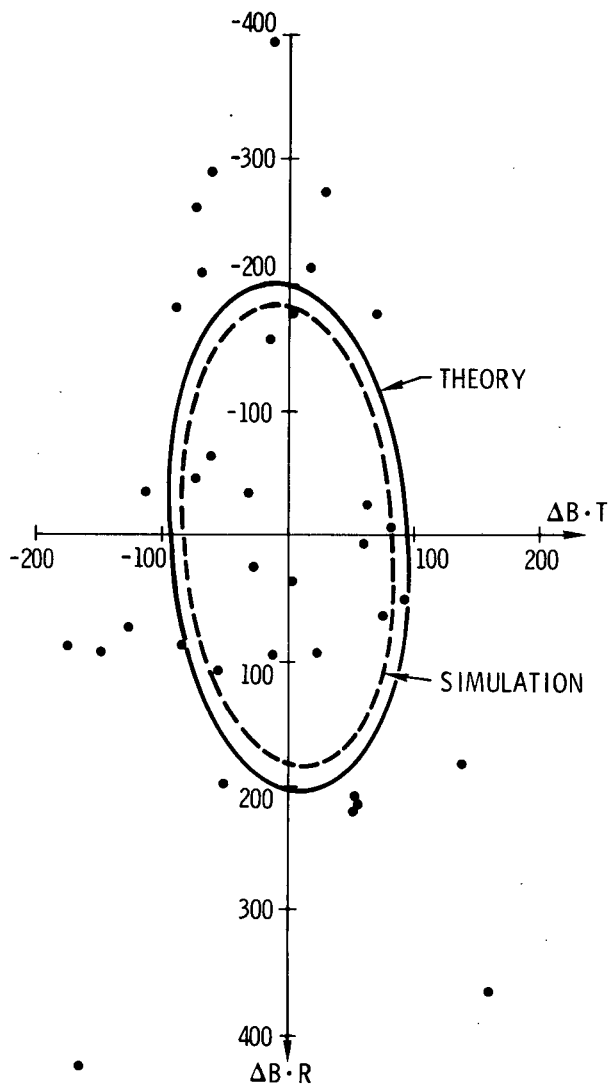
Monte Carlo Results

The results of the simulations are presented in Figure 38. Actual values of the target parameters B·R and B·T are plotted with respect to the nominal target point. The standard probability ellipses representing the bivariate distribution of the predicted target error are shown for comparison. Pertinent statistics of the simulated data are contained in Table 8. The table contains values for the mean and standard deviation of the target errors, the magnitude of the velocity corrections, $\Delta V'$, and the magnitude of the error vector, $|\delta T'| = [\delta B \cdot R^2 + \delta B \cdot T^2]^{1/2}$.

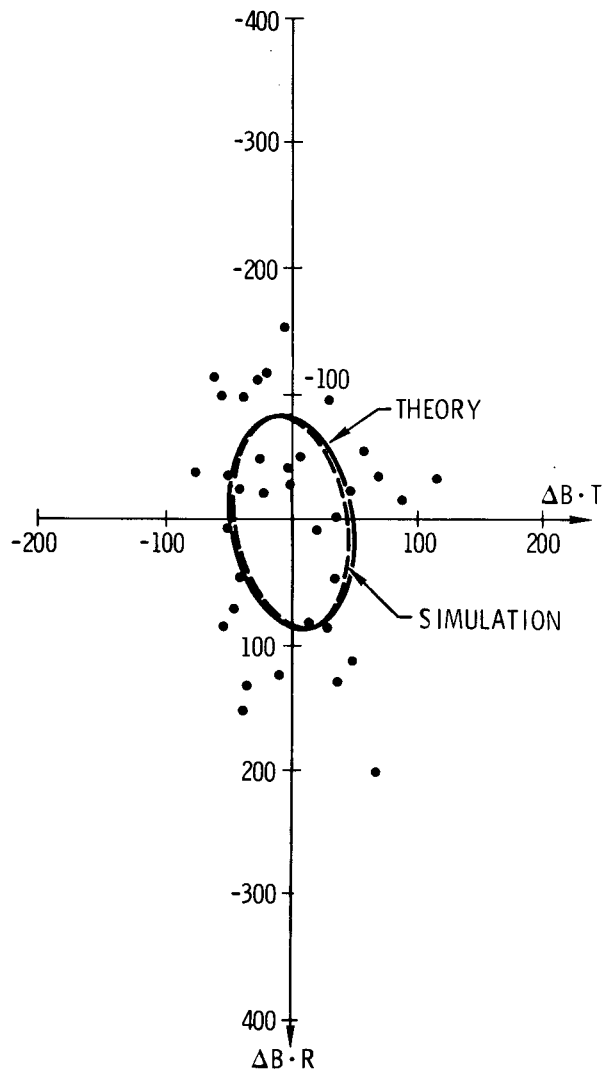
Even for the relatively small sample size (35 runs), the correlation between the simulation statistics and the predicted statistics is reasonably good for the $t_2 = E-10$ case and very good for the $t_2 = E-4$ case. For the E-10 case, Figure 38a, the mean of the simulation errors is 2.3 km for $\delta B \cdot R$ and is -14.0 km for $\delta B \cdot T$ compared to predicted values of zero for both. Standard deviations of $\delta B \cdot R$ and $\delta B \cdot T$ are 185 and 82 km, respectively, compared with predicted values of 201 and 92 km. Theory predicts a $\Delta V'$ RMS value one percent greater than the value obtained by simulation (3.03 m/sec compared to 3.00 m/sec). The actual RMS value for the magnitude of the target error, $|\delta T'|$, is 203 km compared with a predicted value of 221 km.

Table 7 Simulated Initial State Error Statistics

Component	Mean	One-Sigma
x (km)	-122	1432
y (km)	-196	1010
z (km)	204	1473
\dot{x} (km/day)	3.06	16.2
\dot{y} (km/day)	3.33	13.5
\dot{z} (km/day)	-1.18	16.7
b_x (km)	-350	1466
b_y (km)	108	1118
b_z (km)	93	1288



(38a) E-10



(38b) E-4

Figure 38 Monte Carlo Simulation Results

39

Table 8 Monte Carlo Simulation Results

Parameter	$t_1 = E-10$		$t_1 = E-4$	
	Mean	1-Sigma	Mean	1-Sigma
$\Delta V'$ (m/sec)	2.85	1.03	7.22	2.70
$ \delta T' $ (km)	175	101	96	52
$\delta B \cdot R$ (km)	2.3	185	2.7	87
$\delta B \cdot T$ (km)	-14.0	82	1.2	46
δt_e (days)	2.10(-6)	1.95(-5)	2.67(-6)	9.83(-6)

For the E-4 case, Figure 38b, the mean of the simulation errors is 2.7 km for $\delta B \cdot R$ and is 1.2 km for $\delta B \cdot T$ compared to predicted values of zero for both. Standard deviations of $\delta B \cdot R$ and $\delta B \cdot T$ are 87 and 46 km, respectively, compared with predicted values of 86 and 49 km. The $\Delta V'$ RMS value of the simulation is 7.7 m/sec compared with 7.6 m/sec predicted by theory (1.5% greater). The actual RMS value for the magnitude of the target error is 109 km compared with a predicted value of 99 km.

Correlation between theory and simulation should improve as the sample size is increased. However, based on the analysis discussed above, it can be concluded that the navigation and guidance algorithm formulated in Chapter 2 provides an adequate model for preliminary mission analysis of the Grand Tour. For the example selected for simulation, the theory slightly over-predicted the simulation RMS values of $|\delta T'|$ and $\Delta V'$. For the E-10 case, RMS values of $\Delta V'$ and $|\delta T'|$ are 6 and 17 percent larger, respectively, than the corresponding mean values. For the E-4 case the RMS values of $\Delta V'$ and $|\delta T'|$ are 7 and 13 percent larger than the corresponding mean values. Thus, RMS values of correction magnitude and target error magnitude appear to be good first approximations to the mean of their non-Gaussian distributions.

CHAPTER 6

CONCLUSIONS AND RECOMMENDATIONS

The investigation reported here was concerned with the simulation and analysis of the navigation and guidance process for the Jupiter, Saturn and Uranus encounter phases of the 1977 Grand Tour Interior Mission.

Principal Conclusions

From an examination of the theoretical development of the navigation and guidance algorithms in Chapter 2, it can be concluded that the error in the position of the outer planets can be conveniently included as a parameter to be estimated if the error is assumed constant over the encounter period.

Based on a study of the navigation data presented in Chapter 4 the following conclusions can be drawn:

1. Range-rate data provide adequate in-plane navigation accuracies but poor out-of-plane navigation accuracies during the approach phase at each planet.
2. Although onboard angle data provide relatively poor navigation accuracies in terms of the planetocentric state of the spacecraft, the data yield good estimates for the position components of the target vector, i.e., B·R and B·T.
3. Combining onboard angle data with range-rate data leads to a significant improvement in overall navigation accuracy at each planet.

4. Range data, when combined with range-rate data, provide only slight improvement over the range-rate only data at each planet.
5. Onboard angle data alone does not significantly reduce planetocentric spacecraft position uncertainty at Jupiter until the spacecraft reaches periapsis. At Saturn onboard angle data yield better planetocentric position accuracy than do the range-rate data up to about E-15 days. The same is true at Uranus where the crossover point is about E-10 days. Near periapsis the range-rate data is superior for all three planets.
6. Range-rate data provide better planetocentric velocity accuracy during planet approach than do the onboard angle data. Combining onboard angle data with range-rate data does not result in a significant decrease in velocity uncertainty over the range-rate only case except at Uranus.
7. Range-rate observations alone provide a significant improvement in Jupiter and Saturn position uncertainty, but only a slight improvement in Uranus position uncertainty. Onboard angle data alone provide virtually no planet position information.
8. Combined range-rate and onboard angle data provide a significantly smaller planet position uncertainty than the range-rate data alone.
9. Range-rate data provide practically no B·R and B·T information until the spacecraft is well within the planet's sphere of influence. As the spacecraft nears encounter the B·T uncertainty decreases rapidly while the B·R uncertainty decreases at a much slower rate.

10. Onboard angle data provide good B·R and B·T accuracy but poor t_e accuracy.
11. Adding star-planet onboard angle (an out-of-plane angle) observations to the range-rate observations decreases B·R uncertainty significantly. A combination of all three observation types (range-rate plus both onboard angles) yields good target accuracy in all three target components.

From a study of the guidance analysis results presented in Chapter 5 the following conclusions are reached:

1. A survey of approach ΔV_{rms} requirements for a two-correction guidance logic indicates that: (a) the sum of the approach and departure ΔV_{rms} values is sensitive to the time of the second correction, but relatively insensitive to the time of the first correction; (b) the sensitivity to the second correction time is greater for the range-rate case than for the range-rate plus onboard angle case; (c) the optimum correction times for the second approach corrections is later for the range-rate plus onboard angle case than for the range-rate case, and (d) the optimum correction times for the second approach correction are near the following survey values:

	RR	RR + OBA
Jupiter	E-9	E-10
Saturn	E-3	E-3.5
Uranus	E-2	E-3.5

2. A sensitivity analysis of the navigation and guidance process demonstrated that: (a) post-correction target error is relatively

insensitive to both initial state error and guidance execution error; (b) post-correction target error is moderately sensitive to both range-rate and onboard angle observation accuracy, being more sensitive to onboard angle accuracy than to range-rate accuracy; and (c) guidance correction requirements are insensitive to observation accuracy but are almost directly proportional to the standard deviation of the initial state errors.

3. Results of a Monte Carlo simulation of the navigation and guidance process verify that the linear estimation and guidance theory provides an adequate model for preliminary mission analysis of the Grand Tour.

Recommendations for Future Study

The research reported here uncovered several areas which should be considered for future study. The following specific studies are recommended:

1. An extension of the analysis reported here to include other observation types (e.g., moon-star and moon-planet angles) and other missions (e.g., the three planet Grand Tour missions). Accordingly, the computer programs STEP V and STEP VI should be modified to include the capability to simulate and process additional observation types.
2. A study of the effect of other error sources (e.g., unmodeled accelerations, planet mass uncertainty, tracking station location errors, and planet center finding bias) on navigation accuracy and guidance requirements. Computer programs STEP V and STEP VI could be modified to provide options for estimating (or including but not estimating) additional error parameters.

3. A study of the effect of secondary perturbations on the motion of the spacecraft during encounter. A more sophisticated dynamical model which includes planetary oblateness and the perturbation of additional bodies should be considered for incorporation into the STEP V and STEP VI computer programs.
4. A study of alternate guidance parameters for planetary flyby missions should be conducted to determine the best target vector for the Grand Tour missions.
5. The interactive graphics feature of computer program STEP VI should be further developed to exploit the full capabilities of the CDC 6600/252 interactive system. For example, additional problem status displays could be added to automatically display pertinent data as problem execution proceeds. Also, use of the light pen feature would greatly improve the manipulation of input data.
6. An analysis of information lag times due to light travel time should be made to determine the effect on navigation and guidance requirements.

APPENDICES

APPENDIX A
NOMINAL GRAND TOUR MISSION DATA

Mission/trajectory data for the 1977 Grand Tour Interior mission are presented in the following tables. Trajectory parameters which define the four heliocentric legs of the mission are shown in Table 9. The classical elements which define the orientation of the transfer conics (i , Ω , ω) are defined with respect to the equinox and ecliptic of date. Parameters which define the encounter trajectory are presented in Table 10. The classical elements which define the orientation of the encounter conics are defined with respect to a planetocentric equatorial coordinate system.

The nominal mission data were generated using a computer program developed by M. C. Poteet of Convair Aerospace, Fort Worth, Texas. The program generates an approximate solution to multi-planet flyby missions by solving for the heliocentric transfer conics which match the hyperbolic excess speeds at arrival and departure. The heliocentric solution defines heliocentric velocity requirements, and thus, the hyperbolic asymptotes, at arrival and departure. The asymptotes and the excess speed completely define the planetocentric flyby conic.

Table 9 Heliocentric Trajectory Parameters

LEG	JULIAN DATE 244-		DURATION DAYS	a 10 ⁶ km	e	i deg	Ω deg	ω deg	TRANSFER ANGLE deg
	DEPART	ARRIVE							
Earth-Jupiter	3390.5	3895.8	505.3	951.9	.842	.867	-19.11	2.38	145
Jupiter-Saturn	3895.8	4472.2	576.4	-459.2	2.690	2.449	111.18	- .206	43
Saturn-Uranus	4472.2	5701.8	1229.6	-258.6	6.470	2.379	70.74	113.34	76
Uranus-Neptune	5701.8	6700.0	998.2	-208.6	12.151	2.365	-112.28	-34.98	62

Table 10 Planetocentric Flyby Parameters

	ENCOUNTER DATE		ENCOUNTER CONDITIONS			EXCESS VELOCITY km/sec	ϕ deg	a 10^3 km	e	i deg	TARGET PARAMETER, b 10^3 km
			ALTITUDE		VELOCITY						
	JD 244-	CIVIL	10^3 km	RADII	km/sec						
Jupiter	3895.5	22 Jan 79	194.5	2.73	33.23	12.3	98.8	-838.4	1.32	5.6	718.7
Saturn	4472.2	20 Aug 80	2.4	0.04	38.62	16.9	85.5	-132.7	1:47	29.2	143.6
Uranus	5701.8	2 Jan 84	13.1	0.56	27.85	21.4	29.7	- 12.6	3.90	100.1	47.6
Neptune	6700.0	26 Sep 86	OPEN			23.9	OPEN				

APPENDIX B

THE DYNAMICAL EQUATIONS IN RECTANGULAR CARTESIAN COORDINATES

The differential equation of state, Eq. (2.9), can be written in a rectangular cartesian coordinate system as

$$\dot{\mathbf{X}} = \begin{bmatrix} \dot{x} \\ \dot{y} \\ \dot{z} \\ \dot{u} \\ \dot{v} \\ \dot{w} \\ \dot{b}_x \\ \dot{b}_y \\ \dot{b}_z \end{bmatrix} = \begin{bmatrix} F_1 \\ F_2 \\ F_3 \\ F_4 \\ F_5 \\ F_6 \\ F_7 \\ F_8 \\ F_9 \end{bmatrix} \quad (\text{B.1})$$

where

$$F_1 = u$$

$$F_2 = v$$

$$F_3 = w$$

$$F_4 = -\frac{\mu x}{r^3} - \mu_s \left[\frac{x + X_t}{R^3} - \frac{X_t}{R_t^3} \right]$$

$$F_5 = -\frac{\mu y}{r^3} - \mu_s \left[\frac{y + Y_t}{R^3} - \frac{Y_t}{R_t^3} \right]$$

$$F_6 = -\frac{\mu z}{r^3} - \mu_s \left[\frac{z + Z_t}{R^3} - \frac{Z_t}{R_t^3} \right]$$

$$F_7 = 0$$

$$F_8 = 0$$

$$F_9 = 0$$

The heliocentric position components of the target planet can be expressed as

$$X_t = X_t^* + b_x$$

$$Y_t = Y_t^* + b_y \quad (\text{B.2})$$

$$Z_t = Z_t^* + b_z$$

where X_t^* , Y_t^* , and Z_t^* are the components of the nominal heliocentric position vectors obtained from the planetary ephemeris subroutine and b_x , b_y and b_z are components of bias in the planet position vector. The bias in the planetary position vector represents an error in the ephemeris of the target planet which is assumed to be constant over the time period of interest.

The state transition matrix is evaluated by numerical integration of the matrix differential equation

$$\dot{\Phi}(t, t_0) = A(t) \Phi(t, t_0) \quad (\text{B.3})$$

with initial conditions $\Phi(t_0, t_0) = I$,

where $A(t) = \left[\frac{\partial F}{\partial X} \right]^*$ is a 9x9 matrix of partial derivatives evaluated on the nominal trajectory. For convenience the A-matrix can be partitioned into nine submatrices as follows:

$$A = \begin{bmatrix} 0 & I_3 & 0 \\ \hline A_{21} & 0 & A_{23} \\ \hline 0 & 0 & 0 \end{bmatrix} \quad (\text{B.4})$$

The symmetric submatrices A_{21} and A_{23} are defined below.

$$A_{21} = \begin{bmatrix} a_{41} & a_{42} & a_{43} \\ a_{51} & a_{52} & a_{53} \\ a_{61} & a_{62} & a_{63} \end{bmatrix}; \quad A_{23} = \begin{bmatrix} a_{47} & a_{48} & a_{49} \\ a_{57} & a_{58} & a_{59} \\ a_{67} & a_{68} & a_{69} \end{bmatrix} \quad (\text{B.5})$$

where

$$a_{41} = \frac{\partial F_4}{\partial x} = \mu \left[\frac{3x^2}{r^5} - \frac{1}{r^3} \right] + \mu_s \left[\frac{3X^2}{R^5} - \frac{1}{R^3} \right]$$

$$a_{42} = \frac{\partial F_4}{\partial y} = \mu \left[\frac{3xy}{r^5} \right] + \mu_s \left[\frac{3xy}{R^5} \right]$$

$$a_{43} = \frac{\partial F_4}{\partial z} = \mu \left[\frac{3xz}{r^5} \right]$$

$$a_{51} = \frac{\partial F_5}{\partial x} = a_{42}$$

$$a_{52} = \frac{\partial F_5}{\partial y} = \mu \left[\frac{3y^2}{r^5} - \frac{1}{r^3} \right] + \mu_s \left[\frac{3Y^2}{R^5} - \frac{1}{R^3} \right]$$

$$a_{53} = \frac{\partial F_5}{\partial z} = \mu \left[\frac{3yz}{r^5} \right] + \mu_s \left[\frac{3YZ}{R^5} \right]$$

$$a_{61} = \frac{\partial F_6}{\partial x} = a_{43}$$

$$a_{62} = \frac{\partial F_6}{\partial y} = a_{53}$$

$$a_{63} = \frac{\partial F_6}{\partial z} = \mu \left[\frac{3z^2}{r^5} - \frac{1}{r^3} \right] + \mu_s \left[\frac{3Z^2}{R^5} - \frac{1}{R^3} \right]$$

$$a_{47} = \frac{\partial F_4}{\partial b_x} = \mu_s \left[\frac{3X^2}{R^5} - \frac{3X_t^2}{R_t^5} - \frac{1}{R^3} + \frac{1}{R_t^3} \right]$$

$$a_{48} = \frac{\partial F_4}{\partial b_y} = \mu_s \left[\frac{3XY}{R^5} - \frac{3X_t Z_t}{R_t^5} \right]$$

$$a_{49} = \frac{\partial F_4}{\partial b_z} = \mu_s \left[\frac{3XZ}{R^5} - \frac{3X_t Z_t}{R_t^5} \right]$$

$$a_{57} = \frac{\partial F_5}{\partial b_x} = a_{48}$$

$$a_{58} = \frac{\partial F_5}{\partial b_y} = \mu_s \left[\frac{3Y^2}{R^5} - \frac{3Y_t^2}{R_t^5} - \frac{1}{R^3} + \frac{1}{R_t^3} \right]$$

$$a_{59} = \frac{\partial F_5}{\partial b_z} = \mu_s \left[\frac{3YZ}{R^5} - \frac{3Y_t Z_t}{R_t^5} \right]$$

$$a_{67} = \frac{\partial F_6}{\partial b_x} = a_{49}$$

$$a_{68} = \frac{\partial F_6}{\partial b_y} = a_{59}$$

$$a_{69} = \frac{\partial F_6}{\partial b_z} = \mu_s \left[\frac{3Z^2}{R^5} - \frac{3Z_t^2}{R_t^5} - \frac{1}{R^3} + \frac{1}{R_t^3} \right] .$$

(B.6)

APPENDIX C

THE OBSERVATION-STATE RELATIONSHIPS IN RECTANGULAR CARTESIAN COORDINATES

The functional relationships between the observations and the components of the state vector can be written in a rectangular cartesian coordinate system as follows:

$$\rho = [(X - X_s)^2 + (Y - Y_s)^2 + (Z - Z_s)^2]^{1/2} \tag{C.1}$$

$$\dot{\rho} = [(\dot{X} - \dot{X}_s)(X - X_s) + (\dot{Y} - \dot{Y}_s)(Y - Y_s) + (\dot{Z} - \dot{Z}_s)(Z - Z_s)]/\rho \tag{C.2}$$

$$\alpha = \cos^{-1}[(xX_t + yY_t + zZ_t + r^2)/(rR)] \tag{C.3}$$

$$\beta = \cos^{-1}[-(xs_x + ys_y + zs_z)/r] \tag{C.4}$$

where

$$X = X_t^* + b_x + x \tag{C.5}$$

$$Y = Y_t^* + b_y + y \tag{C.6}$$

$$Z = Z_t^* + b_z + z \tag{C.7}$$

$$R = [X^2 + Y^2 + Z^2]^{1/2} \tag{C.8}$$

$$r = [x^2 + y^2 + z^2]^{1/2} \tag{C.9}$$

and s_x , s_y , and s_z are the direction cosines of the navigation star direction.

The linearized observation-state relationship

$$y(t) = \hat{H}(t) x(t) \tag{C.10}$$

in component form becomes

$$\begin{bmatrix} \delta\rho \\ \delta\dot{\rho} \\ \delta\alpha \\ \delta\beta \end{bmatrix} = \begin{bmatrix} h_{11} & h_{12} & \dots & h_{19} \\ & h_{21} & & \\ & h_{31} & & \\ & h_{41} & \dots & h_{49} \end{bmatrix} \begin{bmatrix} \delta x \\ \delta y \\ \delta z \\ \delta u \\ \delta v \\ \delta w \\ \delta b_x \\ \delta b_y \\ \delta b_z \end{bmatrix} \quad (C.11)$$

where []* indicates that the elements of the $\tilde{H}(t)$ matrix are evaluated on the reference trajectory, $X^*(t)$.

The elements of the \tilde{H} -matrix are as follows:

$$h_{11} = \frac{\partial \rho}{\partial x} = (X - X_s)/\rho$$

$$h_{12} = \frac{\partial \rho}{\partial y} = (Y - Y_s)/\rho$$

$$h_{13} = \frac{\partial \rho}{\partial z} = (Z - Z_s)/\rho$$

$$h_{14} = \frac{\partial \rho}{\partial u} = 0$$

$$h_{15} = \frac{\partial \rho}{\partial v} = 0$$

$$h_{16} = \frac{\partial \rho}{\partial w} = 0$$

$$h_{17} = \frac{\partial \rho}{\partial b_x} = h_{11}$$

$$h_{18} = \frac{\partial \rho}{\partial b_y} = h_{12}$$

$$h_{19} = \frac{\partial \rho}{\partial b_z} = h_{13}$$

$$h_{21} = \frac{\partial \dot{\rho}}{\partial x} = [(\dot{X} - \dot{X}_S) - (X - X_S)(\dot{\rho}/\rho)]/\rho$$

$$h_{22} = \frac{\partial \dot{\rho}}{\partial y} = [(\dot{Y} - \dot{Y}_S) - (Y - Y_S)(\dot{\rho}/\rho)]/\rho$$

$$h_{23} = \frac{\partial \dot{\rho}}{\partial z} = [(\dot{Z} - \dot{Z}_S) - (Z - Z_S)(\dot{\rho}/\rho)]/\rho$$

$$h_{24} = \frac{\partial \dot{\rho}}{\partial u} = h_{11}$$

$$h_{25} = \frac{\partial \dot{\rho}}{\partial v} = h_{12}$$

$$h_{26} = \frac{\partial \dot{\rho}}{\partial w} = h_{13}$$

$$h_{27} = \frac{\partial \dot{\rho}}{\partial b_x} = h_{21}$$

$$h_{28} = \frac{\partial \dot{\rho}}{\partial b_y} = h_{22}$$

$$h_{29} = \frac{\partial \dot{\rho}}{\partial b_z} = h_{23}$$

$$h_{31} = \frac{\partial \alpha}{\partial x} = \left[\cos \alpha \left[\frac{x}{r^2} + \frac{x}{R^2} \right] - \frac{(x+X)}{rR} \right] \frac{1}{\sin \alpha}$$

$$h_{32} = \frac{\partial \alpha}{\partial y} = \left[\cos \alpha \left[\frac{y}{r^2} + \frac{Y}{R^2} \right] - \frac{(y+Y)}{rR} \right] \frac{1}{\sin \alpha}$$

$$h_{33} = \frac{\partial \alpha}{\partial z} = \left[\cos \alpha \left[\frac{z}{r^2} + \frac{Z}{R^2} \right] - \frac{(z+Z)}{rR} \right] \frac{1}{\sin \alpha}$$

$$h_{34} = \frac{\partial \alpha}{\partial u} = 0$$

$$h_{35} = \frac{\partial \alpha}{\partial v} = 0$$

$$h_{36} = \frac{\partial \alpha}{\partial w} = 0$$

$$h_{37} = \frac{\partial \alpha}{\partial b_x} = \left[\cos \alpha \frac{X}{R^2} - \frac{x}{rR} \right] \frac{1}{\sin \alpha}$$

$$h_{38} = \frac{\partial \alpha}{\partial b_y} = \left[\cos \alpha \frac{Y}{R^2} - \frac{y}{rR} \right] \frac{1}{\sin \alpha}$$

$$h_{39} = \frac{\partial \alpha}{\partial b_z} = \left[\cos \alpha \frac{Z}{R^2} - \frac{z}{rR} \right] \frac{1}{\sin \alpha}$$

$$h_{41} = \frac{\partial \beta}{\partial x} = \left[s_x + \frac{x \cos \beta}{r} \right] \frac{1}{r \sin \beta}$$

$$h_{42} = \frac{\partial \beta}{\partial y} = \left[s_y + \frac{y \cos \beta}{r} \right] \frac{1}{r \sin \beta}$$

$$h_{43} = \frac{\partial \beta}{\partial z} = \left[s_z + \frac{z \cos \beta}{r} \right] \frac{1}{r \sin \beta}$$

$$h_{44} = \frac{\partial \beta}{\partial u} = 0$$

$$h_{45} = \frac{\partial \beta}{\partial v} = 0$$

$$h_{46} = \frac{\partial \beta}{\partial w} = 0$$

$$h_{47} = \frac{\partial \beta}{\partial b_x} = 0$$

$$h_{48} = \frac{\partial \beta}{\partial b_x} = 0$$

$$h_{49} = \frac{\partial \beta}{\partial b_z} = 0$$

APPENDIX D

THE DERIVATION AND APPLICATION OF THE SCHUR IDENTITY

The Schur identity (also called the "inside out rule") can be stated as follows:

The matrix equation

$$E = (A + BC)^{-1} \quad (D.1)$$

is equivalent to

$$E = A^{-1} - A^{-1} B [I + CA^{-1} B]^{-1} CA^{-1} \quad (D.2)$$

where A and E are nonsingular nxn matrices and where B and C are any matrices with dimension nxp and pxn respectively.

Derivation

Given

$$E = (A + BC)^{-1} \quad (D.3)$$

then

$$E^{-1} = A + BC \quad (D.4)$$

Post-multiplying by E gives

$$I = AE + BCE \quad (D.5)$$

and pre-multiplying by A^{-1} yields

$$\begin{aligned} A^{-1} &= E + A^{-1} BCE \\ E &= A^{-1} - A^{-1} BCE \end{aligned} \quad (D.6)$$

Now to eliminate E from the right hand side. First pre-multiply Eq. (D.7) by C

$$\begin{aligned}
 CE &= CA^{-1} - CA^{-1}B CE \\
 CE + CA^{-1}BCE &= CA^{-1} \\
 [I + CA^{-1}B]CE &= CA^{-1} \\
 CE &= [I + CA^{-1}B]^{-1} CA^{-1}
 \end{aligned} \tag{D.7}$$

Then substitute Eq. (D.7) into Eq. (D.6) to obtain the desired result:

$$E = A^{-1} - A^{-1}B[I + CA^{-1}B]^{-1} CA^{-1} . \tag{D.8}$$

Application

Consider the nxn covariance matrix

$$P_k = (\bar{P}_k^{-1} + H_k^T R_k^{-1} H_k)^{-1} \tag{D.9}$$

which is of the form

$$E = (A + BC)^{-1}$$

where $A = \bar{P}_k^{-1}$, $B = H_k^T$, and $C = R_k^{-1}H_k$. Applying the Schur identity (Eq. D.8) gives

$$P_k = \bar{P}_k - \bar{P}_k H_k^T [I + R_k^{-1} H_k \bar{P}_k H_k^T]^{-1} R_k^{-1} H_k \bar{P}_k . \tag{D.10}$$

Eq. (D.10) can be rewritten to obtain the desired result, i.e.,

$$P_k = \bar{P}_k - \bar{P}_k H_k^T (H_k \bar{P}_k H_k^T + R)^{-1} H_k \bar{P}_k . \tag{D.11}$$

APPENDIX E

THE DERIVATION AND APPLICATION OF THE ELLIPSOID OF PROBABILITY

In the analysis of navigation and guidance errors, it is sometimes convenient to display in geometric form the statistical data contained in a covariance matrix by generating surfaces of constant probability.

Consider a multivariate Gaussian distribution of the random n-vector z with zero mean and covariance

$$A = E[zz^T] . \tag{E.1}$$

The distribution is characterized by the quadratic form

$$a = z^T A^{-1} z = \frac{|A + zz^T|}{|A|} - 1 . \tag{E.2}$$

The scalar q can be shown to have a chi-square distribution with zero mean, unit variance and n-degrees of freedom⁽¹⁹⁾. Setting q = q₁ in Eq. (E.2) defines an "ellipsoid of probability." The probability that z falls within the ellipsoid corresponding to q₁ is the probability that q ≤ q₁ and is given by

$$P_r(q_1, n) = \frac{1}{2^{n/2} \Gamma(n/2)} \int_0^{q_1} q^{\frac{(n-2)}{2}} \exp(-q/2) dq \tag{E.3}$$

The lengths of the principal axes of the error ellipsoid are given by

$$a_i = q_1^{1/2} \lambda_i ; \quad i = 1, \dots, n \tag{E.4}$$

where λ_i is the i^{th} eigenvalue of the covariance matrix A . The orientations of the principal axes are given by the unit vectors

$$e_i = \frac{X_i}{|X_i|} ; \quad i = 1, \dots, n \quad (\text{E.5})$$

where X_i is the i^{th} eigenvector of the covariance matrix A .

The Bivariate Case

Consider the 2x2 covariance matrix

$$A = \begin{vmatrix} a_{11} & a_{12} \\ a_{21} & a_{22} \end{vmatrix} \quad (\text{E.6})$$

the eigenvalues of A are formed from

$$|A - \lambda I| = 0 . \quad (\text{E.7})$$

In expanded form, Eq. (E.7) becomes

$$\begin{vmatrix} a_{11} - \lambda & a_{12} \\ a_{21} & a_{22} - \lambda \end{vmatrix} = \lambda^2 - \lambda(a_{11} + a_{22}) + a_{11}a_{22} - a_{12}a_{21}$$

$$2\lambda = (a_{11} + a_{22}) \pm \sqrt{(a_{11} + a_{22})^2 - 4(a_{11}a_{22} - a_{12}a_{21})} .$$

Now let

$$a_{11} = \sigma_x^2$$

$$a_{22} = \sigma_y^2$$

$$a_{12} = a_{21} = \sigma_{xy} = \rho\sigma_x\sigma_y .$$

Then,

$$2\lambda = (\sigma_x^2 + \sigma_y^2) \pm [(\sigma_x^2 + \sigma_y^2)^2 - 4(\sigma_x^2 \sigma_y^2 - \rho^2 \sigma_x^2 \sigma_y^2)]^{\frac{1}{2}}$$

$$2\lambda = (\sigma_x^2 + \sigma_y^2) \pm [\sigma_x^4 + 2\sigma_x^2 \sigma_y^2 + \sigma_y^4 - 4\sigma_x^2 \sigma_y^2 + 4\rho^2 \sigma_x^2 \sigma_y^2]^{\frac{1}{2}}$$

$$2\lambda = (\sigma_x^2 + \sigma_y^2) \pm [(\sigma_x^2 - \sigma_y^2)^2 + 4\sigma_{xy}^2]^{\frac{1}{2}}$$

which yields the eigenvalues

$$\lambda_{1,2} = \frac{(\sigma_x^2 + \sigma_y^2)}{2} \pm [4(\sigma_x^2 - \sigma_y^2)^2 + \sigma_{xy}^2]^{\frac{1}{2}} \quad (\text{E.8})$$

The two eigenvectors $X_1 = \begin{bmatrix} x_1 \\ y_1 \end{bmatrix}$ and $X_2 = \begin{bmatrix} x_2 \\ y_2 \end{bmatrix}$ are defined by $AX_i = \lambda_i X_i$;
or

$$[A - \lambda_i I]X_i = 0 ; \quad i = 1,2 \quad (\text{E.9})$$

Hence from Eq. (E.9)

$$\begin{bmatrix} a_{11} - \lambda_i & a_{12} \\ a_{21} & a_{22} - \lambda_i \end{bmatrix} \begin{bmatrix} x_i \\ y_i \end{bmatrix} = 0$$

$$(a_{11} - \lambda_i)x_i + a_{12}y_i = 0$$

$$a_{21}x_i + (a_{22} - \lambda_i)y_i = 0$$

Setting $x_i = 1$ gives

$$(a_{11} - \lambda_i) + a_{12}y_i = 0$$

$$y_i = \frac{\lambda_i - a_{11}}{a_{12}} ; \quad i = 1,2 . \quad (\text{E.10})$$

The eigenvectors are then

$$X_i = \begin{bmatrix} 1 \\ \frac{\lambda_i - \sigma_x^2}{\sigma_{xy}} \end{bmatrix}; \quad i = 1, 2. \quad (\text{E.11})$$

The orientation of the error ellipse is specified by the angle ϕ between the major axis of the ellipse and the x-axis. The angle is given by

$$\begin{aligned} \cos \phi &= e_1 \cdot \bar{i} \\ \sin \phi &= e_2 \cdot \bar{j} \end{aligned} \quad (\text{E.12})$$

where

$$e_1 = \frac{X_1}{|X_1|} \quad \text{and} \quad e_2 = \frac{X_2}{|X_2|}.$$

This can be reduced to

$$\phi = \tan^{-1} \left(\frac{\lambda_1 - \sigma_x^2}{\sigma_{xy}} \right). \quad (\text{E.13})$$

The semimajor and semiminor axes of the error ellipse are given by

$$\begin{aligned} a &= |\lambda_1 q_1|^{1/2} \\ b &= |\lambda_2 q_1|^{1/2}. \end{aligned}$$

For the bivariate case Eq. (E.3) reduces to $P_r(q_1, 2) = 1 - \exp(-q_1/2)$. The probabilities corresponding to $\sqrt{q_1} = 1, 2, \text{ and } 3$ are 0.40, 0.86, and 0.99 respectively. Values of q_1 corresponding to other given values of P_r can be computed from $q_1 = 2 \ln(P_r - 1)$.

Target Dispersion Ellipse

Consider the error covariance matrix associated with the target

coordinates B·R and B·T

$$A = \begin{bmatrix} \sigma_{B \cdot R}^2 & \sigma_{B \cdot R, B \cdot T} \\ \sigma_{B \cdot R, B \cdot T} & \sigma_{B \cdot T}^2 \end{bmatrix}$$

Figure 39 shows the standard probability ellipse ($q_1 = 1$, $P_r = 0.40$) which represents A. The ellipse is defined by

$$a = \left\{ \frac{\sigma_{B \cdot R}^2 + \sigma_{B \cdot T}^2}{2} + \left[\frac{1}{4}(\sigma_{B \cdot R}^2 + \sigma_{B \cdot T}^2)^2 + \sigma_{B \cdot R, B \cdot T}^2 \right]^{1/2} \right\}^{1/2}$$

$$b = \left\{ \frac{\sigma_{B \cdot R}^2 + \sigma_{B \cdot T}^2}{2} - \left[\frac{1}{4}(\sigma_{B \cdot R}^2 + \sigma_{B \cdot T}^2)^2 + \sigma_{B \cdot R, B \cdot T}^2 \right]^{1/2} \right\}^{1/2}$$

$$\phi = \tan^{-1} \left(\frac{a^2 - \sigma_{B \cdot R}^2}{\sigma_{B \cdot R, B \cdot T}} \right) \quad -90 \leq \phi \leq 90$$

$$\psi = 90 + \phi \quad 0 \leq \psi \leq 180$$

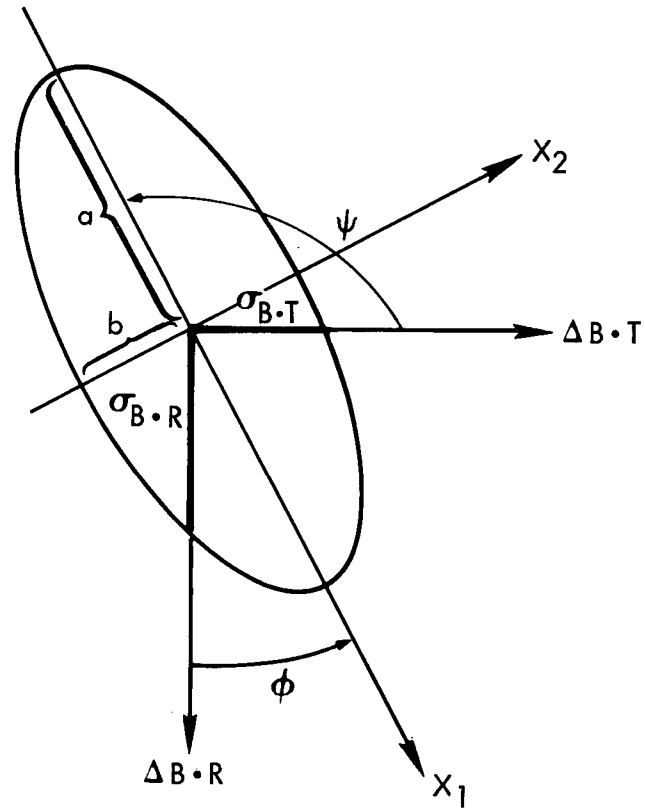


Figure 39 Standard Probability Ellipse

APPENDIX F

DEFINITION OF THE TARGETING COORDINATE SYSTEM

The targeting vector used in this study is defined by

$$T = \begin{bmatrix} B \cdot R \\ B \cdot T \\ t_e \end{bmatrix} \quad (F.1)$$

where t_e is the time of encounter (periapsis) and where $B \cdot R$ and $B \cdot T$ are the components of the vector \bar{B} in the target (R - T) plane. The vector \bar{B} , defined as the normal vector directed from the center of the target planet to the approach asymptote of the encounter hyperbola, is illustrated in Fig. 40.

R - S - T Coordinate System

Let \bar{S} be the unit vector in the direction of the approach asymptote. The unit vector \bar{T} is orthogonal to \bar{S} and parallel to the reference plane (e.g., ecliptic plane), i.e.,

$$\bar{T} = (\bar{S} \times \bar{P}_{ref}) / |\bar{S} \times \bar{P}_{ref}| \quad (F.2)$$

where \bar{P}_{ref} is the pole of the reference plane. The unit vector \bar{R} completes a right-handed orthogonal system, i.e.,

$$\bar{R} = \bar{S} \times \bar{T} \quad (F.3)$$

The B-vector targeting system involves the intersection of three planes, i.e., the orbit plane, the reference plane, and the target plane. The following

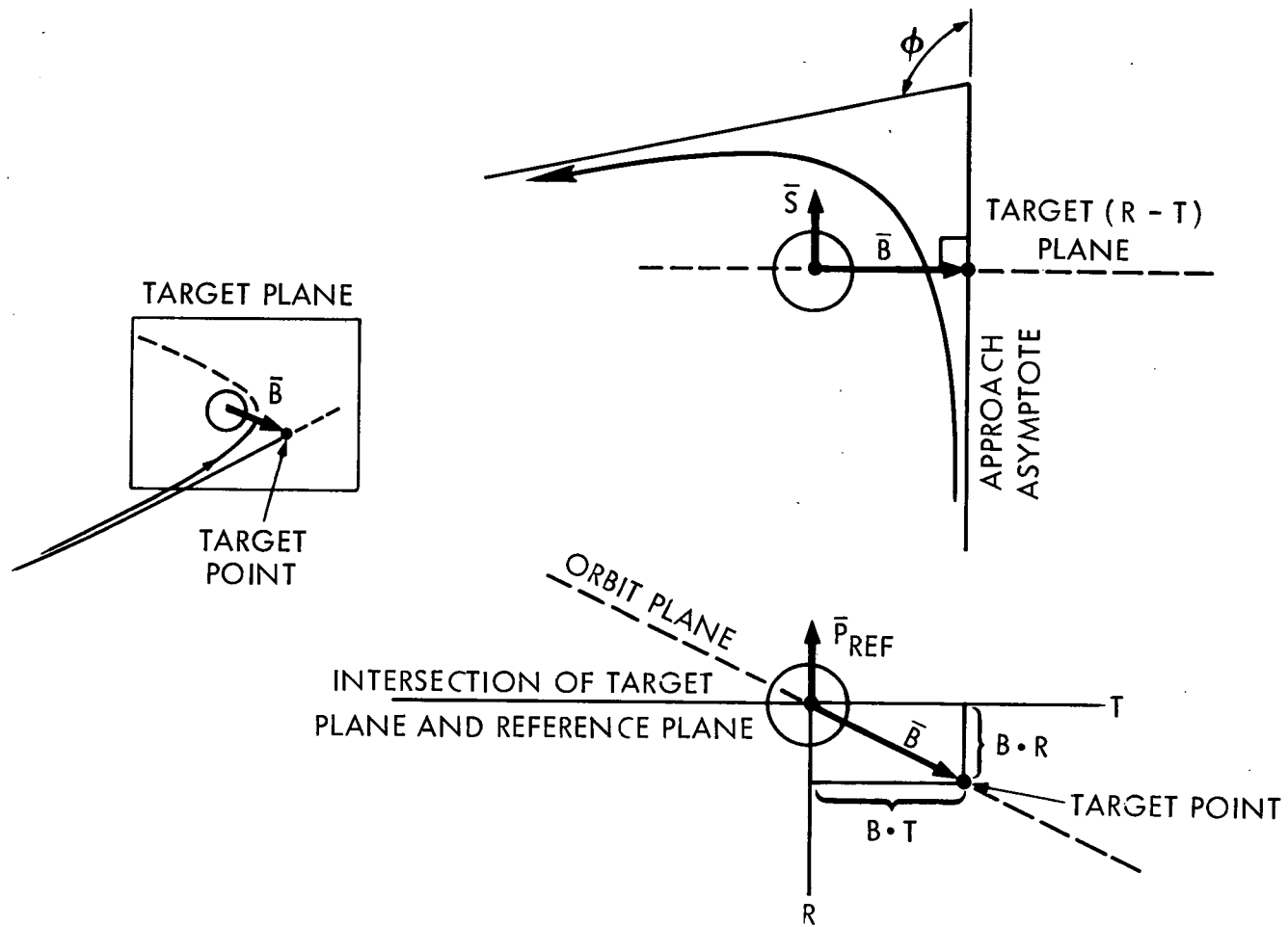


Figure 40 Targeting Geometry

notes may be helpful in visualizing the system:

- (1) \bar{T} lies along the intersection of the reference plane and the target plane.
- (2) \bar{B} lies along the intersection of the orbit plane and the target plane.
- (3) The orbit plane and the target plane are orthogonal.

Computational Algorithm

Given the state of a spacecraft in hyperbolic orbit relative to the planet (i.e., \bar{r} and \bar{v}) and the gravitational parameter μ , the vector \bar{B} is determined as follows:

- 1) $\bar{r} = (\bar{r} \cdot \bar{r})^{\frac{1}{2}}$ distance
- 2) $v = (\bar{v} \cdot \bar{v})^{\frac{1}{2}}$ speed
- 3) $C_3 = v^2 - 2\mu/r$ energy constant (twice the energy per unit mass)
- 4) $V_\infty = \sqrt{C_3}$ hyperbolic excess speed
- 5) $\bar{W} = (\bar{r} \times \bar{v}) / |\bar{r} \times \bar{v}|$ unit vector normal to orbit plane
- 6) $h = \bar{v} \cdot (\bar{W} \times \bar{r})$ magnitude of angular momentum
- 7) $a = \mu/C_3$ semimajor axis
- 8) $b = h/V_\infty$ semiminor axis
- 9) $\bar{P} = (v^2/\mu - 1/r)(1/e)\bar{r} - (\bar{r} \cdot \bar{v}/\mu)(1/e)\bar{v}$ unit vector in the direction of periapsis
- 10) $\bar{Q} = \bar{W} \times \bar{P}$ unit vector normal to \bar{W} and \bar{P}
- 11) $\bar{B} = a(e-1/e)\bar{P} - a\sqrt{1-1/e^2} \bar{Q}$ target vector
- 12) $H = \cos^{-1}[ae/(a+r)]$ hyperbolic auxiliary angle
- 13) $t_{go} = (H^3/\mu)^{\frac{1}{2}}\{e \tan H - \text{Log}[\tan(\pi/4 + H/2)]\}$ time to encounter (periapsis)
- 14) $t_e = t + t_{go}$ time of encounter

Additional parameters of the hyperbolic orbit may be computed as follows:

- | | | |
|-----|---|-------------------------------|
| 15) | $\bar{r}_p = a(e-1)\bar{P}$ | periapsis radius vector |
| 16) | $\psi = \pi - 2 \tan^{-1}(b/a)$ | turn angle |
| 17) | $f = -2 \tan^{-1}[\sqrt{(e+1)/(e-1)} \tan(H/2)]$ | true anomaly |
| 18) | $\bar{S} = (\bar{W} \times \bar{B})/ \bar{W} \times \bar{B} $ | approach asymptote |
| 19) | $\bar{S}_d = \cos \psi \bar{S} - \sin \psi (\bar{B}/ \bar{B})$ | departure asymptote direction |
| 20) | $i = \cos^{-1}(W_z)$ | inclination |
| 21) | $\Omega = \tan^{-1}(W_x/-W_y)$ | ascending node |

APPENDIX G

DERIVATION OF THE TARGET MAPPING MATRIX C

Consider the departure target vector $\bar{V}_{\infty D}$ expressed as a function of the approach target vector T by a Taylor expansion about the nominal path, i.e.,

$$\bar{V}_{\infty D} = \bar{V}_{\infty D}^* + \left[\frac{\partial \bar{V}_{\infty D}}{\partial T} \right]^* \delta T + \dots \quad (G.1)$$

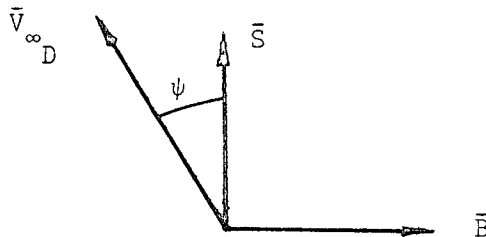
Neglecting terms higher than first order yields

$$\delta \bar{V}_{\infty D} = C \delta T \quad (G.2)$$

where $C = \left[\frac{\partial \bar{V}_{\infty D}}{\partial T} \right]^*$.

In what follows an analytical expression for the linear mapping matrix C will be derived for a two-body dynamical model.

Consider the geometric relationship between the departure target vector $\bar{V}_{\infty D}$, the approach asymptote \bar{S} , and the miss vector \bar{B} shown in the sketch below.



The departure target vector can be written as

$$\bar{V}_{\infty D} = V_{\infty D} \left[\cos \psi \bar{S} - \sin \psi \frac{\bar{B}}{b} \right] \quad (G.3)$$

where ψ is the turn angle, $b = |\bar{B}|$, and $V_{\infty} = |\bar{V}_{\infty D}|$. Resolving \bar{B} into the targeting components $B \cdot R$ and $B \cdot T$ yields

$$\bar{V}_{\infty D} = V_{\infty} [\cos \psi \bar{S} - \sin \psi \{(B \cdot R)\bar{R} + (B \cdot T)\bar{T}\}] .$$

Taking $\frac{\partial \bar{V}_{\infty D}}{\partial T}$ gives

$$\begin{aligned} \frac{\partial \bar{V}_{\infty D}}{\partial B \cdot R} &= \frac{V_{\infty}}{b} \left[b \left(\frac{\partial \cos \psi}{\partial B \cdot R} \right) \bar{S} - \left\{ \sin \psi + \frac{\partial \sin \psi}{\partial B \cdot R} (B \cdot R) \right. \right. \\ &- \frac{\sin \psi}{b} \left(\frac{\partial b}{\partial B \cdot R} \right) B \cdot R \} \bar{R} - \left. \left\{ \frac{\partial \sin \psi}{\partial B \cdot R} (B \cdot T) \right. \right. \\ &- \left. \left. \frac{\sin \psi}{b} \left(\frac{\partial b}{\partial B \cdot R} \right) B \cdot T \right\} \bar{T} \right] \quad (G.4) \end{aligned}$$

$$\begin{aligned} \frac{\partial \bar{V}_{\infty D}}{\partial B \cdot T} &= \left(\frac{V_{\infty}}{b} \right) \left[b \frac{\partial \cos \psi}{\partial B \cdot T} \bar{S} - \left\{ \sin \psi + \frac{\partial \sin \psi}{\partial B \cdot R} (B \cdot R) \right. \right. \\ &- \left. \frac{\sin \psi}{b} \left(\frac{\partial b}{\partial B \cdot R} \right) \right\} \bar{R} - \left\{ \frac{\partial \sin \psi}{\partial B \cdot R} (B \cdot T) \right. \\ &- \left. \left. \frac{\sin \psi}{b} \left(\frac{\partial b}{\partial B \cdot R} \right) B \cdot T \right\} \bar{T} \right] \quad (G.5) \end{aligned}$$

$$\frac{\partial \bar{V}_{\infty D}}{\partial t_e} = 0 \quad (G.6)$$

Since $b^2 = B \cdot R^2 + B \cdot T^2$, then

$$\frac{\partial b}{\partial B \cdot R} = \frac{B \cdot R}{b} \quad (G.7)$$

and

$$\frac{\partial b}{\partial B \cdot T} = \frac{B \cdot T}{b} \quad (G.8)$$

The turn angle is defined by

$$\cos \psi = \left(\frac{b^2 V_\infty^4}{\mu^2} - 1 \right) / \left(\frac{b^2 V_\infty^4}{\mu^2} + 1 \right) \quad (G.9)$$

thus,

$$\frac{\partial \cos \psi}{\partial b} = \frac{4bV_\infty^4}{\mu^2 \left(\frac{b^2 V_\infty^4}{\mu^2} + 1 \right)} \quad (G.10)$$

and

$$\frac{\partial \sin \psi}{\partial b} = \left(\frac{\partial \cos \psi}{\partial b} \right) (-\cot \psi) \quad (G.11)$$

Define

$$d_1 = \frac{4bV_\infty^4}{\mu^2 \left(\frac{b^2 V_\infty^4}{\mu^2} + 1 \right)} \quad (G.12)$$

and

$$d_2 = -d_1 \cot \psi \quad (G.13)$$

Then

$$\frac{\partial \cos \psi}{\partial B \cdot R} = \frac{\partial \cos \psi}{\partial b} \cdot \frac{db}{dB \cdot R} = d_1 \left(\frac{B \cdot R}{b} \right) \quad (G.14)$$

$$\frac{\partial \cos \psi}{\partial B \cdot T} = \frac{\partial \cos \psi}{\partial b} \cdot \frac{db}{dB \cdot T} = d_1 \left(\frac{B \cdot T}{b} \right) \quad (G.15)$$

Likewise

$$\frac{\partial \sin \psi}{\partial B \cdot R} = d_2 \left(\frac{B \cdot R}{b} \right) \quad (G.16)$$

$$\frac{\partial \sin \psi}{\partial B \cdot T} = d_2 \left(\frac{B \cdot T}{b} \right) . \quad (G.17)$$

Now Eqs. (G.4) and (G.5) can be rewritten

$$\frac{\partial \bar{V}_{\infty D}}{\partial B \cdot R} = (a_{11} \bar{R} + a_{21} \bar{S} + a_{31} \bar{T}) \left(\frac{V_{\infty}}{b} \right) \quad (G.18)$$

$$\frac{\partial \bar{V}_{\infty D}}{\partial B \cdot T} = (a_{12} \bar{R} + a_{22} \bar{S} + a_{32} \bar{T}) \left(\frac{V_{\infty}}{b} \right) \quad (G.19)$$

where

$$a_{11} = \sin \psi \left[\left(\frac{B \cdot R}{b} \right)^2 - 1 \right] - \frac{d_2}{b} (B \cdot R)^2 \quad (G.20)$$

$$a_{21} = d_1 (B \cdot R) \quad (G.21)$$

$$a_{31} = \frac{(B \cdot R)(B \cdot T)}{b^2} (\sin \psi - b d_2) \quad (G.22)$$

$$a_{12} = a_{31} \quad (G.23)$$

$$a_{22} = d_1 (B \cdot T) \quad (G.24)$$

$$a_{32} = \sin \psi \left[\left(\frac{B \cdot T}{b} \right)^2 - 1 \right] - \frac{d_2}{b} (B \cdot T)^2 . \quad (G.25)$$

Forming

$$A = \begin{bmatrix} a_{11} & a_{12} & 0 \\ a_{21} & a_{22} & 0 \\ a_{31} & a_{33} & 0 \end{bmatrix} \quad (G.26)$$

and defining

$$B = [\bar{R} \ \bar{S} \ \bar{T}] \quad (\text{G.27})$$

leads to

$$C = (BA) \left(\frac{V_\infty}{b} \right) . \quad (\text{G.28})$$

REFERENCES

1. Lee, V. A., Jones, D. W., Poteet, M. C., "Trajectory and Mission Analysis Aspects of Jupiter Flyby Probes," Proceedings of the XVII International Astronautical Congress, Belgrade, Yugoslavia, September, 1967.
2. Archer, J. L., "Mission Modes to the Outer Solar System," Presented at the AIAA 8th Aerospace Sciences Meeting, New York, New York, January, 1970.
3. Silver, B. W., "Grand Tours of the Jovian Planets," AIAA Preprint No. 67-613, Presented at the AIAA Guidance, Control and Flight Dynamics Conference, Huntsville, Alabama, August, 1967.
4. Friedlander, A. L., "Guidance Analysis of the Multiple Outer Planet (Grand Tour) Mission," Presented at the AAS/AIAA Astrodynamics Specialist Conference, Jackson, Wyoming, September, 1968.
5. Kingsland, L., "Trajectory Analysis of the Grand Tour Mission to the Outer Planets," AIAA Preprint No. 68-1055, Presented at the AIAA 5th Annual Meeting and Display, Philadelphia, Pennsylvania, October, 1968.
6. Manning, L. A., Fraser, D. C., "Guidance and Navigation Requirements for Missions to the Outer Planets," AIAA Preprint No. 70-71, Presented at the AIAA 8th Aerospace Sciences Meeting, New York, New York, January, 1970.
7. Curkendall, D. W. and Stephenson, R. R., "Earthbased Tracking and Orbit Determination - Backbone of the Planetary Navigation System," Astronautics and Aeronautics, Vol. 8, pp. 30-36, May, 1970.
8. Melbourne, W. G., "Planetary Ephemerides," Astronautics and Aeronautics, Vol. 8, pp. 38-43, May, 1970.
9. Bryson, A. E., Jr., Ho, Yu-Chi, Applied Optimal Control, Optimization, Estimation and Control, Blaisdell, 1969.
10. Deutsch, R., Estimation Theory, Prentice-Hall, 1965.
11. Handbook of Mathematical Functions, AMS 55, National Bureau of Standards, June, 1964.
12. Battin, R. H., "A Statistical Optimizing Navigation Procedure for Space Flight," ARS Journal, Vol. 32, pp. 1681-1696, November, 1962.
13. Rauch, H. E., Tung, F., and C. T. Striebel, "Maximum Likelihood Estimation of Linear Dynamic Systems," AIAA Journal, Vol. 3, No. 8, August, 1965.

14. Liebelt, P. B., An Introduction to Optimal Estimation, p. 141, Addison-Wesley, 1967.
15. Jones, D. W., Hagar, H., Tapley, B. D., "STEP VI, a Navigation and Guidance Analysis Program with Interactive Graphics," The University of Texas at Austin, to be published.
16. Ball, J. E. and Duxbury, T. C., "Navigating the Grand Tours," Astronautics and Aeronautics, Vol. 8, pp. 73-76, September, 1970.
17. Shannon, C. E. and Weaver, W., The Mathematical Theory of Communication, The University of Illinois Press, 1949.
18. Potter, J. E. and Fraser, D. C., "A Formula for Updating the Determinant of the Covariance Matrix," AIAA Journal, Vol. 5, pp. 1352-1354, July, 1967.
19. Rao, C. R., Linear Statistical Inference and its Applications, John Wiley, 1965.

BIBLIOGRAPHY

1. Battin, R. H., Astronautical Guidance, McGraw Hill, New York, New York, 1964.
2. Born, G. H., "The Derivation of a General Solution and its Application to Orbit Determination," Ph.D. Dissertation, The University of Texas at Austin, 1968.
3. Breakwell, J. V., H. E. Rauch, and F. F. Tung, "Theory of Minimum Effort Control," NASA CR-378, Langley Research Center, 1966.
4. Bucy, R. S. and P. D. Joseph, Filtering for Stochastic Processes with Applications to Guidance, Interscience Publishers, New York, 1968.
5. Curkendall, D. W. and C. G. Pfeiffer, "Discussion of Guidance Policies for Multiple-Impulse Correction of the Trajectory of a Spacecraft," Preprint No. 63-334, Presented at the AIAA Guidance and Control Conference, Cambridge, Massachusetts, August 1963.
6. Duxbury, T. C. and W. G. Breckenridge, "Mariner Mars 1969 Optical Approach Navigation," AIAA Preprint No. 70-70, Presented at the AIAA 5th Aerospace Sciences Meeting, New York, January 1970.
7. Escobal, P. R., Methods of Orbit Determination, John Wiley, New York, 1965.
8. Ingram, D. S., "Orbit Determination in the Presence of Unmodeled Accelerations," Applied Mechanics Research Laboratory Report No. AMRL-1022, The University of Texas at Austin, January 1971, also Ph.D. Thesis, The University of Texas at Austin, Austin, Texas, November 1970.
9. Jordon, J. F., "Optimal Stochastic Control Theory Applied to Interplanetary Guidance," Ph.D. Dissertation, The University of Texas at Austin, 1966.
10. Nishimura, T. and C. G. Pfeiffer, "A Dynamic Programming Approach to Optimal Stochastic Orbital Transfer Strategy," Journal of Spacecraft and Rockets, Vol. 7, No. 4, April 1970.
11. Parzen, E., Modern Probability Theory and its Applications, John Wiley, New York, 1960.
12. Solloway, C. B., "Elements of the Theory of Orbit Determination," EPD-255, Jet Propulsion Laboratory, December 1964.

13. Soong, T. T. and C. G. Pfieffer, "Unified Guidance Analysis in Design of Space Trajectories," Journal of Spacecraft and Rockets, Vol. 3, No. 1, January 1966.
14. Szebehely, V., Theory of Orbits, Academic Press, New York, 1967.
15. Tapley, B. D. and G. H. Born, "Sequential Estimation of the State and the Observation-Error Covariance Matrix," AIAA Journal, Vol. 9, No. 2, February 1971.
16. Van Gelder, A., J. Dunn and J. Mendelsohn, "Final Value Optimal Stochastic Control Problem with Bounded Controller," AIAA Journal, Vol. 5, No. 8, August 1967.